The Thesis committee for Mikko Juha Viljami Ponkala
certifies that this is the approved version of the following thesis:

Humidity Effects on Hygroscopic Particles Deposited on HEPA Filters and Silicon Wafer Surfaces

APPROVED BY

SUPERVISING COMMITTEE:

Ofodike A. Ezekoye, Supervisor

John S. Haglund

Humidity Effects on Hygroscopic Particles Deposited on HEPA Filters and Silicon Wafer Surfaces

by

Mikko Juha Viljami Ponkala, B.S.M.E

THESIS

Presented to the Faculty of the Graduate School of

The University of Texas at Austin

in Partial Fulfillment

of the Requirements

for the Degree of

MASTER OF SCIENCE IN ENGINEERING

The University of Texas at Austin

December 2012

To my father and mother, Juha and Outi.

Acknowledgments

I would like to thank Texas Instruments for funding my research. This work is a direct result of Texas Instruments' input and support. From Texas Instruments, I'd like to especially acknowledge John DeGenova and John Stuber for their expertise and guidance throughout my research. I would also like to thank John Haglund for serving as the second reader on my thesis and for all of his assistance with aerosol generation and characterization. Additionally, this work would not have been possible without my supervisor Professor Ofodike Ezekoye. I truly appreciate his deep knowledge of the fundamentals underlying the engineering sciences and getting the opportunity to learn from him. I thank him for his patience and intelligence in guiding me to complete all the research tasks.

Working in the Thermal-Fluids Systems area within the Department of Mechanical Engineering at the University of Texas at Austin has been a very enjoyable experience. Within the department, I'd like to thank all the members of my research group for collaboration on various problems. Specifically, I'd like to thank Kristopher Overholt for his assistance in computational methods and Morgan Bruns and Benjamin Barr for their help on analytical problems. Outside of my research, my graduate school experience would not have been as enjoyable without the support of my friends, especially Cassandra Telenko, Katie Carpenter, and Matt Kincaid.

Finally, I'd like to thank my family for their support throughout my education. I'm truly in debt for my parents Juha and Outi for all the opportunities they have presented me with. Also, my brother Joonas has been a great inspiration in pursuing my degrees in mechanical engineering.

Humidity Effects on Hygroscopic Particles Deposited on HEPA Filters and Silicon Wafer Surfaces

Mikko Juha Viljami Ponkala, M.S.E.
The University of Texas at Austin, 2012

Supervisor: Ofodike A. Ezekoye

Semiconductor wafer manufacturing facilities (fab) must maintain extremely clean air environments to minimize the number of wafers scrapped due to contamination which would result in reduced yields. The fab air is cleaned bypassing it through either HEPA or ULPA filters. A number of airborne fab contaminants may be hygroscopic causing them to exist as a solid or a liquid when in equilibrium with their environment's relative humidity. The effect of relative humidity on such contaminants is poorly documented whether they were to be captured in a filter or deposited on a wafer. The work presented here experimentally characterizes NaCl evolution within HEPA filters when exposed to humidity fluctuations and the effect of humidity on NH_4Cl corrosiveness when deposited on cobalt coated wafers with a TiN layer. Successive deliquescence and efflorescence fluctuations were imposed on particles captured on a glass fiber HEPA filter. Scanning Electron Microscopy (SEM) and Environmental SEM (ESEM) studies of the filters showed that the NaCl, under humidity excursions, did not penetrate deep into the filter but deliquesced and effloresced near the top surface of the filter. Pressure drop measurements for filters containing NaCl particles showed differences in ΔP associated with relative humidity changes. These ΔP changes suggested some redistribution particle properties. When

exposed to a relative humidity of 20%, the NH_4Cl particles did not corrode the cobalt wafer beyond the location of the initial deposit. At 61% relative humidity, the surrounding areas of the particles were corroded with a solid artifact left at the original location. At 76% relative humidity the NH_4Cl particles were observed to have deliquesced, which is below the expected deliquescence relative humidity. The corrosion of the cobalt wafer was most extensive when the NH_4Cl particles had deliquesced.

Table of Contents

List of Tables

List of Figures

Chapter 1

Introduction: Filtration and Hygroscopic Particle Background

1.1 Introduction

Maintaining a high air quality environment is important in a number of industries. Specifically for the semiconductor manufacturing industry, clean air is required to avoid contaminating the silicon wafers along any part of the manufacturing process which is intended to produce functioning semiconductor devices. Since feature size on wafers continue to decrease to meet the forecasted industry goals, the air quality of the semiconductor manufacturing facility (fab) becomes even more critical as particles in the nanometer range can cause nonfunctioning devices. In a fab, the air cleaned by passing it through either High Efficiency Particulate Air (HEPA) filters or Ultra Low Penetration Air (ULPA) filters. HEPA filters remove 0.3μm particle size with at least 99.95% efficiency while ULPA filters remove with at least 99.9995% efficiency. In addition to the recirculation air filters used in the main environment (i.e. ballroom), tools may be isolated in mini environments that have their own set of filters to maintain an even stricter air quality level.

Due to the myriad of chemicals used in a fab, the potential particulate contaminants encountered may have a wide variety of compositions. Some of the particle contaminants are hygroscopic in nature, meaning that they may exist as a solid or a liquid depending on the relative humidity of the environment. Knowing the chemical and physical states of such particles is extremely important from a capturing perspec-

tive as the filtration of liquid and solid aerosols differs significantly. Additionally, if a hygroscopic particle were to deposit onto a wafer, the particle's interaction with the substrate would be influenced by its physcal state. Even though the temperature and relative humidity of a fab are tightly monitored and controlled, localized humidity swings may occur due to small accidents such as a water spill within the ballroom. Additionally, the outdoor air filters may experience swings in humidity for a short period depending on the ability of the air handler unit control to adjust to fluctuating outdoor relative humidity level. Therefore it is important to understand the effect of humidity on hygroscopic particles as well as the time scales associated with any interaction between a particle and environmental water vapor.

The work presented here experimentally addresses the effects of relative humidity on hygroscopic particles that have been captured on HEPA filters in a dry state but are subsequently exposed to high humidity fluctuations. One goal of the filter experiments is to quantify whether the deposited hygroscopic particles are transported within the filter, ultimately resulting in re-entrainment down stream of the filter. Atomized NaCl crystals are used as a surrogate in the filter experiments since they are among the most researched hygroscopic salts in the literature, providing ample background knowledge on their interactions with water vapor. In addition to the filter tests, NH_4Cl particles are deposited on pieces scored from a 300mm wafer and exposed to varying levels of relative humidities to assess the effect of water vapor on wafer corrosion. NH_4Cl particles are chosen for the wafer experiments since they represent a contaminant that is more likely to be encountered in a fab than NaCl.

This thesis is organized in three main sections. Chapter 1, presents background on dry particleand liquid aerosol filtration. It also provides theoretical background on the time scales and thermodynamics analysis associated with hygroscopic particle

phase transformations. Chapter 1 is concluded by discussing the published work on filtration of hygroscopic particles.

Chapter 2, presents the author's contributed experimental work on hygroscopic filtration. The section begins by presenting the experimental apparatus along with design and calibration considerations. Following the description of the test apparatus, results are presented on the HEPA filters loaded with NaCl particles subjected to humidity fluctuations. The experimental results include filter pressure drop and mass change, as well as scanning electron microscopy visualizations of the changes taking place on the filter. Before concluding the chapter, experimental results of NH_4Cl particles deposited on a HEPA filter are presented to clarify whether a measurable water vapor absorption occurs at relative humidities below the deliquescence point.

Chapter 3, the final main section, presents the results of the wafer contamination studies. The chapter presents visualizations of NH_4Cl contaminated cobalt witness wafer samples subjected to a wide range of relative humidities to help clarify the levels of relative humidity a wafer can be exposed tobefore showing visible changes. To support the optical observations of long time humidity exposures, scanning electron microscopy is utilized to provide further insight into the surface changes on wafers when the hygroscopic contaminants change phase. The scanning electron microscopy results include particles in the hundreds of micrometer size range for large scale analysis as well as atomized particles in the micrometer range to provide indication of wafer particle interaction in size ranges closer to the actual conditions encountered in a fab.

1.2 Filtration of Solid Aerosols

An aerosol can be deposited through five mechanisms: interception, inertial impaction, diffusion, gravitational settling, and electrostatic attraction. Interception occurs when an aerosol comes to within one radius of the surface of a filter fiber, thus coming into contact and adhering. Inertial impaction takes place when an aerosol is unable to follow the gas stream line due to its inertia, resulting in a collision with a fiber. Under diffusion, the aerosol does not follow the gas stream line due to Brownian motion and adheres to a fiber. Finally, gravitational settling occurs due to gravitational force depositing an aerosol and electrostatic deposition may occur due to charging of the aerosol or the fibers. The three first mechanisms are shown in Figure 1.1 [1]. Figure 1.2 illustrates the deposition of dry aerols onto fibers. Initially, the particles are captured by the fibers, but after a while the particles start forming dendrites on top of the filter resulting in the formation of a cake layer.

In general, filtration of solid particles can be divided into three stages. In the first stage, the pressure drop across the filter increases slowly with added mass while the aerosol is captured by the filter. In the second region, the pressure drop begins to increase nonlinearly. Finally the third stage, cake filtration, is reached where aerosols are captured by already deposited aerosols on top of the filter [2]. The evolution of a pressure drop across a filter is illustrated in Figure 1.3.

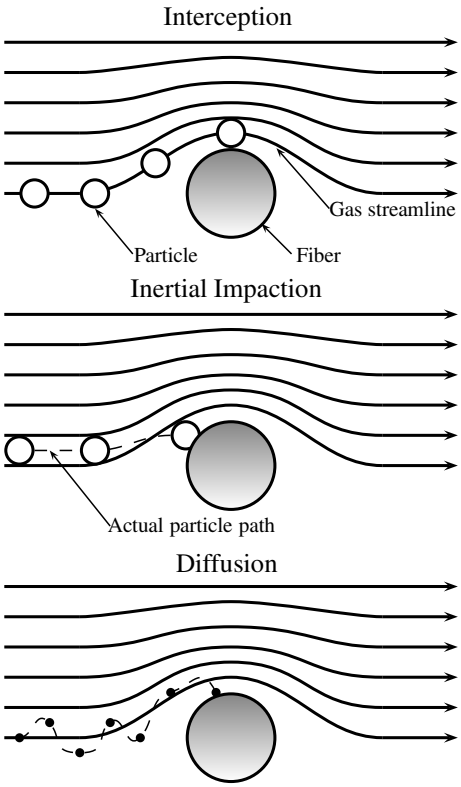

Figure 1.1: Interception, impaction, and diffusion of a particle on a fiber, adpated from [1].

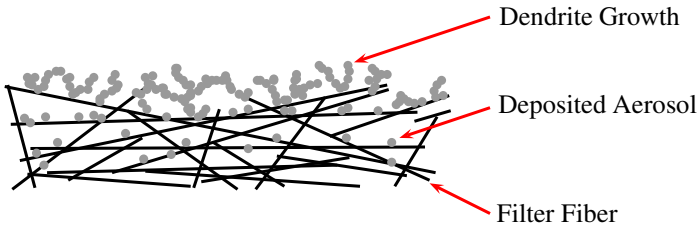

Figure 1.2: Deposition of solid aerosols onto a fibrous high efficiency filter

Thomas et al. showed that evolution of the pressure drop is dependent on multiple variables. The dependence of face velocity and particle diameter on mass loading are shown in Figures 1.4 and 1.5 respectively. In both figures, a nonlinear

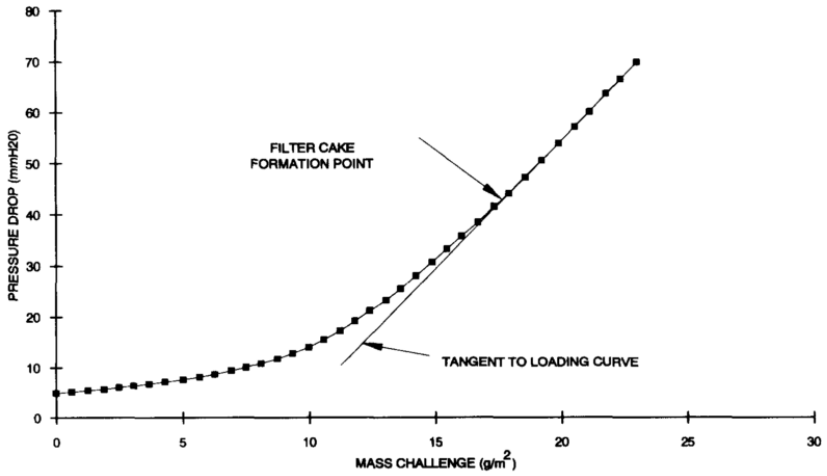

Figure 1.3: Pressure drop as a function of collected mass illustrating onset of cake filtration, taken from [2]

region exists at very low mass loadings as the onset of cake filtration has not been encountered. The experimental results are for HEPA filters loaded with soda fluorescein [3].

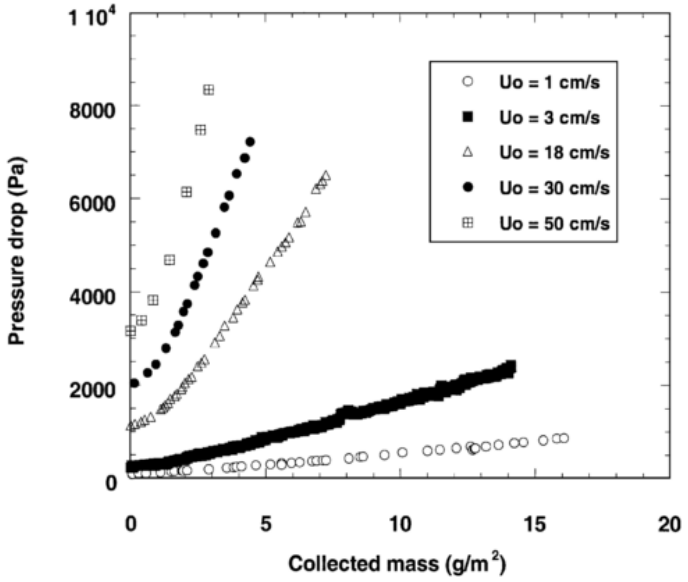

Figure 1.4: Evolution of pressure drop with dry particle loading for a variety of filtration velocities, taken from [3]

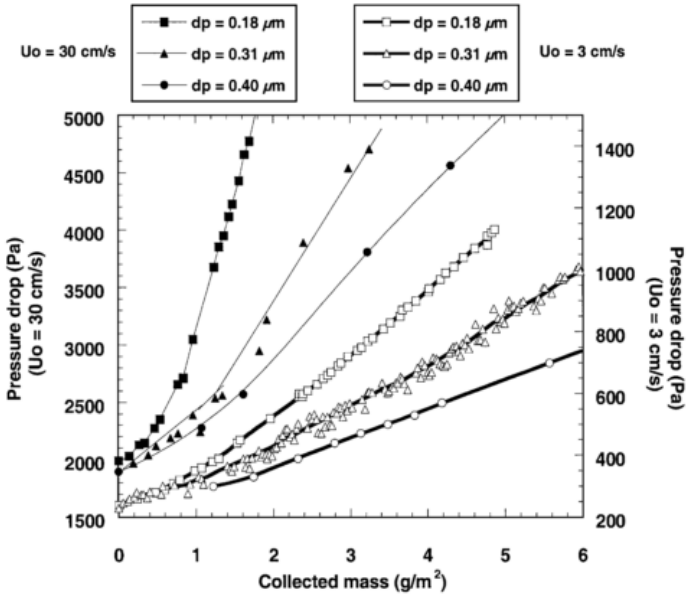

Figure 1.5: Evolution of pressure drop depending on dry particle size for two different filtration velocities, taken from [3]

For HEPA filters the first stage may not exist, as cake formation is instantaneous [2]. Novick et al. studied characteristics of HEPA filters by loading them with dry sodium chloride, ammonium chloride, and aluminum oxide particles. The overall pressure drop across a HEPA filter can be expressed as

$$\Delta P = \Delta P_f + \Delta P_c \tag{1.1}$$

In the above equation, ΔP_f represents the pressure drop across a clean filter while ΔP_c is the pressure drop due to particle loading. Since porous, D'Arcy's law upholds and ΔP_f can be expressed as

$$\Delta P_f = K_f v \tag{1.2}$$

K_f is a constant that depends on the physical properties of the filter while v is the velocity through the filter. Assuming monodisperse particle loading, the pressure drop in the cake expressed in terms of mass is

$$\Delta P_c = K_c \frac{mv}{A_f} \tag{1.3}$$

where K_c is the cake specific resistance, m the mass loading, and A_f the filtration surface area. Figure 1.6 shows how cake filtration loading for a variety of size distributions based on mass median diameter (MMD) affects pressure drop across a HEPA filter. The HEPA filters were loaded under 2.45 to 3.0 cm/s gas velocities [4].

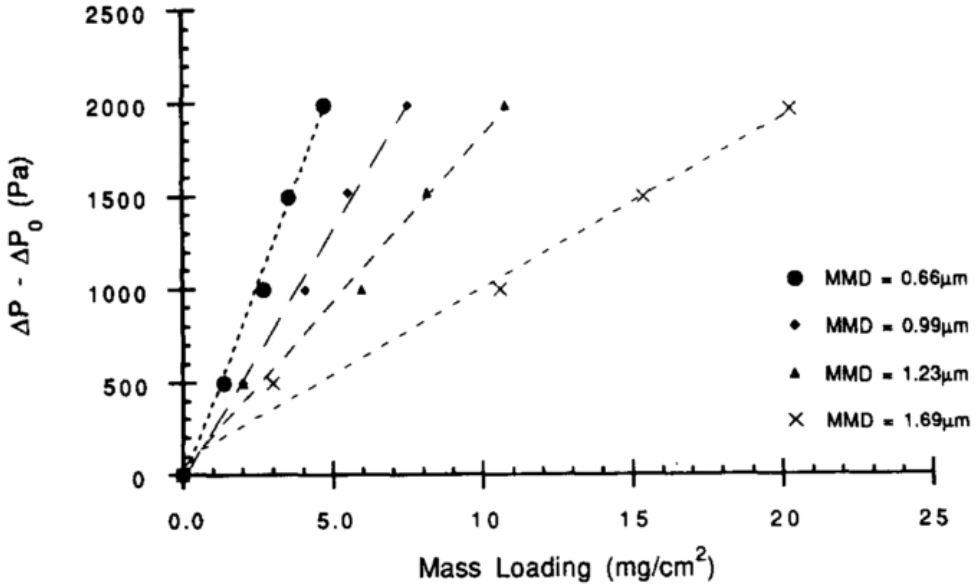

Figure 1.6: Net increase in pressure drop based on mass loading and particle size distribution for sodium chloride aerosols, taken from [4]

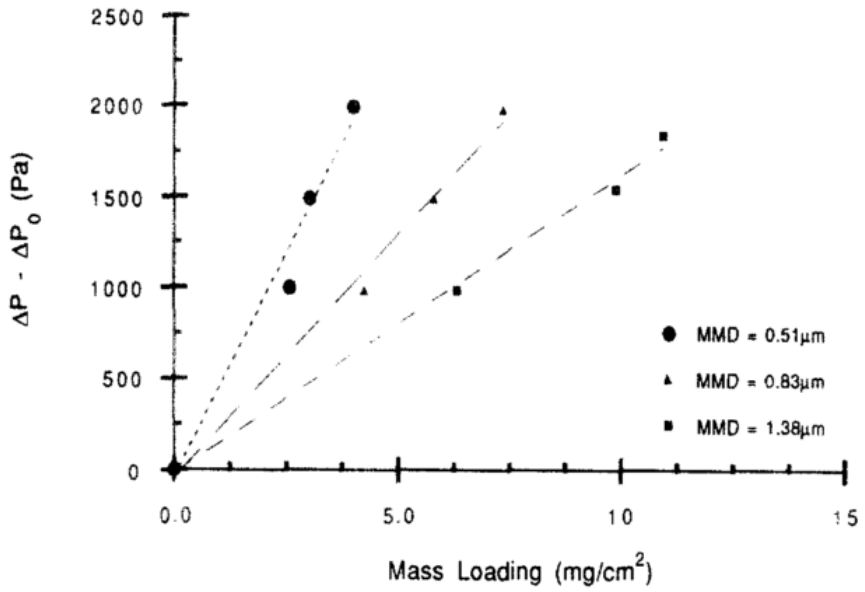

Figure 1.7: Net increase in pressure drop based on mass loading and particle size distribution for ammonium chloride aerosols, taken from [4]

1.3 Filtration of Liquid Aerosols

As with filtration of dry particles, substantial research has also been performed on the filtration of wet particles. The research indicates that filtration of wet particles is very distinct from dry particles. Instead of forming dendrite structures as in the case with dry aerosols, wet aerosols form droplets that after substantial loading can cause webbing in and clogging of the filter. The distribution of liquid aerosol in the filter depends on the packing density of the filter, α. At low packing densities ($\alpha < 0.004$) the liquid forms large droplets at the intersections of fibers. In high packing density filters ($\alpha > 0.1$) the collected liquid aersol forms pools and bridges between the fibers. The two collection distributions are illustrated in Figure 1.8 [5, 13].

Contal et al. experimented with submicron liquid aerosol collection on HEPA filters. The authors divided the evolution within the filter in to four stages. In

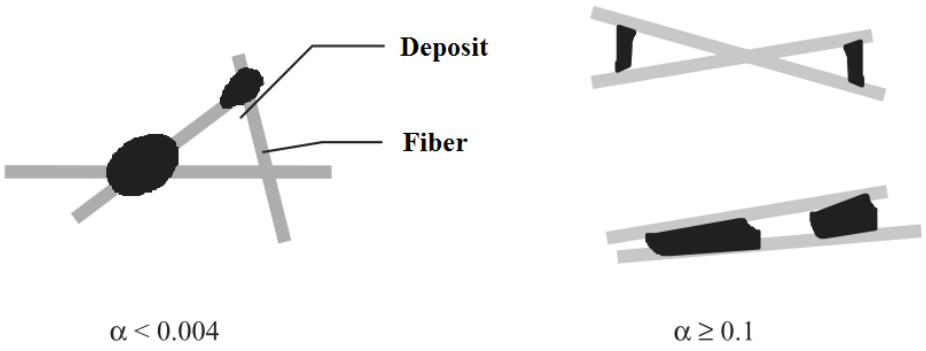

Figure 1.8: Illustration of liquid aerosol collection depending on filter packing density, taken from [5]

the first stage, droplets deposit onto the fibers and the pressure drop increases due to reduction in available flow area. In the second stage droplets join together to cover the filters and the collected liquid redistributes within the filter due to capillary action. In the third stage a liquid film is formed on top of the filter and the pressure drop increases exponentially. In the fourth stage liquid films and bridges are formed throughout the thickness of the filter eventually resulting in drainage of the liquid and the pressure drop stabilizes. During the fourth stage re-entrainment was found to be insignificant compared to drainage. Re-entrainment is defined as droplets being aerosolized from the filter while drainage is pooling of liquid immediately following the filter for horizontal configuration. The four stages along with visualizations of the collected liquid are shown in a pressure drop diagram in Figure 1.9. Figure 1.10 shows the dependence of pressure drop on air velocity for a filter loaded with liquid aerosol while Figure 1.11 shows the corresponding penetration profiles [5].

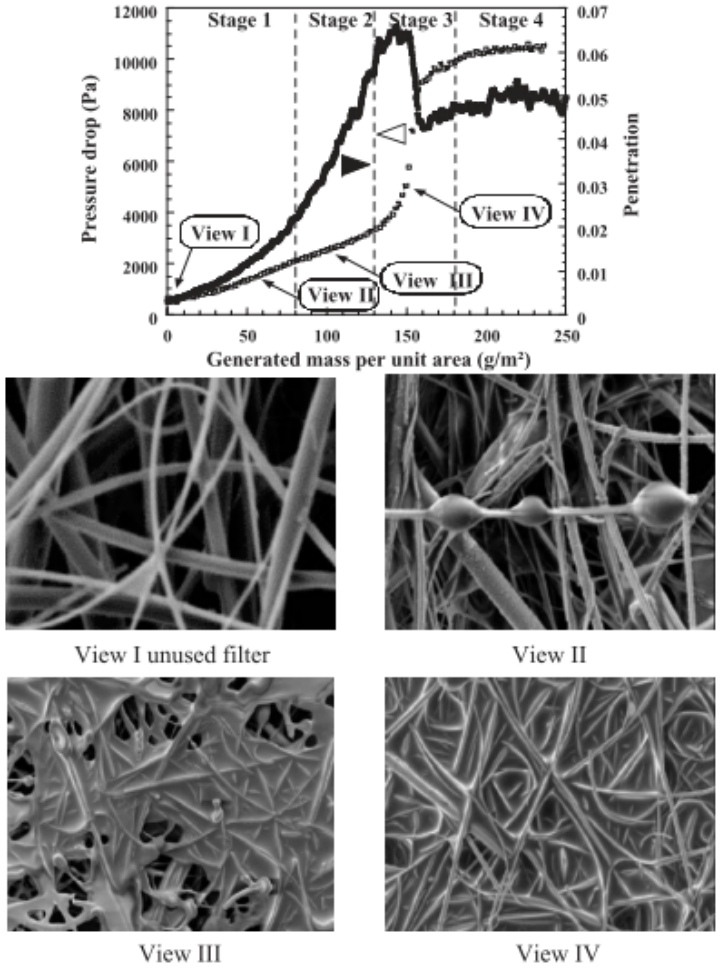

Figure 1.9: Four stages of liquid aerosol filtration with corresponding SEM images, taken from [5]

To quantify the aerosol penetration and re-entrainment, Contal et al. set up another filter downstream of the test filter as illustrated in Figure 1.12. Under loading, once the test filter was saturated the pressure drop in the downstream filter was noted to increase. However, the authors indicated that the increase in pressure drop in the downstream filter was due to penetration and not re-entrainment since upon flowing clean air through the test filter the pressure drop in the downstream filter was not observed to increase.

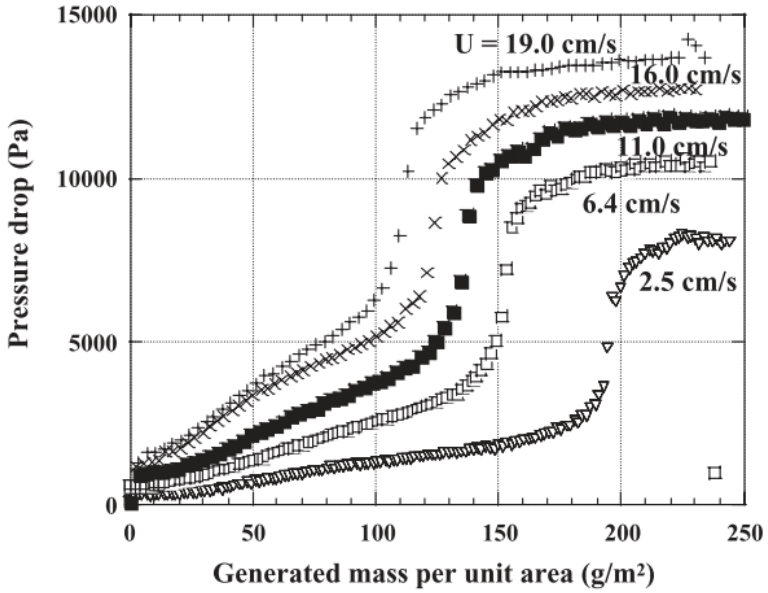

Figure 1.10: Pressure drop as a function of loaded mass for liquid aerosol filtration at various air velocities, taken from [5]

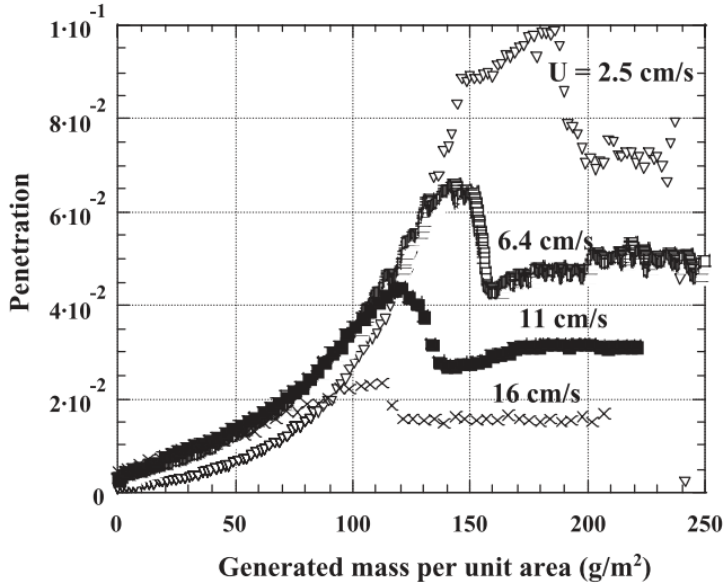

Figure 1.11: Penetration as a function of loaded mass for liquid aerosol filtration at various air velocities, taken from [5]

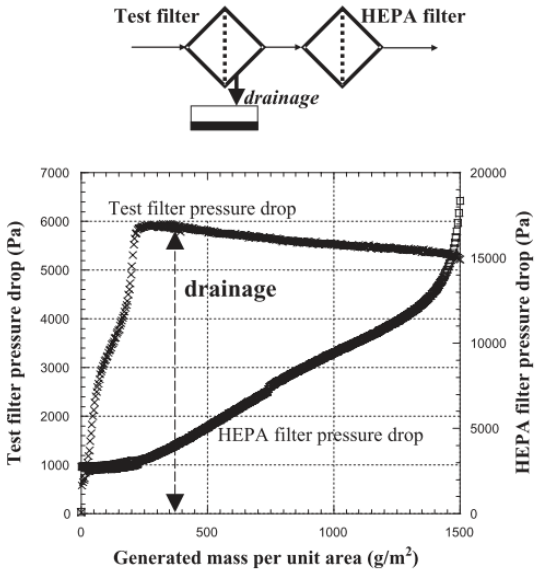

Figure 1.12: Pressure drop of test filter and a downstream filter to capture lost mass from test filter, taken from [5]

Tekasakul et al. studied collected liquid mass retention of filter media saturated with palm oil and propylene glycol. The saturation was reached by soaking the filter with oil. More mass was retained in filters saturated with palm oil than with propylene glycol after flowing through air until a constant mass was reached, which could be explained by higher viscosity of palm oil. Additionally, more mass was retained at velocity of 7 cm/s than 28cm/s. The higher retention at a lower velocity could be explained by lower drag on the fluid [14]. Penicot et al. studied differences in pressure drop across HEPA filters loaded with solid or liquid particles. Stopping loading upon clogging of the filter, indicated by reaching the plateau following the spike in pressure drop, with liquid particles, the pressure drop across the filter dropped to a lower constant level from the initial plateau when running through clean air. However, no mass loss was observed indicating that the collected liquid redistributed within the filter [15].

Payet et al. studied the penetration in HEPA filters loaded with liquid aerosols. After loading a filter with diethylsebacate (DES), the penetration by solid NaCl particles was found to increase after 1.25 times the initial pressure drop [16]. Frising et al. studied the effect of the filter on the drainage of liquid from the filter. At velocity close to 0.9 m/s only approximately 10% of the void space was occupied by the collected liquid while at velocity as low as 0.05 m/s 70% of the void space was filled. However, higher velocities had the benefit of lower penetration [17].

1.4 Deliquescence and Efflorescence of Hygroscopic Particles

The physical state of many inorganic salts depends on the relative humidity of their environment. At a high humidity the solid dissolves into a liquid, while at a lower humidity the salt recrystallizes. Compounds that exhibit such behavior are termed hygroscopic. The rapid uptake of water to enter a solution is called deliquescence, while the rapid expulsion of uptaken water is called efflorescence. At the point of deliquescence, chemical potential of the crystalline salt equals that of the final solution and the chemical potential of the water in solution equals that of the vapor [18]. In other words, the water activity of the saturated solutions equals that of the air relative humidity at the point of deliquescence. At higher relative humidities, the particle continues to grow as more water from the surrounding enters to solution. The size of an inorganic salt aerosol can become many times greater than the original crystalline state, and its growth can be described by Köhler theory [19]. To evaluate the growth of a droplet beyond the point of deliquescence from a theoretical standpoint following [20], one may consider a salt solution droplet suspended in gas at a constant temperature T and total pressure P. For a constant water vapor partial pressure, the change in total Gibbs free energy of the system, G, requires

$$dG = \sum \mu_{i,g} dn_{i,g} + \sum \mu_{i,l} dn_{i,l} + \sigma d\Omega = 0 \tag{1.4}$$

where μ_i represents the chemical potential and n_i is the number of moles of component i. The subscripts g and l stand for gas and liquid respectively. In the third term σ is the surface tension while Ω is the interfacial area. Since the solutes are non-volatile, Equation 1.4 becomes

$$\mu_{w,g} dn_{w,g} + \mu_{w,l} dn_{w,l} + \sigma d\Omega = 0 \tag{1.5}$$

where w denotes water as the solvent. Equation 1.5 reduces to

$$\mu_{w,g} = \mu_{w,l} + \sigma \left(\frac{d\Omega}{dn_{w,l}} \right) \tag{1.6}$$

with the simplification $dn_{w,l} = -dn_{w,g}$. With the ideal gas assumption, the water gas phase chemical potential is given by

$$\mu_{w,g} - \mu_l^\circ = RTln\left(a_{w,g}\right) = RTln\left(\frac{p}{p^\circ}\right) \tag{1.7}$$

For the lquid phase,

$$\mu_{w,l} - \mu_l^\circ = RTln\left(a_{w,l}\right) = RTln\left(\gamma_{w,l}\chi_{w,l}\right) \tag{1.8}$$

where μ_l° refers to the state of pure water, T the temperature, R the gas constant, and a_w the water activity. In Equation 1.7 p° is the vapor pressure at temperature T. Meanwhile, in Equation 1.8 γ_w is the water activity coefficient and χ_w the mole fraction of water.

The change in surface area of a droplet with radius r is given by

$$d\Omega = 8\pi r dr \tag{1.9}$$

and the change in volume by

$$dV = 4\pi r^2 dr \tag{1.10}$$

Representing the volume of the droplet as a summation of the partial molar volumes of water, $\bar{v}_w$, and solute, $\bar{v}_s$, Equation 1.10 can be expressed as

$$dV = \bar{v}_w dn_w + \sum \bar{v}_s dn_s = \bar{v}_w dn_w \tag{1.11}$$

Eliminating dr with Equation 1.9, Equation 1.11 becomes

$$\frac{d\Omega}{dn_w} = \frac{2\bar{v}_w}{r} \tag{1.12}$$

To show the equilibrium size r_e of a droplet with composition χ_w at a relative humidity $p/p^\circ = a_w$, Equations 1.7, 1.8, and 1.12 can be substituted into Equation 1.6 resulting in

$$ln\left(\frac{p}{p^\circ}\right) = ln\left(\gamma_w \chi_w\right) + \frac{2\bar{v}_w \sigma}{RTr_e} \tag{1.13}$$

It is important to note that $\bar{v}_w$ is neither the molar volume of pure water or the solution, but the partial molar volume of water. However, for dilute solutions using molar volume of pure water is an appropriate practical approximation. Neglecting curvature effects, Equation 1.13 becomes

$$p = p^\circ \gamma_w \chi_w \tag{1.14}$$

which is Raoult's law when χ_w approaches unity. In general, curvature effects can be neglected for particles larger than 0.1μm in diameter.

Figure 1.13 shows a typical growth curve of an inorganic salt with respect to relative humidity. At 75% relative humidity, the crystalline NaCl aerosol deliquesces and continues to grow exponentially with increasing relative humidity. Upon reduction in relative humidity, the aerosol does not recrystallize at 75% relative humidity. Instead, it exists as a supersaturated solution until approximately 45% relative humidity. The existence as a supersaturated solution is termed hysteresis [6].

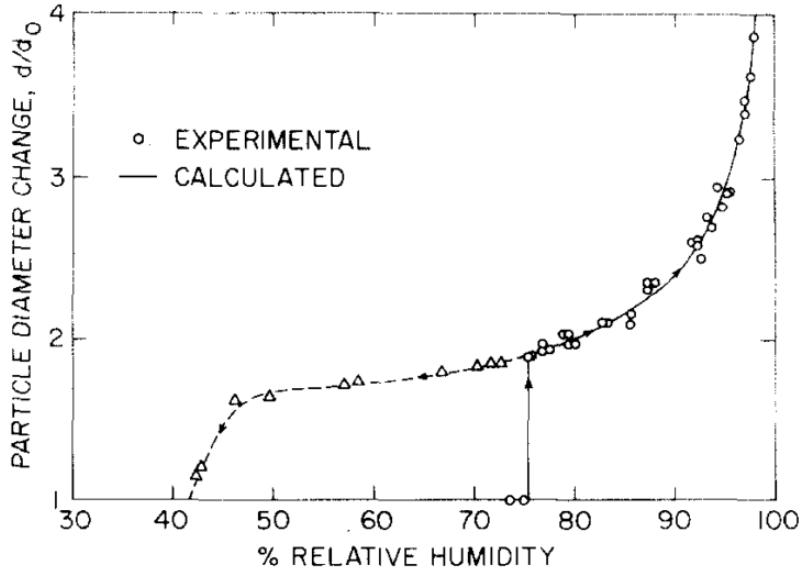

Figure 1.13: Growth and evaporation of a NaCl aerosol with respect to relative humidity at 25°C, taken from [6]

The deliquescence and subsequent growth is affected by the system's temperature. In the deliquescence process, the heat of condensation for the water from the atmosphere entering the solution is equal to the negative of its heat of vaporization, ΔH_v. The overall heat in the deliquescence process is

$$\Delta H = n\Delta H_s - \Delta H_v \tag{1.15}$$

where the integral heat of solution, ΔH_s, is the energy absorbed by the chemical reaction between the liquid water and solid salt of n moles to form an aqueous solution. Applying Clausius-Clapeyron we get

$$\frac{dln\,(p)}{dT} = -\frac{\Delta H}{RT^2} = \frac{\Delta H_v}{RT^2} - \frac{n\Delta H_s}{RT^2} \tag{1.16}$$

With the definition

$$\frac{dln\,(p^\circ)}{dT} = \frac{\Delta H_v}{RT^2} \tag{1.17}$$

Equation 1.16 can be expressed as

$$\frac{dln\,(a_w)}{dT} = -\frac{n\Delta H_s}{RT^2} \tag{1.18}$$

Based on Equation 1.18, the deliquescence relative humidity decreases with an increase in temperature. Additionally, if the system were to contain more than one solute, the deliquescence relative humidity of a mixed salt system has been found to be lower than the deliquescence humidities of the individual components [21]. A number of models that build on the fundamentals discussed here exist to predict the state and size of an inorganic salt aerosol. An especially useful model is the Extended AIM Aerosol Thermodynamics Model, which allows the user to define the solute components at various water vapor partial pressures and temperatures [22].

The above thermodynamic considerations apply to equilibrium conditions. The rate at which the equilibrium is reached depends on the driving potential between the difference in the atmosphere's vapor pressure and the vapor pressure above

the solution. In determining the deliquescence humidity of NaCl particles, Linnow et al. recorded the time required to completely deliquesce NaCl. The time required for deliquescence was obtained by observing RH-XRD peaks until they reached a steady state. Figure 1.14 shows the data from the RH-XRD experiments for NaCl.

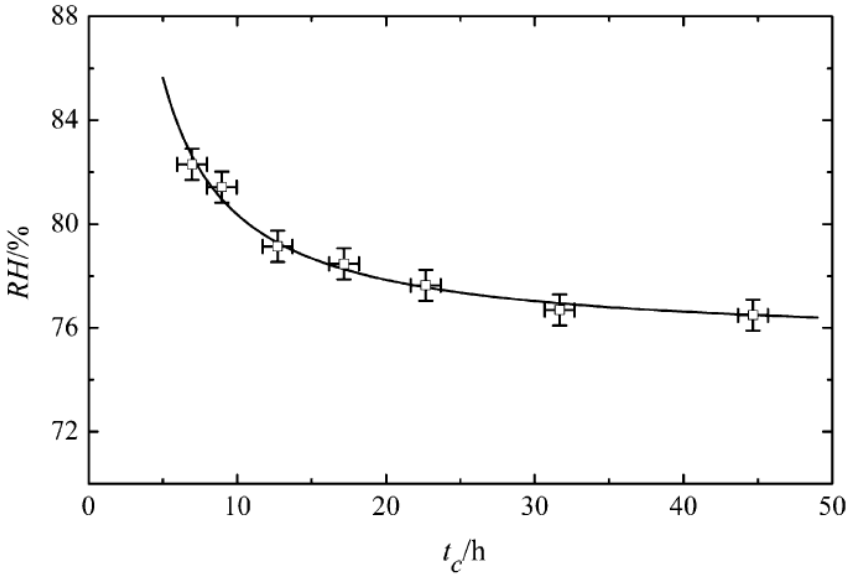

Figure 1.14: Time required to completely deliquesce NaCl at varying relative humidities, taken from [7]

The data in Figure 1.14 takes the form

$$RH = Ae^{\frac{B}{t_c}} \tag{1.19}$$

which can be linearized to

$$ln\,(RH) = ln\,(A) + \frac{B}{t_c} \tag{1.20}$$

In the above equations, t_c is the complete reaction time and A and B are constants. The linearized form in Equation 1.20 can be extrapolated to $B/t_c = 0$, at which

$ln(A) = ln(RH_D)$ giving the deliquescence humidity [7]. Based on the experimental data and curve fit, it is clear that the rate of deliquescence is strongly dependent on the gradient $y_{\text{inf}} - y_D$, the difference in the the surrounding and deliquescence vapor pressures. However, the analysis in Figure 1.14 does not give any consideration to the mass of the solute. Additionally, a deposited NaCl particle would be expected to have a different deliquescence time constant than an aerosolized one as the surface area open for mass transfer differs. In another study, Linnow et al. showed that NaCl crystals deposited on porous media also have time scales on the order of hours to completely deliquesce [23]

On the other hand, El Golli et al. experimentally determined the time required for evaporation for NaCl aerosols below the efflorescence point. The data was plotted against a theoretical model developed by the authors for a single solute saline droplet evaporation. The model and experimental results for relative humidity below the efflorescence point of NaCl are shown in Figure 1.15

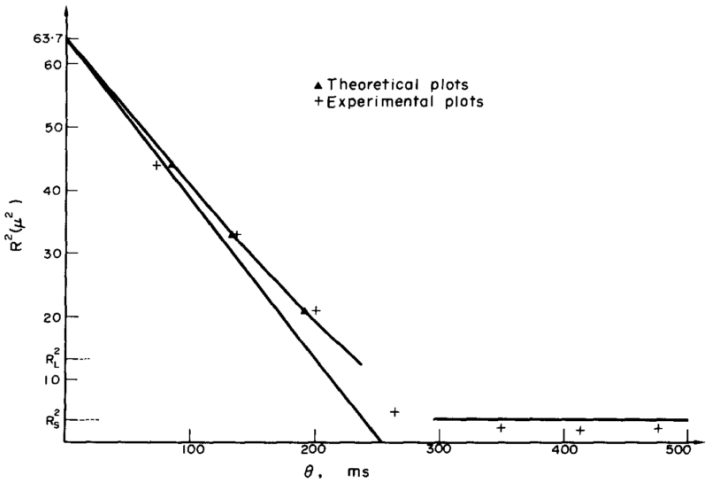

Figure 1.15: Time required for a NaCl droplet to evaporate in air with T=26°C, RH=29%, $m_\circ$=30g/kg, taken from [8]

The experimental data in Figure 1.15 were obtained by measuring the aerosol size at increasing distances downstream of the initial measurement. With constant flow rate, the time required for evaporation could be determined. From both theoretical and experimental standpoints, it is clear that the evaporation time of droplets less than 10μm in size is less than 0.5s, since an aerosol with a nominal size of 8μm evaporated in approximately 0.3s.

1.5 Filtration of Hygroscopic Particles

Compared to the filtration of solid and liquid aerosols, the filtration of hygroscopic aerosols has not been as extensively researched. Given a particular aerosol's phase transformation dependence on relative humidity, one can imagine the filtration being similar to solid aerosols at low humidities and at very high humidities similar to wet aerosols. Additionally, the filtration problem can be altered for already captured aerosols if there were to be a swing in the relative humidity of the carrier air stream. For example, captured solid aerosols may deliquesce in a humid air stream, become a liquid, redistribute in the filter, and change the pressure drop.

Gupta et al. studied the evolution of pressure drop as a function of collected mass for both hygroscopic and nonhygroscpic aerosols on flat HEPA filters [24]. Joubert et al. experimentally characterized pressure drop evolution for flat and pleated HEPA filters loaded with NaCl aerosols under wide range of humidities [9]. Figure 1.16 shows the change in pressure drop before deliquescence while Figure 1.17 illustrates the growth in pressure drop at humidities above the deliquescence point at a gas velocity of 0.07m/s.

The linear relation between loaded mass and pressure drop in Figure 1.16 indicates the aerosols are solid. A decrease in cake resistance associated with increasing

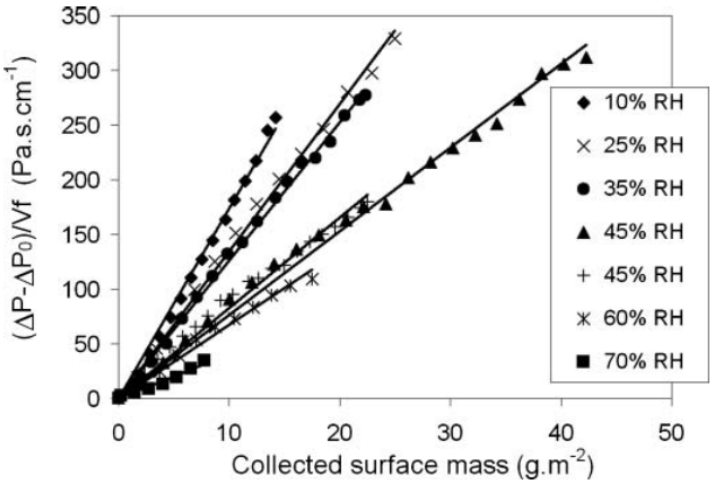

Figure 1.16: Pressure drop dependence of a flat HEPA filter on accumulated mass below deliquescence for NaCl aerosols, taken from [9]

relative humidity, can be noted which corresponds to the slope of each line. One would expect that below the deliquescence point of the aerosol, the development of pressure drop with respect to mass loading would be equal across the range of relative humidities if the aerosol is in crystal form. With increasing relative humidity below the deliquescence point, the cake resistivity decreases as indicated by the decrease in the slope in Figure 1.16. The decrease in cake resistivity below the deliquescence point might be explained by agglomeration of the individual aerosol particles. Craig et al. studied NaCl particles through gas adsorption and electron microscopy. In exposures of relative water vapor pressures of 5% to 25%, the surface area per mass was noted to decrease indicating agglomeration [25]. In a more recent study, Krämer et al. experimentally found the dynamic shape factors of NaCl aerosols carried in an air stream atomized from a solution to be greater than their cubic equivalent. The increase in dynamic shape factor indicates agglomeration of aerosols which is affected by the water vapour interaction with the crystal surface [26]. Due to agglomeration at increasing humidities below the deliquescence point the filter is loaded with ag-

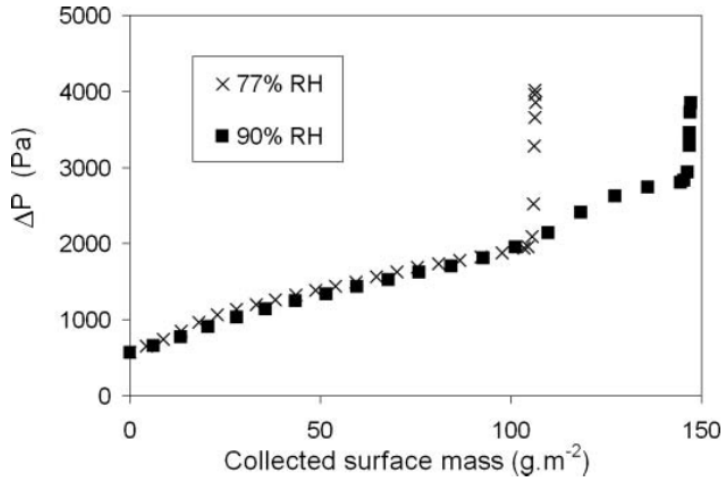

Figure 1.17: Pressure drop dependence of a flat HEPA filter on accumulated mass above deliquescence for NaCl aerosols, taken from [9]

glomerates instead of individual crystals. Therefore one may think of the loading at very low humidities is associated with particles resulting in a higher cake resistance as shown in Figure 1.6 than loadings closer to the deliquescence point.

Because of increase in pressure drop with added mass shows a sudden spike (cf. Figure 1.17), it is concluded that the hygroscopic particles behave like liquid aerosols above the deliquesence point. The work of both Gupta et al. and Joubert et al. showed the spike in pressure drop to occur at higher collected mass for higher relative humidities. Figure 1.18 shows a pleated HEPA filter being loaded under a variety of relative humidities.

Interestingly, at relative humidites in the range of 60-70%, while the slope of the pressure drop increases with loading at relative humidities above the deliquescence point, there is a sharp increase at higher loading.

Brekke et al. studied the effect of humidity on filters used in offshore gas turbine applications. For gas turbines, clean air is required to provide efficient com-

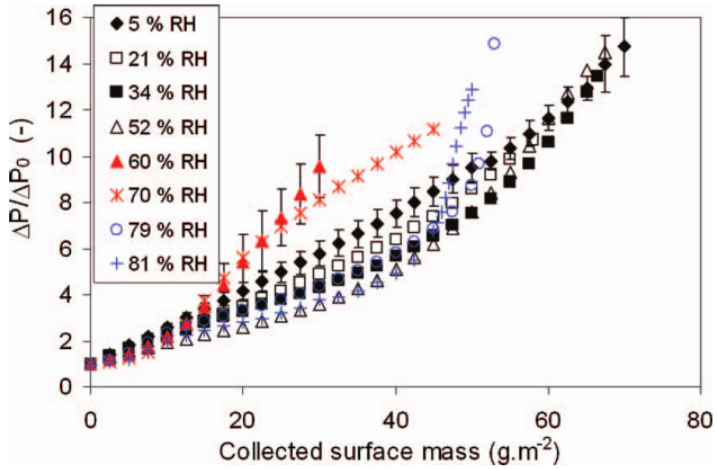

Figure 1.18: Pressure drop dependence of a pleated HEPA filter on accumulated mass at varying relative humidities for NaCl aerosols, taken from [9]

bustion and to protect components from wear. In a marine environment, a number of hygroscopic salt aerosols exist which need to be removed by the filters. However, marine environments also have humidities up to the saturation point altering the physical state of captured hygroscopic aerosols. In the study the authors subjected filters obtained from four different locations to simulated fog conditions. The air velocities tested ranged from 3.5 to 6.0m/s. Under the saturated fog conditions, mass loss was measured from each filter indicating that at high velocities and humidities re-entrainment can be an issue for hygroscopic particles that may have been originally deposited in crystalline state [27].

1.6 Filtration Literature Review Conclusion

The preceding sections discuss the literature available on dry as well as wet aerosol filtration. For dry loading conditions, the pressure drop of a filter evolves linearly with respect to accumulated mass upon formation of a cake. Prior to forming a cake, the pressure drop increases at a lower rate. For wet aerosol loading, the

pressure drop grows slowly with added mass until a sharp spike occures when the liquid wets the filter surface. Eventually the spike plateaus for wet loading to a constant value where the filter cannot hold any more additional mass and previously collected aerosol is drained out of the filter. The discussion is also expanded to hygroscopic aerosols. Depending on the relative humidity, a hygroscopic particle may act like a dry or wet aerosol. After covering the theoretical background of deliquescence and efflorescence, the current literature on hygroscopic particle filtration is discussed.

Although a number of studies establish dry loading lines and wet loading pressure drop evolution curves for hygroscopic aerosols, no studies determining the effect of dynamic excursions in gas air chemistry exist. Therefore this work aims to experimentally determine the effect on humidity fluctuations above the deliquescence point of hygroscopic aerosols deposited onto HEPA filters below the point of efflorescence. The experiments record the pressure drop evolution and mass fluctuation to swings in gas humidity to values above the deliquescence point and then again below the efflorescence point. The scope of the work validates whether any mass loss could occur from the filter due to the deliquescence and efflorescence cycles.

Chapter 2

Hygroscopic Aerosols Captured In HEPA Filter

Since cleanroom contaminants may be hygroscopic, such as NH_4Cl, the performance of HEPA filters under air humidity excursions was experimentally studied. Such air humidity excursions could be a result of an abrupt swing in outdoor humidity or a water spill within the facility.

2.1 Experimental Set Up

A flow loop was constructed to provide a constant air flow rate with dynamically variable air humidity. A schematic diagram of the flow loop is shown in Figure 2.1, and the physical layout of the final constructed experimental set up is shown in Figure 2.2. The air enters through the blower after which the air can be directed through either the humidifier or air dryer by opening and closing appropriate valves. To accommodate for desired air velocity as well as different pressure drops through the humidifier and air dryer, the power of the blower can be controlled with a variable transformer. The air dryer consists of a 11.43 cm outside diameter schedule 40 PVC pipe filled with desiccant (Du-Cal Drierite, W. A. Hammond Drierite Co., Ltd.). The humidifier consists of an atomizer (Six-Jet Atomizer 9306, TSI, Inc.) outputting to a 16.83 cm outside diamter schedule 40 PVC pipe to allow for a longer time of flight for the aerosolized water to evaporate. A HEPA filter precedes the atomizer to remove contaminants in the high pressure air and deionized water is used as the atomizing fluid. The relative humidity of the humidifier can be controlled through the atomizing

pressure and number of nozzles in operation. Additionally, any combination of flow rates through the humidifier and the air dryer can be used providing a wide variety of operating conditions.

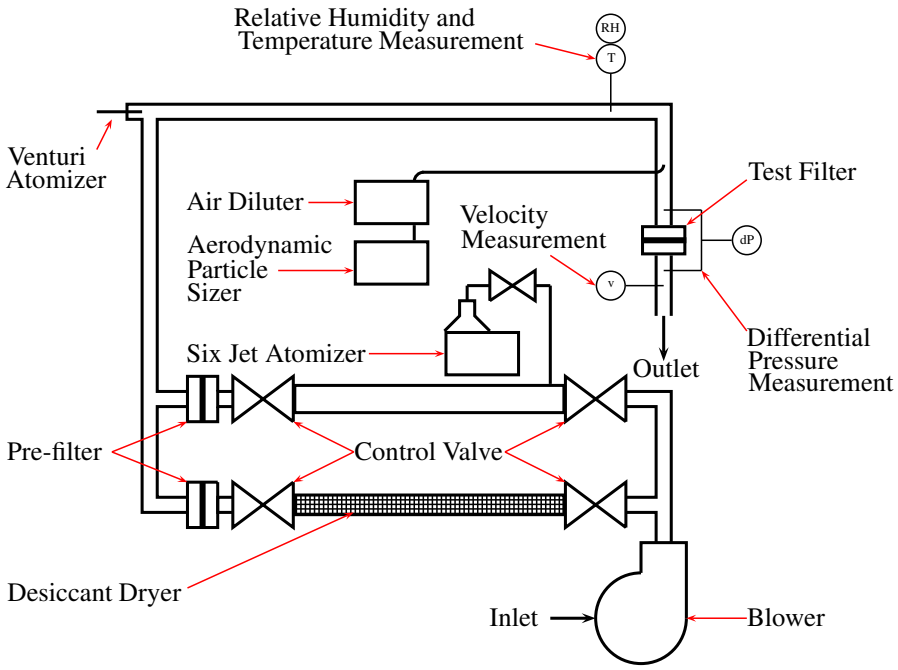

Figure 2.1: Symbolic illustration of the flow loop used to test HEPA filters

After the humidifier and the air dryer, the air passes through HEPA pre-filters to remove contaminants present in the ambient air. After the pre-filters, the desired contaminant aerosol is injected with a venturi atomizer consisting of two needles shown in Figure 2.3. The air needle is 21 gauge and the salt solution needle is 30 gauge. The gauges correspond to 0.81 mm outside and 0.58 mm inside diameters for the air needle and 0.31 mm outside and 0.15 mm inside diameters for the salt solution needle. As with the Six-Jet atomizer, the high pressure air passes through a HEPA filter before atomizing the fluid and the flow rate can be controlled with a pressure regulator. The atomizer generates polydisperse aerosols, and the size can be

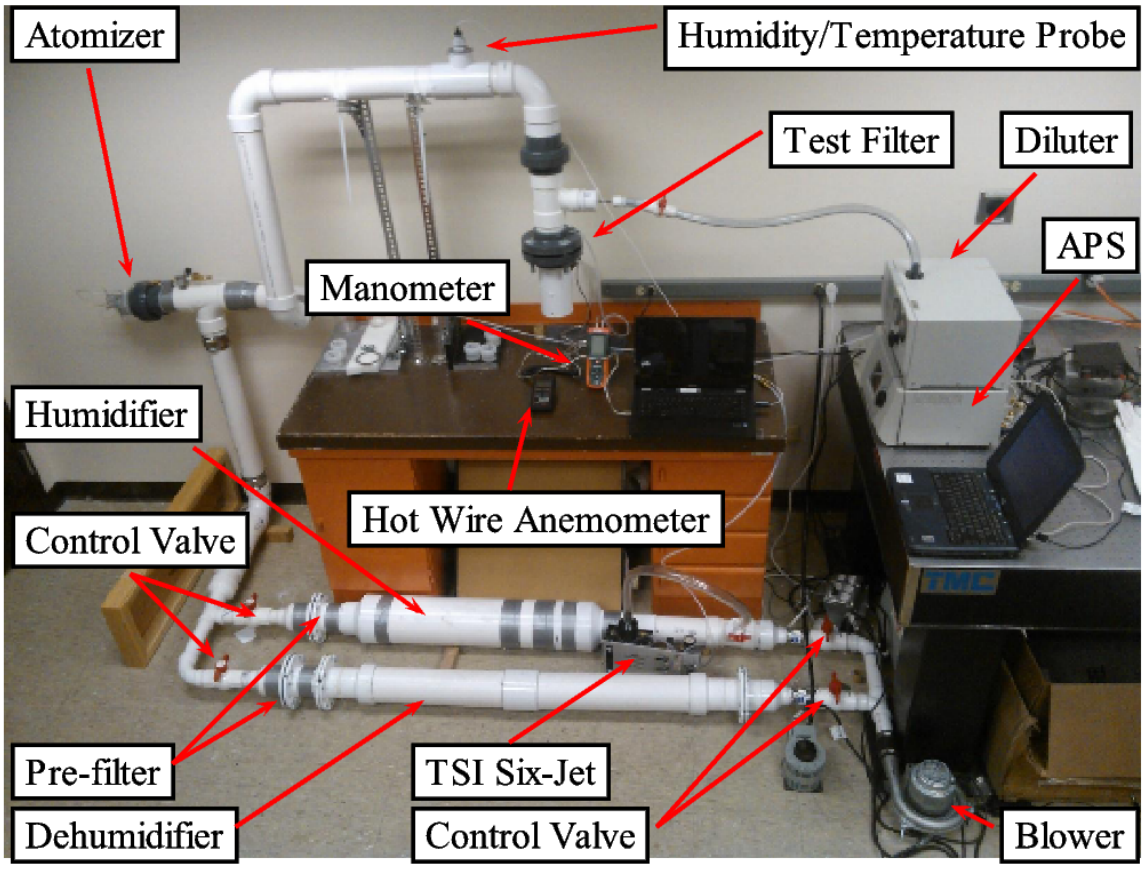

Figure 2.2: Image of the actual constructed experimental set up

controlled with the salt solution concentration or the atomization pressure.

Downstream from the atomizer, the relative humidity and temperature of the air stream is measured. During atomization, the humidity and temperature sensor was moved downstream of the filter to not expose it to the corroding test aerosols. Next, the air passes by an inlet tube for an aerodynamic particle analyzer set up for isokinetic sampling (APS 3320, TSI, Inc.). The APS can measure particles from 0.5 to 20μm aerodynamic size. The total flow rate through the APS is 5 lpm, therefore a tube with inner diameter of 0.775 cm was chosen to match the 0.45 cm/s velocity within the flow loop. Additionally, the tube diameter had to be appropriately sized to minimize

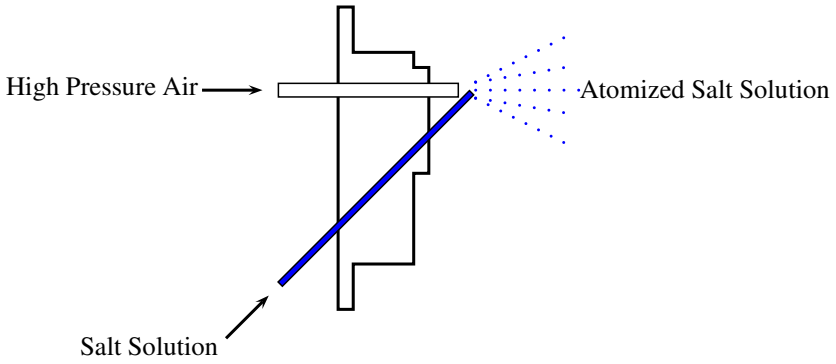

Figure 2.3: Illustration of the polydisperse venturi atomizer used for generating hygroscopic salt aerosols.

aerosol deposition within the sampling tube, which would bias the size distribution measurement. Assuming plug flow and neglecting effects of gravity and turbulent difusion, the velocity around a bend can be derived by balancing the centrifugal force with the fluid drag force

$$v_{bend} = \frac{sU_{tube}}{R_{bend}} \tag{2.1}$$

In the above equation, v_{bend} represents the outward velocity of the particle, s represents the stop distance, U_{tube} is the velocity in the straight pipe, and R_{bend} is the mean radius of the bend. The problem is depicted in Figure 2.4.

If the particle stop distance is on the order of half of the tube diameter, the particle may not be able to follow the airflow through the bend. The characteristic time, t_{bend}, for a particle to flow around the bend is given by

$$t_{bend} = \frac{\pi R_{bend}}{2U_{tube}} \tag{2.2}$$

Subsequently, the radial distance the particle travels in the bend is

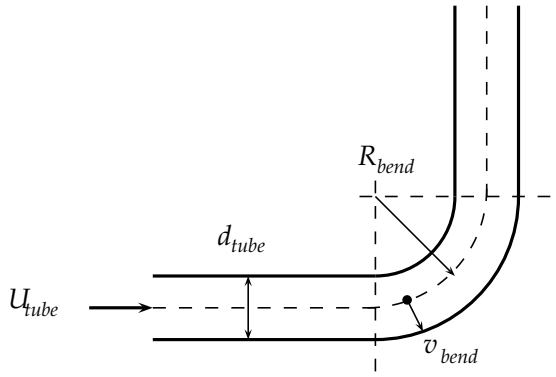

Figure 2.4: Bend in sampling tube, adapted from [10]

$$s_{bend} = v_{bend} t_{bend} \tag{2.3}$$

A nondimensional stopping distance is the Stokes number, St. For St much greater than 1, a particle is unable to navigate changes in gas stream direction while particles with St much less than 1 follow the gas stream lines. The Stokes number is defined as

$$St = \frac{s}{l_{ch}} \tag{2.4}$$

where l_{ch} is a characteristic length scale of the system. In the case of the aerosol sampling tube, the characteristic length scale is taken as the inner diameter of the tube.

The stopping distances along with their Stokes number for a range of particles are given in Tables 2.1 and 2.1 below. Particles larger than 20μm in size are not anticipated to be generated. Given the calculations, particles over 15μm in diameter should not be generated. Larger particles have a stop distance approaching the tube

radius of 3.86mm and may be therefore deposited in the bend at far greater rates than smaller particles [10, 28].

Table 2.1: Stop distances for NH_4Cl aerosols in l_{ch}=3.86mm flow.

NH_4Cl		
Particle Diameter [μm]	**Stop Distance [mm]**	**Stokes number**
1	0.003	0.0005
5	0.076	0.0120
10	0.302	0.0500
15	0.680	0.1120
20	1.209	0.2000

Table 2.2: Stop distances for NaCl aerosols in l_{ch}=3.86mm flow.

NaCl		
Particle Diameter [μm]	**Stop Distance [mm]**	**Stokes number**
1	0.004	0.0007
5	0.107	0.0180
10	0.429	0.0700
15	0.965	0.1580
20	1.715	0.2800

At the start of the project, the APS was not operable because the total flow pump was burned out. The burned out pump was replaced with a higher capacity rotating vane pump. Two needle valves were added to the configuration to allow for control of the air flow rate. A control valve was added to control the total air flowing through the APS, while a bypass valve was added to allow the pump to draw a higher flow rate. The original schematic is shown in Figure 2.5 while the modified schematic is shown in Figure 2.6. The APS operates with a diluter (TSI 3302A) at 100:1 ratio to ensure aerosol concentration below 1000pt/cm^3 for accurate measurement.

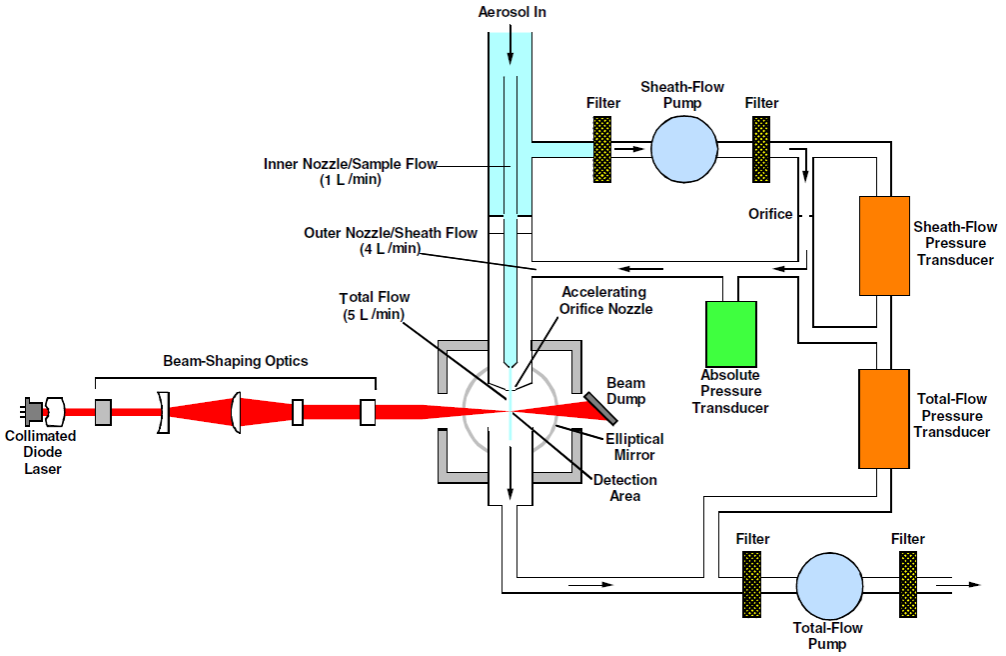

Figure 2.5: Original schematic of the APS 3320, taken from [11]

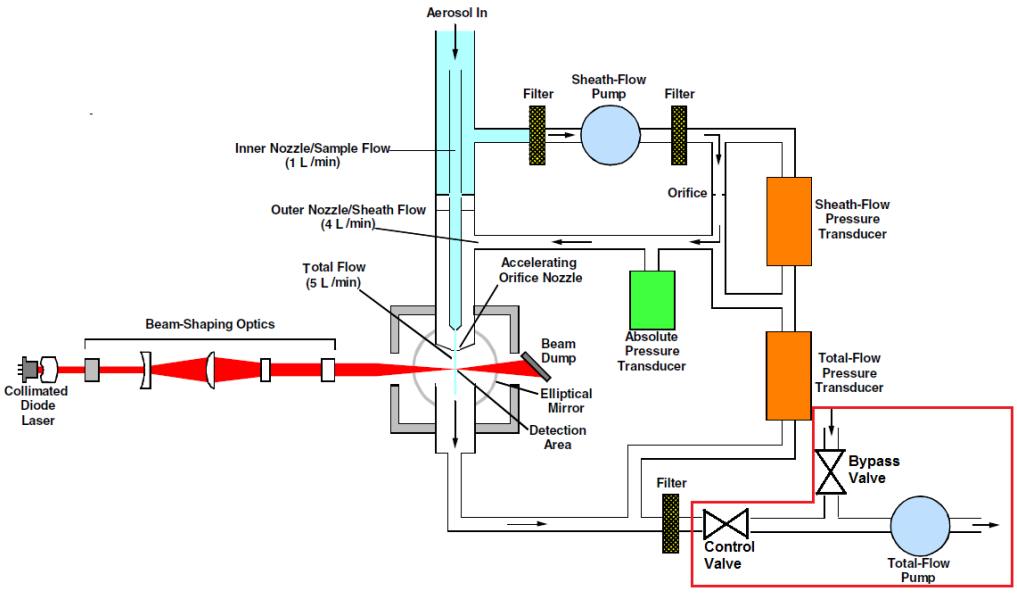

Figure 2.6: Schematic of the modified APS 3320, modified from [11]

The modified the APS was calibrated with 3μm, 5μm, and 9.9μm spherical latex particles from a particle-water suspension. The measured particle concentrations as a function of particle size are shown in Figures 2.7 through 2.9 for each calibration particle size. When atomizing 3μm and 5μm particles into the air stream, a peak at the corresponding diameters can be seen in Figures 2.7 and 2.8. The peak near 1μm particles can be attributed to condensation nuclei resulting from the atomization. However, for the 9.9μm particles no peak is detected at the correct diameter, only the condensation nuclei are recorded as illustrated in Figure 2.9. Therefore atomization of particles in the range of 10μm and larger should be avoided to guarantee proper size distribution measurement.

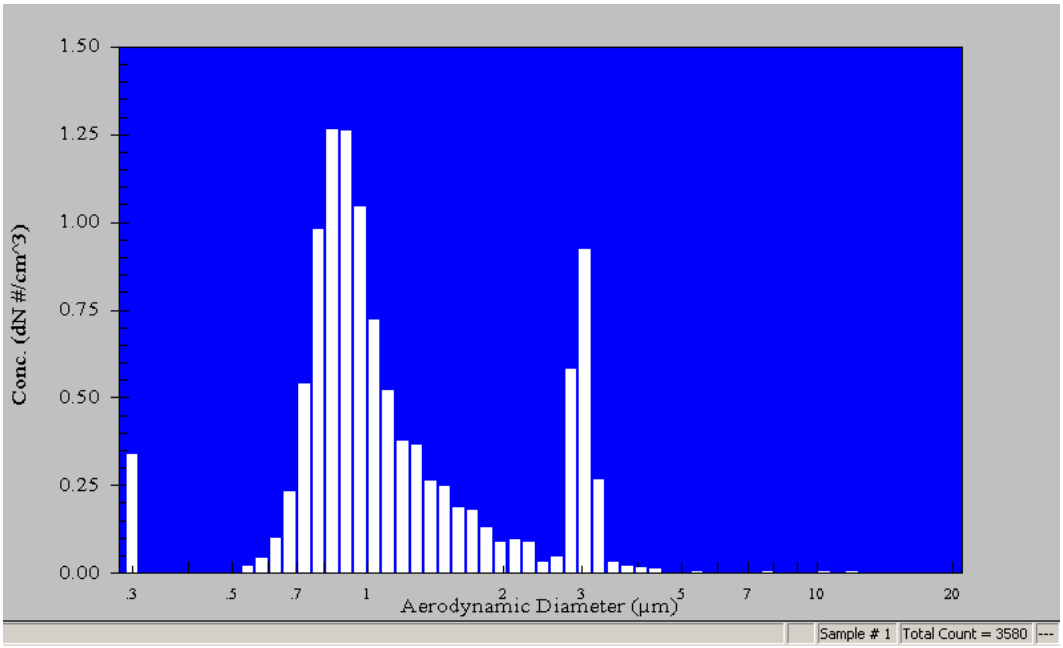

Figure 2.7: APS calibration data for 3μm particles

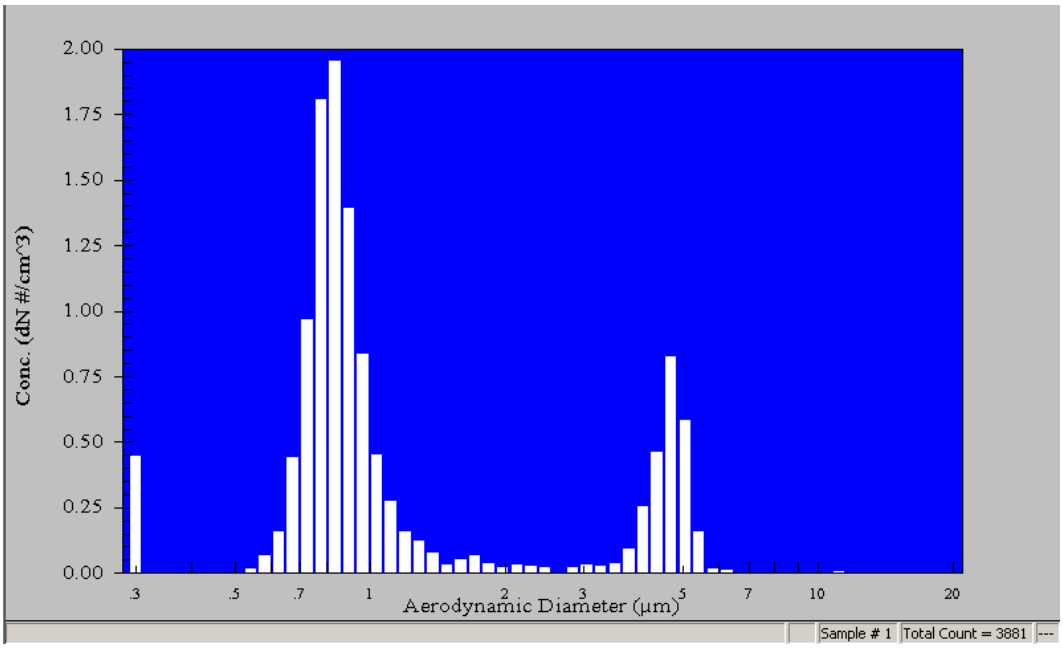

Figure 2.8: APS calibration data for 5μm particles

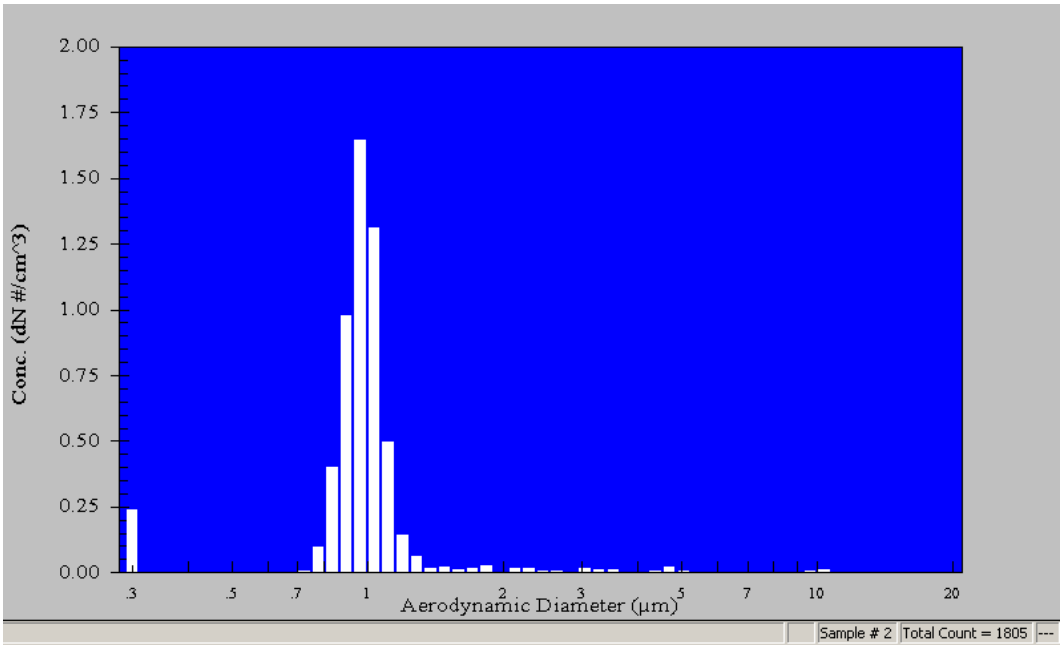

Figure 2.9: APS calibration data for 9.9μm particles

Since the APS inlet tube is upstream of the filter, the total pressure can be significantly higher than the atmospheric pressure especially at higher filter mass loadings. Due to the high inlet pressure, correct flow rates through the air diluter and APS could not be obtained while loading the filters. Therefore the atomized salt used to load the filters could not be continuously characterized. Assuming that the atomized particles and the system losses are independent of the system total pressure, the atomized salt size distribution was obtained with the APS when no filter was placed into the flow loop. Since the atomization pressure and solution concentrations were kept constant, the atomized salt distribution was assumed to be constant from run to run and the MMD was taken as an average of ten samples with the standard deviation as the uncertainty.

After the APS inlet tube, the sample flows through the test HEPA filter used for diagnostics. Pressure drop across the filter is monitored with a digital manometer. Below the filter the air velocity is recorded with a hot wire anemometer after which the air enters the exhaust. Dowstream of the humidifier and air dryer the flow loop is constructed of 8.89 cm outside diameter schedule 40 PVC pipe. The filter holder consists of two 8.89 cm outside diameter schedule 80 PVC flanges in which the filter is supported with a metal mesh. To ensure that all the air passes though the filter, a stainless steel shim with an internal diameter of 70mm presses the filter down once the flanges are clamped together. Therefore the total exposed filter face area is 3848.45 mm^2. The test filters were Millipore AP25 glass fiber filters with binder. The manufacturer reports the retention rating as 0.8-8.0μm, thickness as 1200μm, binder content as 110g/cm^2, and weight as 140g/m^2. Also, at 0.053m/s air flow rate the clean air resistance is reported to be 343Pa and DOP penetration as 0.03%.

The velocity measurements were made with a Dwyer 471 digital thermo-

anemometer. For the anemometer, the manufacturer specifies a ±3% full scale accuracy. The diameter of the filtration area is 70mm while the diameter of the pipe at the point of velocity measurement is 88.9mm. Therefore to achieve a 0.45m/s filtration velocity at the filter, the hotwire should be reading 0.28m/s assuming a flat velocity profile. With the 3% accuracy, the velocity reading of the hotwire is within ±0.0084m/s of the reading. However, a ±0.0084m/s inaccuracy in the anemometer reading corresponds to ±0.014m/s at the filter due to the diameter difference. Additionally, the velocity was controlled to within ±0.01m/s, such that the total velocity uncertainty at the filter is ±0.021m/s when taken as the root of the summed squares of the two uncertainties. the velocity measurement was not adjusted to any error associated with the gas relative humidity. The anemometer reading can be affected by the gas relative humidity, but for the current study the effect is negligible compared to other uncertainties [29]. The pressure across the filter was recorded with a Extech HD750 digital manometer. For the manometer, the manufacturer reports an uncertainty of ±0.3% full scale with a resolution of 10Pa. With a range of 34.47kPa, the full scale accuracy of the manometer becomes 103Pa. In addition to the manometer uncertainties, the anemometer uncertainty has to also be considered to get the full pressure reading uncertainty. From the filter manufacturer data, 343Pa pressure drop at 0.053m/s corresponds to ±136Pa associated with the total velocity uncertainty (0.021m/s) based on Equation 1.2. Combining the pressure uncertainties due to the anemometer and the manometer gives an overall uncertainty of ±171 Pa. Based on 10 samples, the average pressure drop across a clean filter was found to be 2461±17Pa where 17Pa is the sample standard deviation. Using Equation 1.2 and the manufacturer's specification, the clean filter pressure drop should be 2912Pa. The discrepancy in the measurement and scaled reading represents a possible bias error in the velocity measurements. The relative humidities were made with an Omega RH-

USB, for which the manufacturer reports an acccuracy of ±3% for relative humidity and ±0.1°C for temperature. Table 2.1 shows the measured relative humidities and the expected relative humidities above the saturated solution based on experimental results reported by Greenspan [30]. The saturated solutions were allowed to sit for 72 hours, after which time the measurements were recorded. All the measured humidities are within the uncertainty of the meter except above LiCl. The discrepancy could be attributed to either the chamber not being sealed properly allowing water vapor to enter the chamber from the surroundings. Or, to the solution having been stored at an improper temperature thus altering its saturated relative humidity permanently. The mass measurements were made with a Denver Instruments TP-323 balance. The balance reads with 0.001g accuracy and the manufacturer specifies a repeatability of ±0.001g. For all the mass measurements, three readings were taken for each sample to ensure a repeatable mass measurement.

Table 2.3: Measured relative humidities and temperatures for saturated salt solutions.

Salt	**Temperature** [$^{\circ}C$]	**Measured RH** [%]	**Reference RH, [30]** [%]
LiCl	22.8	19.9	11.3
NaBr	21.5	60.8	58.7
NaCl	22.1	74.8	75.3
NH_4Cl	22.1	77.7	78.9

2.2 Filtration Experimental Results

To help assess the performance of HEPA filters over a lifetime, filter samples were subjected to different mass loadings after which time they were exposed to fluctuating humidity conditions. NaCl was used as a surrogate salt since it has been studied extensively by other researchers. First a filter was weighed after which it

was loaded with a desired amount of salt at 0.45m/s. Since the velocity could not be measured immediately above the filter, the measured velocity was adjusted based on equal volumetric flow rates assuming constant air density. Since the diameter of the pipe was wider at the velocity measurement point than at the filtration area, the recorded velocity indicated 0.28m/s which is equivalent to 0.45m/s at the filter location; this calculation assumes equal volumetric flow rates with a flat velocity profile and constant density. The particles were atomized from 100g/L aqueous solution with a pressure of 40psi. The particles were loaded at approximately 20% relative humidity to ensure that the particles were completely dry. After loading the filter was weighed again to determine the collected salt mass. The pressure drop results for loaded filters are shown in Figure 2.10, with the pressure drop increasing linearly with respect to mass loading as expected. The particle size was nominally 2.97 $\pm$ 0.42μm MMD. In the figure, data from two other studies discussed in Chapter 1 are inluded [9,24]. The pressure drop divided by the gas velocity increases at a faster rate for the previous studies than the study conducted here as the previous studies load the filters with smaller particles. To show repeatability of the current study, three individual test runs are included in the figure. Since the three test runs all collapse along the dashed best fit line, it can be concluded that the particles atomized from test to test are consistent.

After determining the mass of the cake layer, the filters were subjected to humidity fluctuations. First, each filter was exposed to a relative humidity above the deliquescence point of NaCl. Upon reaching a relative humidity of 77%, the humidifier was controlled to provide a relative humidity between 78% and 79% for five minutes. The mean relative humidities and temperature for each test filter are shown in Table 2.2. The actual measurements are provided in Appendix A. After the high humidity exposure, air below the efflorescence point of NaCl was flowed

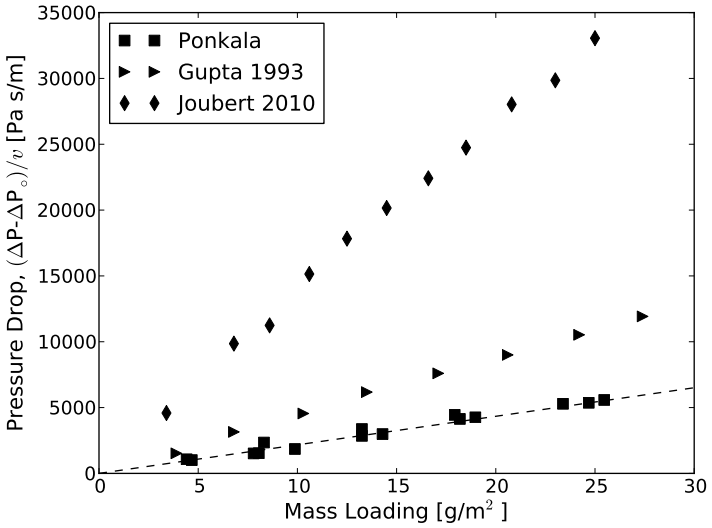

Figure 2.10: Pressure drop increase divided by the gas velocity as a function of mass loading for the current study as well as two previous published experiments.

through the filter until the pressure drop reached a constant value. The process was repeated twice, and then the mass of the filter was recorded. Intermediate mass recordings were not taken at the high humidity points to minimize redistribution of the deliquesced salt by capillary action. Throughout the fluctuations the filter velocity was kept at 0.45m/s. The humidity fluctuations are illustrated in Figure 2.11. The actual measured temperatures and relative humidities are included in Appendix A as functions of time.

The time variation of the total pressure drop across the filter along with the relative humidity for the lowest mass loading case are shown in Figure 2.12. The labels a) through g) corresponds to the regions in Figure 2.11. In region a), the salt solution is atomized, and the velocity is adjusted to correspond to 0.45m/s. Because the atomization rate is not constant, the relative humidity fluctuates. With increasing atomization rate, the relative humidity increases. Additionally, during at-

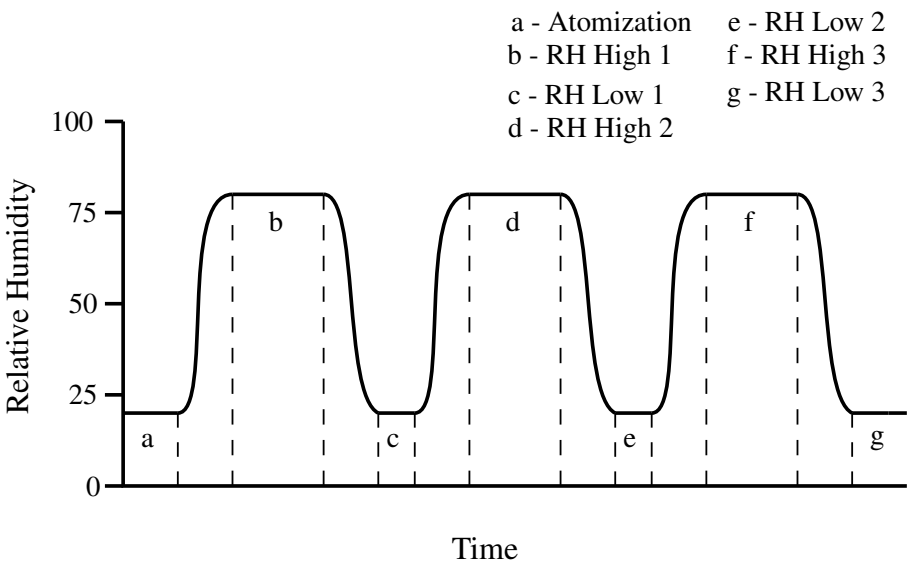

Figure 2.11: Humidity fluctuations with respect to time for the atomization and subsequent pressure drop change cases.

omization, the relative humidity is recorded downstream of the filter so that it will not be damaged by the aerosolized salt particles. Following atomization, the blower is shut off and the filter is weighed to determine its mass accumulation. Since the blower is off and the filter is not in place, the pressure reading is zero. Following the mass recording, the relative humidity probe is moved upstream of the filter and the blower is turned back on. Also, the control valves are adjusted to flow the air through the humidifier instead of the desiccant dryer. Before reaching a relative humidity above the deliquescence point of NaCl, the pressure drop across the filter decreases even though the air velocity is held constant, a phenomena reported by a previous study [31]. Upon deliquescing, the pressure drop increases as the volumetric fraction through which air can pass through is reduced as shown in region b). After 5 minutes, flow is diverted through the desiccant dryer instead of the humidifier and the pressure drop is recorded once the pressure drop reaches a steady value in

Table 2.4: Relative humidities and temperature for each test filter.

Mass Loading [$\mathbf{g/m^2}$]	**RH High 1** [%]	**RH High 2** [%]	**RH High 3** [%]	**Temperature** [$^{\circ}C$]
4.677	78.9	78.3	78.1	23.6
7.795	78.3	78.3	78.3	20.5
13.252	78.6	78.5	78.5	22.2
18.189	78.6	78.5	78.7	22.9
24.685	78.7	78.2	78.9	23.9

region c). After a steady pressure reading the same procedure is repeated twice to provide two more fluctuations after which time the blower is shut off and the filter is weighed to determine if all the atomized mass was retained in the filter. Between regions b) and c), d) and e), and f) and g) sharp spikes and drops are recorded in the pressure drop. The sharp changes are caused by suddenly redirecting the flow through either the desiccant or humidifier flow paths. The two paths have different flow resistances. As an example, upon switching to the desiccant path, more air can be pushed through the system the for same blower power resulting in an increase in velocity and pressure drop. To correct for this, the power of the fan is reduced until the correct air velocity os reached. Immediately before completely efflorescing the salt in the filter after the humidity spikes, the pressure drop is noted to drop to very low values, in some cases even below the clean filter pressure drop. The sharp drop can be attributed to a reading error in the anemometer as its reading is affected by changes in humidity causing it to read a higher value than the actual velocity. As noted earlier in the experimental instrumentation description, the velocity reading of an anemometer depends on the gas relative humidity [29]. After the air humidity steadies, the anemometer reads correctly and the velocity can be adjusted to give the true effloresced pressure drop. In future studies, the sudden dip in the anemometer

reading could be used as an indication when the salt in the filter is completely effloresced. The total pressure drops for the other mass loading cases are included in Appendix A for reference.

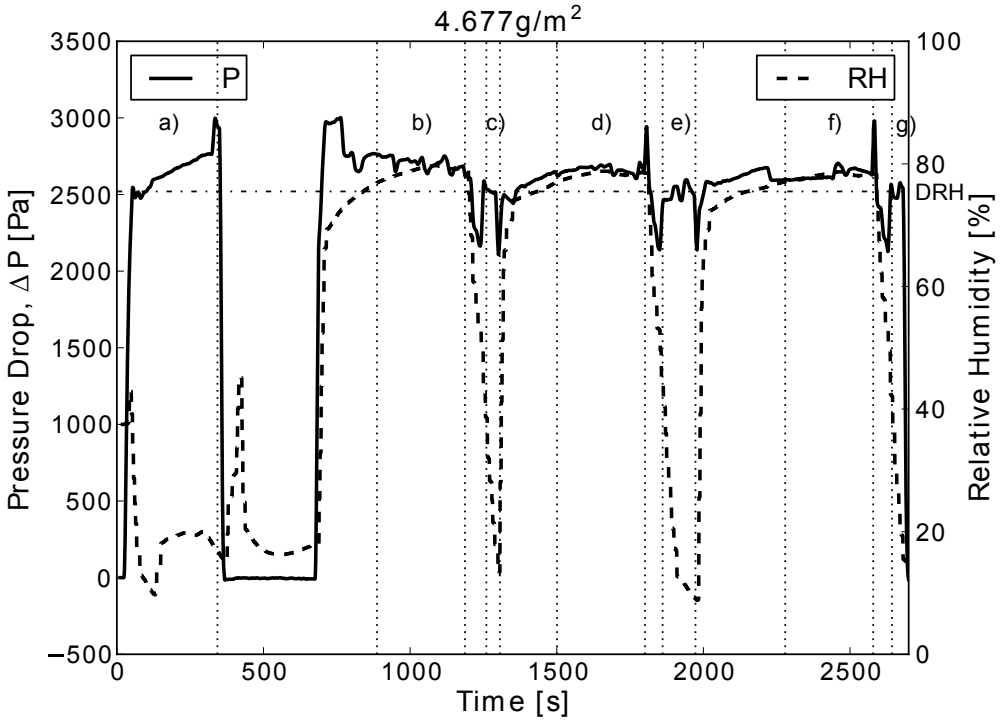

Figure 2.12: Total pressure drop for the lowest mass loading filter throughout the experiment.

Figures 2.13 through 2.17 show the pressure drop difference between the loaded and clean filter following atomization for all the mass loading cases. Again, labels b) through g) correspond to the regions in Figure 2.11.

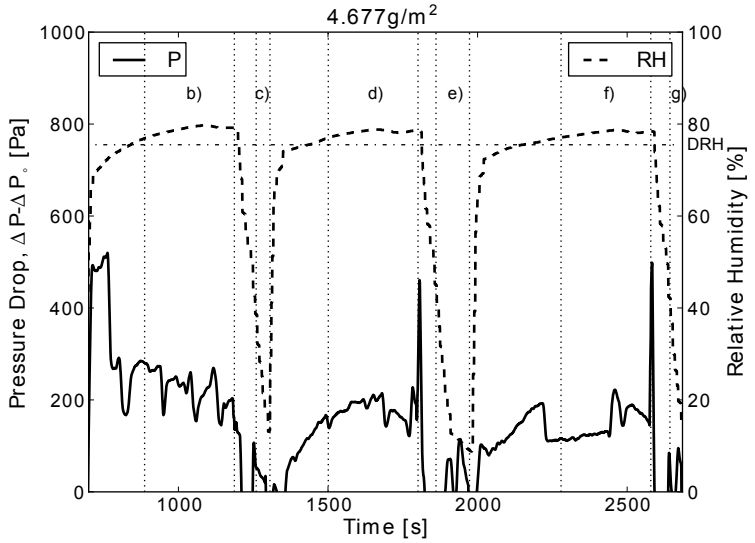

Figure 2.13: Adjusted pressure drop across the filter for 4.467g/m^2 loading case as a function of time.

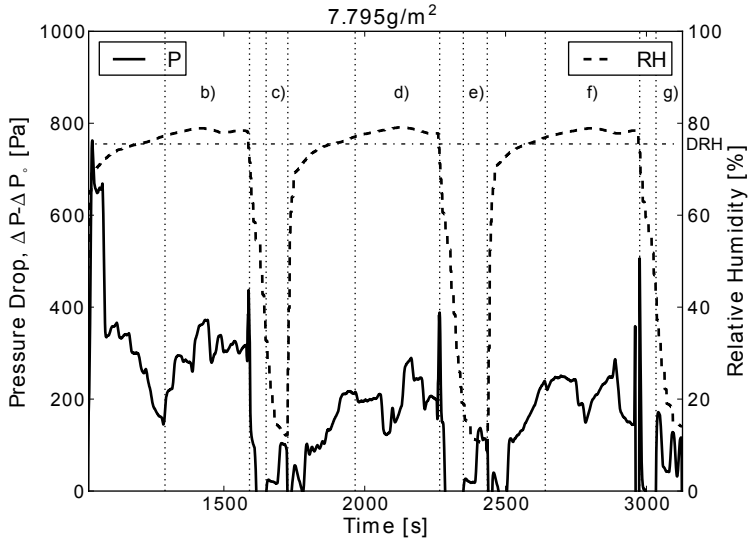

Figure 2.14: Adjusted pressure drop across the filter for 7.795g/m^2 loading case as a function of time.

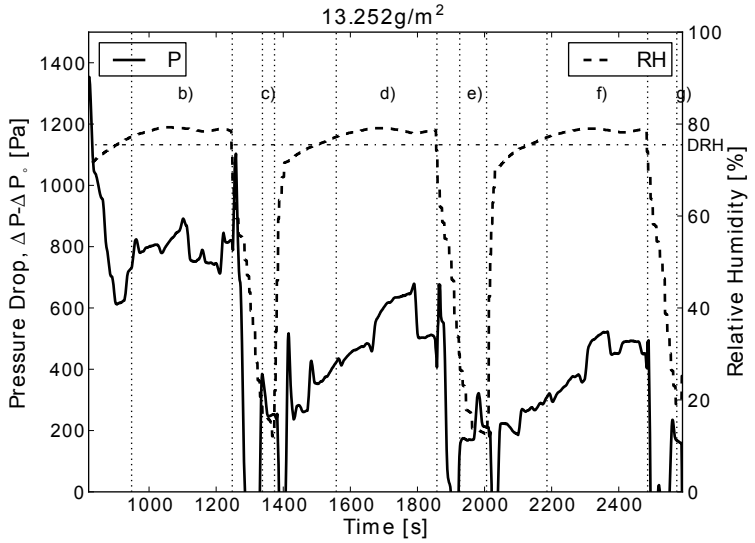

Figure 2.15: Adjusted pressure drop across the filter for 13.252g/m^2 loading case as a function of time.

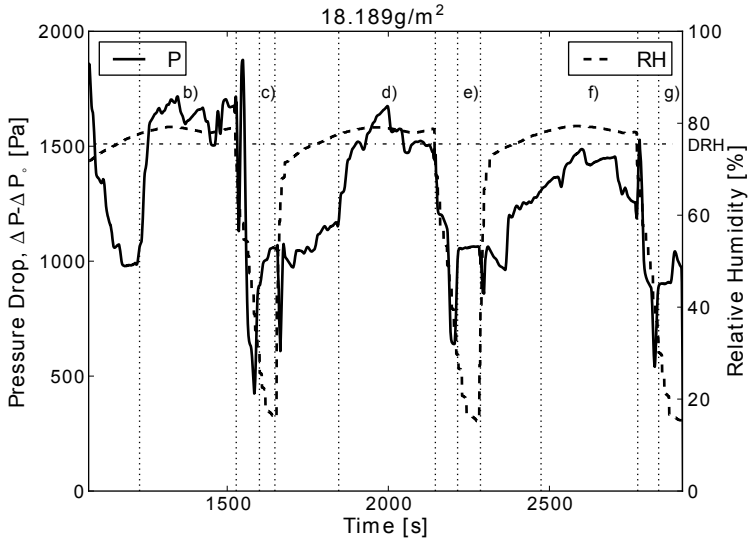

Figure 2.16: Adjusted pressure drop across the filter for 18.189g/m^2 loading case as a function of time.

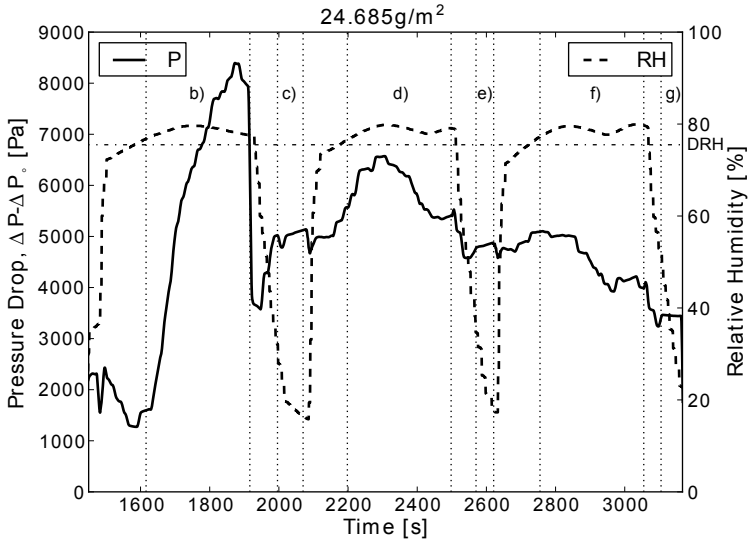

Figure 2.17: Adjusted pressure drop across the filter for 24.685g/m^2 loading case as a function of time.

The results of the pressure drop at the end of each successive humidity fluctuations are summarized in Figure 2.18. For all the cases except the highest mass loading, the pressure drop at the end of the first humidity spike is lower than that of the original cake. Also, for the same cases the pressure drop after the first low humidity exposure is less than both the original cake pressure drop and the first deliquesced pressure drop. For the three intermediate mass loadings the successive deliquesced pressure drops are less than after the first humidity spike. However, the effloresced pressure drop stays constant within the instrumentation uncertainty for the lowest four mass loadings. Only at the highest mass loading does the deliquesced pressure drop become larger than the cake pressure drop. Also, for all the effloresced points the pressure drop is greater than the cake pressure drop. Once again the pressure drop has a reducing trend with successive humidity fluctuations, except at the high mass loading the effloresced pressure drop also decreases.

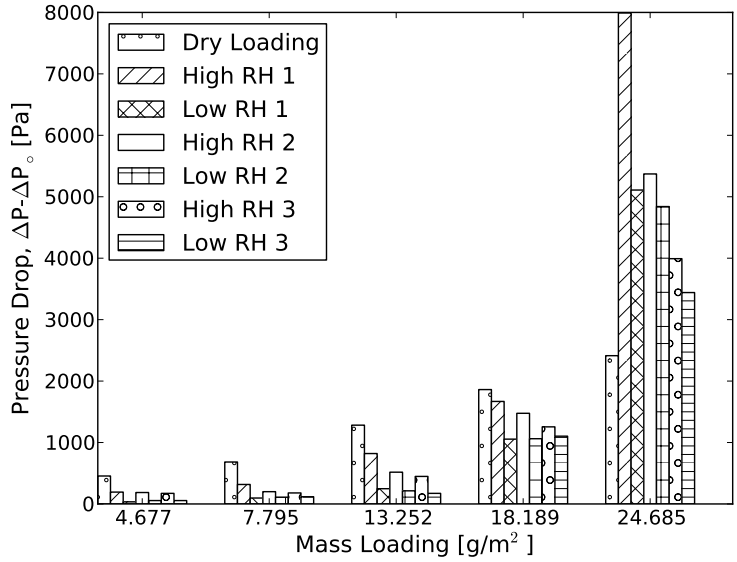

Figure 2.18: Pressure drop at the end of each successive high and low humidity exposure.

The decreasing ΔP trend with succesive humidity spikes possibly indicates that once deliquesced the salt redistributes itself in the filter to a state of lower flow resistance. At the four lower mass loadings, the deliquesced salt does not make the filter impermeable. Only at the highest mass loading does the filter become clogged as indicated by the sharp increase in pressure drop from the dry to wet state. For all these tests, no mass loss was recorded suggesting that even if the deliquesced salt may have traveled deeper into the filter media, it is not carried out of the exit stream of the filter. The possibility for re-entrainment penetration exists for the highest mass loading where each successive deliquesced state has a significantly lower pressure drop than the previous one. Still, the pressure drop across the filter at approximately 25g/m^2 for these tests is much lower than if the filter were to be loaded with liquid NaCl. For example, when loaded with 43.914g/m^2 deliquesced NaCl the pressure drop increased by 827.4 Pa from the clean pressure drop. Upon effloresing the loaded wet

mass was 10.9g/m^2. This test indicates that not all the NaCl loaded at the 25g/m^2 condition fully deliquesced. There is more discussion about this point later.

The data in Figure 2.18 are plotted in another format in Figures 2.19 and 2.20. Figure 2.20 is the same plot as Figure 2.19 except that the clogged filter at highest mass loading is eliminated to clarify the data for the lower dry mass loadings. From Figures 2.19 and 2.20 relaxation in pressure drop with each successive humidity swing is even more evident. If a sufficient number of humidity fluctuations were to be added to the experimental tests and the filter is thick enough, one could expect the deliquesced pressure drop to always reach the same value and the effloresced value to drop to the same one as the previous effloresced state. This steady state is already found for the lowest mass loading case even after three fluctuations.

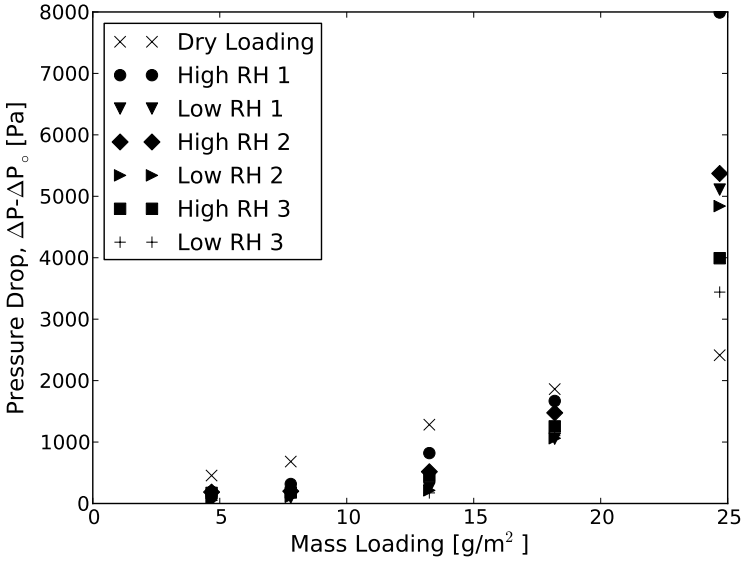

Figure 2.19: Pressure drop at the end of each successive high and low humidity exposures.

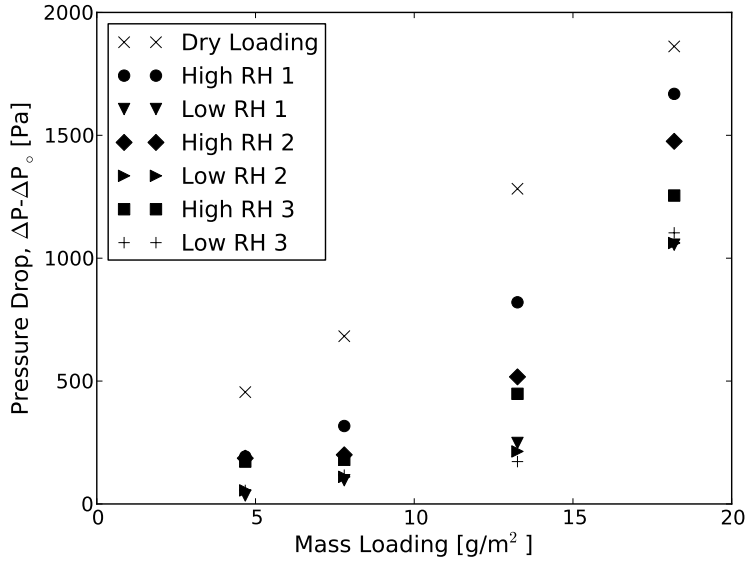

Figure 2.20: Pressure drop at the end of each successive high and low humidity exposures eliminating the highest mass loading.

The relaxation in pressure drop with each successive effloresced state is further illustrated in Figure 2.21 which shows the pressure drop at the end of each low humidity exposure. For all the cases except the highest mass loading the effloresced state pressure drop seems to have reached almost a constant value after the first low humidity exposure. Again, the data in Figure 2.21 is plotted eliminating the highest mass loading in Figure 2.22 to clarify the recorded pressure drops at the lower four mass loadings.

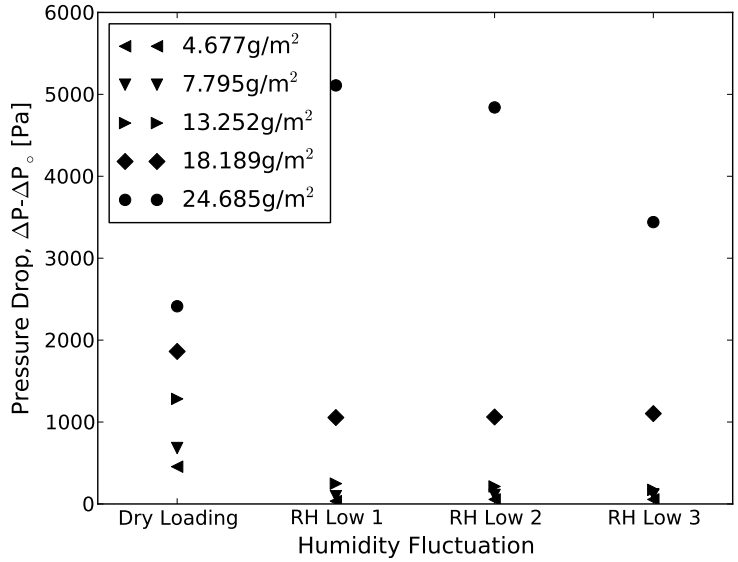

Figure 2.21: Pressure drop at the end of each successive low humidity exposures for each initial mass loading.

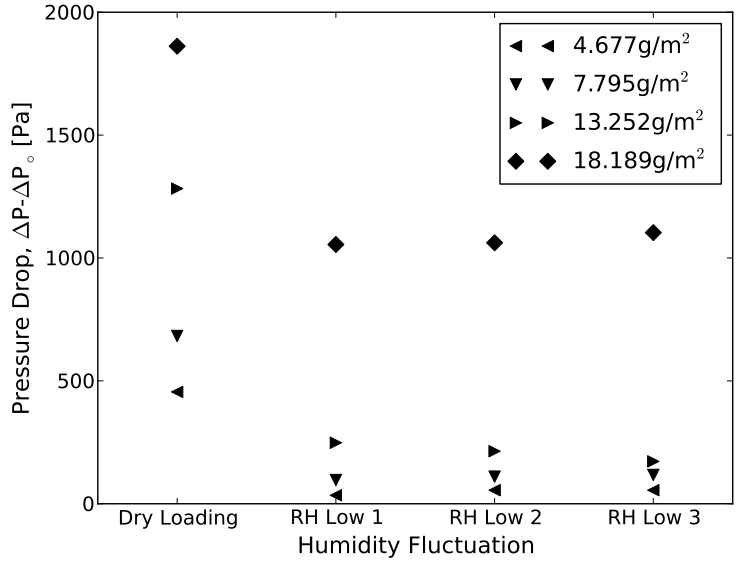

Figure 2.22: Pressure drop at the end of each successive low humidity exposures omitting the highest initial mass loading.

Figures 2.23 and 2.24 show the change in pressure drop at the end of each high humidity exposure. The deliquesced pressure drops appear to relax to a constant value with exponential decay. The number of fluctuations (or time) required to reach the constant value appears to be dependent on the initial mass loading. For low mass loadings, only one humidity fluctuation is enough to reach a constant fluctuation between deliquesced and effloresced pressure drops as shown by the lowest mass loading in Figures 2.22 and 2.24.

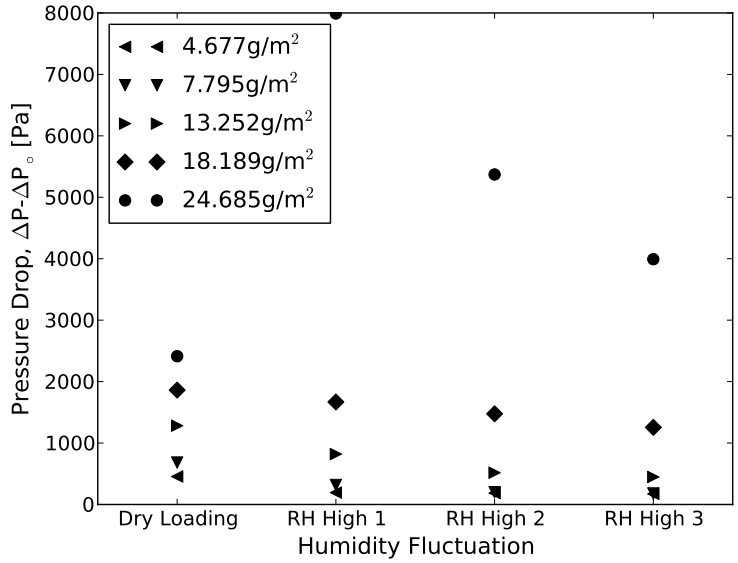

Figure 2.23: Pressure drop at the end of each successive high humidity exposures for each initial mass loading.

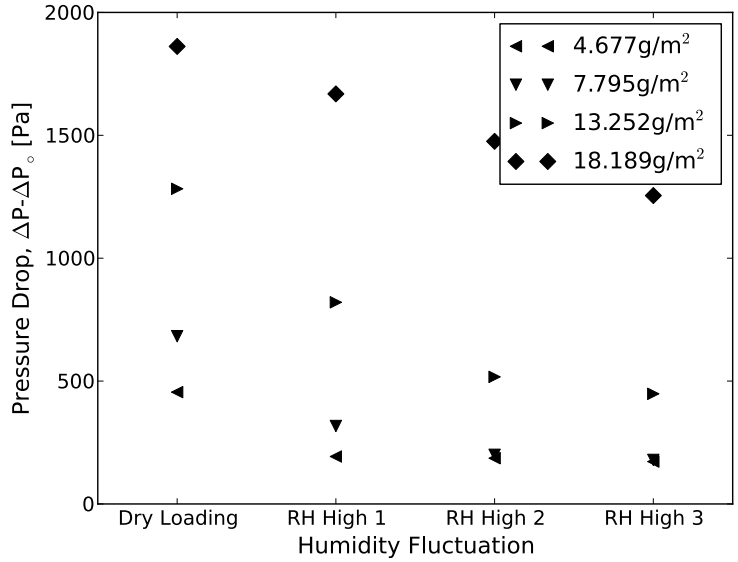

Figure 2.24: Pressure drop at the end of each successive high humidity exposure-somitting the highest initial mass loading.

An additonal filter was also loaded up to 28.843g/m^2 with effloresced NaCl particles. Following the first deliquescence and efflorescence cycle, no air flow was able to be pushed through the filter. It seems that after efflorescing, the salt film possibly formed an impenetrable crust on top of the filter preventing all air flow causing a higher pressure drop than the deliquesced film. Creating a clogged effloresced filter indicates that beyond a certain dry mass loading with hygroscopic particles, deliquescing followed by efflorescing may produce pressure drops larger than either initial dry or wet loading.

Another series of tests was conducted to quantify the mass gain of the NaCl cake after the first humidity increase. Before and after atomization the filter was weighed to determine the accumulated salt mass. After the initial mass recordings, the loaded filter was placed in a flow with humidity above the deliquescence point

for 5 minutes and then removed to weigh the deliquesced cake mass. The results are are shown in Figure 2.25. Based on the data, the highest percent increase occurs for the lowest mass loading, while at the high end the water uptake is less than half of the original cake mass. A possible explanation as deliquescence occurs, the solution creates a film on top of the yet to be deliquesced crystals, and this film has a lower surface area to volume ratio than individual droplets formed in the lower mass loading cases. This would suggest that mass transfer processes are inept in defining the time scale. Due to the low surface area to volume ratio, a much longer time would be required for the solution to reach equilibrium.

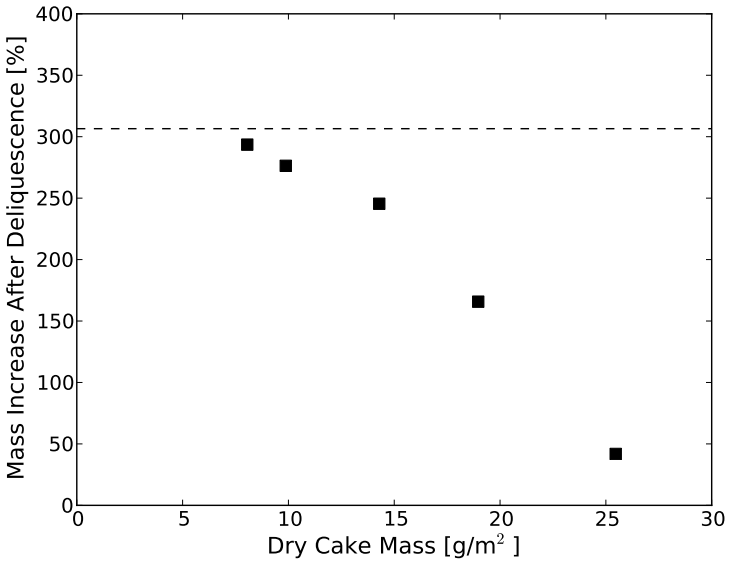

Figure 2.25: Comparison of mass increase with respect to mass loading following the first humidity spike.

From Figure 2.25, the time scales associated with filter deposited NaCl deliquescence become clearer. For a very low mass loading, the surface area with respect to volume is very large allowing for the deliquesced salt solution to almost reach equi-

librium even in 5 minutes at approximately 3% above the deliquescence point. For very high mass loading, as the cake enters solution upon onset of deliquescence the surface area to volume decreases leading to a much lower mass uptake rate.

2.3 Filter SEM Imaging

To visualize the effect of humidity fluctuations on the filter, a series of scanning electron microscope (SEM) images were taken immediately after atomization and following three humidity spikes. Large enough pieces were cut out of the filters to preserve the cake in its original state on the samples. The cut out samples with unaffected cake were then mounted onto SEM sample pins and coated with gold to eliminate charging during imaging. In between the final low humidity exposure and gold coating, the samples were exposed to humidities ranging from 20% to 50% during transportation. At such relative humidities the water vapor is not expected to cause any deformation in the cake since they are well below the deliquescence point. Figures 2.26 and 2.27 show the dry cake at mass loadings similar to those in Figure 2.10 at various levels of magnification. Images of a clean filter are provided in frames a) through d) in Figure 2.26. After the two lowest mass loadings, the individual filter fibers are not visible. Instead, the filter is coated entirely with the NaCl cake.

Figures 2.28 and 2.29 show the filters used in generating the data in Figure 2.10 after completing the humidity fluctuations. For the lower mass loadings in frames a) through d) and e) through h), remains of the original filter cake are hard to locate. Large crystals can be located on top of the filter, indicating effloresced coalesced droplets. The rest of the NaCl appears to coat the fibers or effloresce in webs spanning the fibers. Since the fiber material contains binder, locating the effloresced salt is difficult. In frames i) through l), islands of effloresced NaCl can be located. The

islands indicate formation of liquid film on top of the filter instead of wicking deeper into the media.

For the highest loading condition, (cf. Figure 2.29), all the frames show extensive effloresced salt crust on top of the filter. The crystals still appear to have their cubical shape with a film formed between individual particles. The retention of the cubical shape indicates that the crystals did not fully deliquesce explaining the lower mass increase for high loading conditions in Figure 2.25. For the highest mass loading in frames i) through l), almost the entire filter is covered in the crust explaining the extremely high measured pressure drop. Overall these images suggest to get mass loss from the filter (i.e. salt penetration through filter) as in the case of saturated wet loaded filters, the hygroscopic particle loading would have to be very high or the filtration velocity much greater than cases examined in this study. At a filtration velocity of 0.45m/s the salt pools up on top of the filter instead of penetrating deep into the medium.

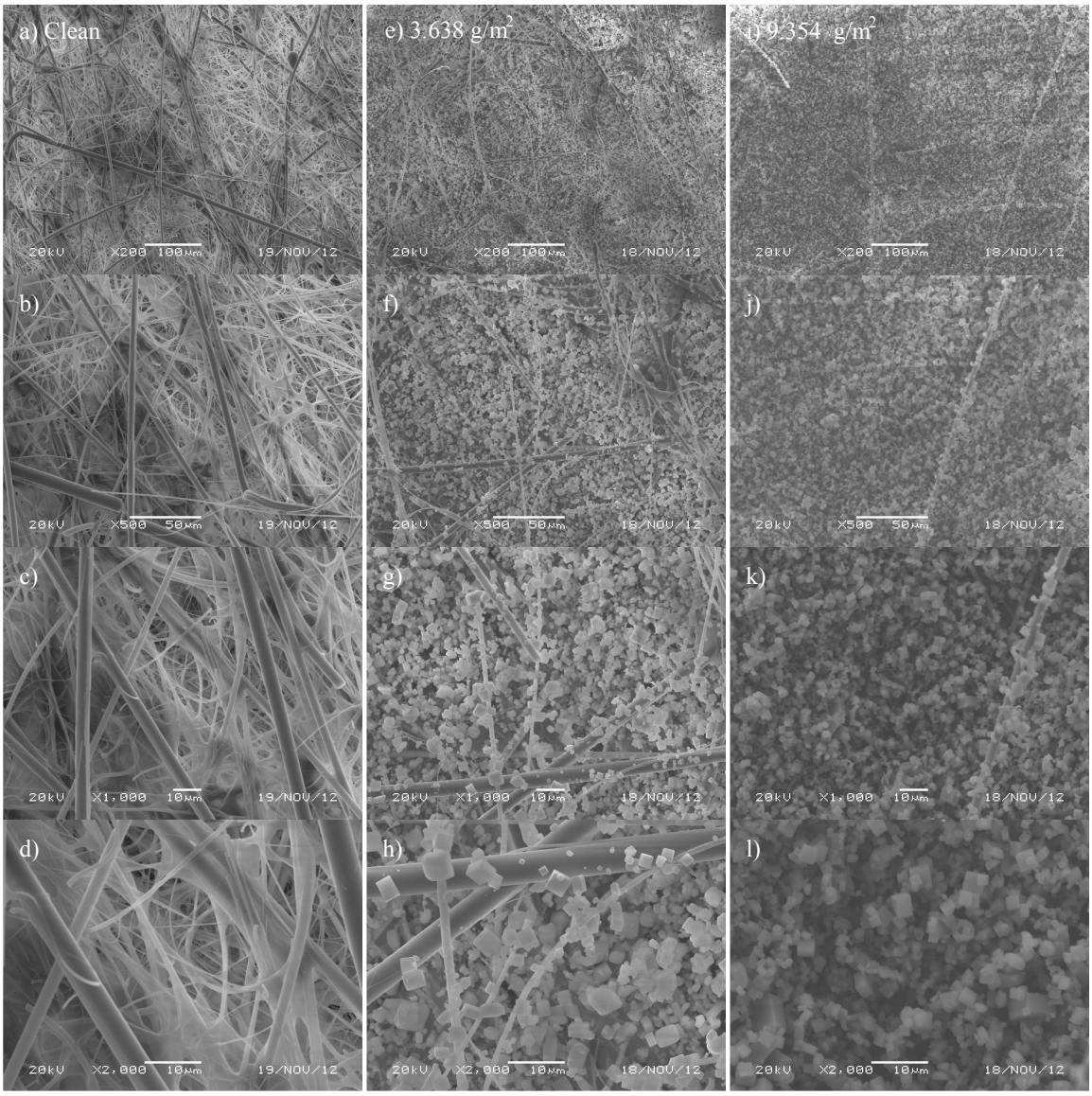

Figure 2.26: SEM images of HEPA filter after loading with NaCl particles at various mass loadings. Column (1) clean, column (2) 3.638g/m^2, column (3) 9.354 g/m^2 loading

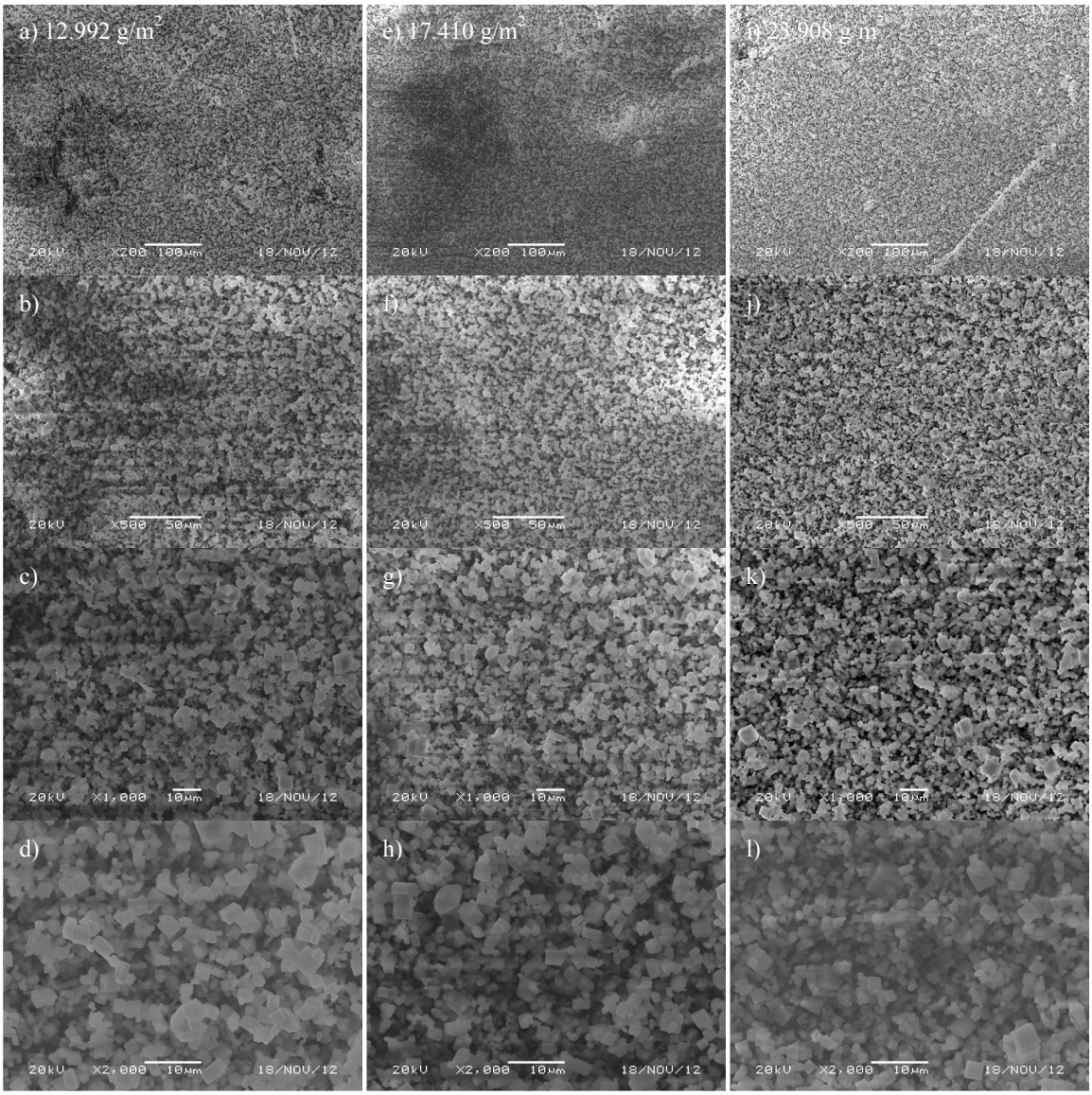

Figure 2.27: SEM images of HEPA filter after loading with NaCl particles at various mass loadings.Column (1) 12.992g/m^2, column (2) 17.410g/m^2, column (3) 23.908g/m^2 loading

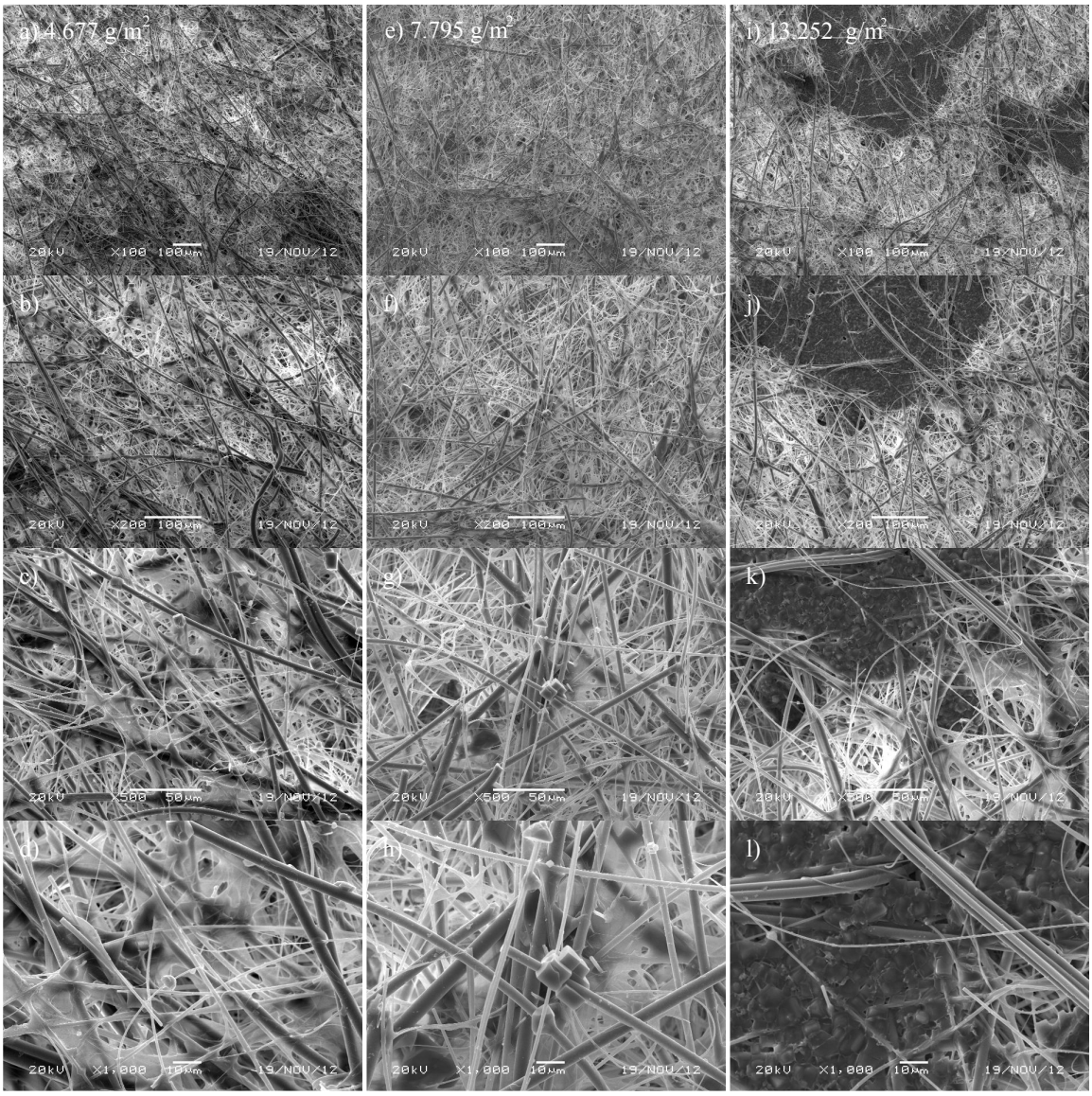

Figure 2.28: SEM images of HEPA filters loaded with NaCl particles after undergoing humidity fluctuations at various mass loadings.Column (1) 4.677g/m^2, column (2) 7.795g/m^2, column (3) 13.252g/m^2 loading

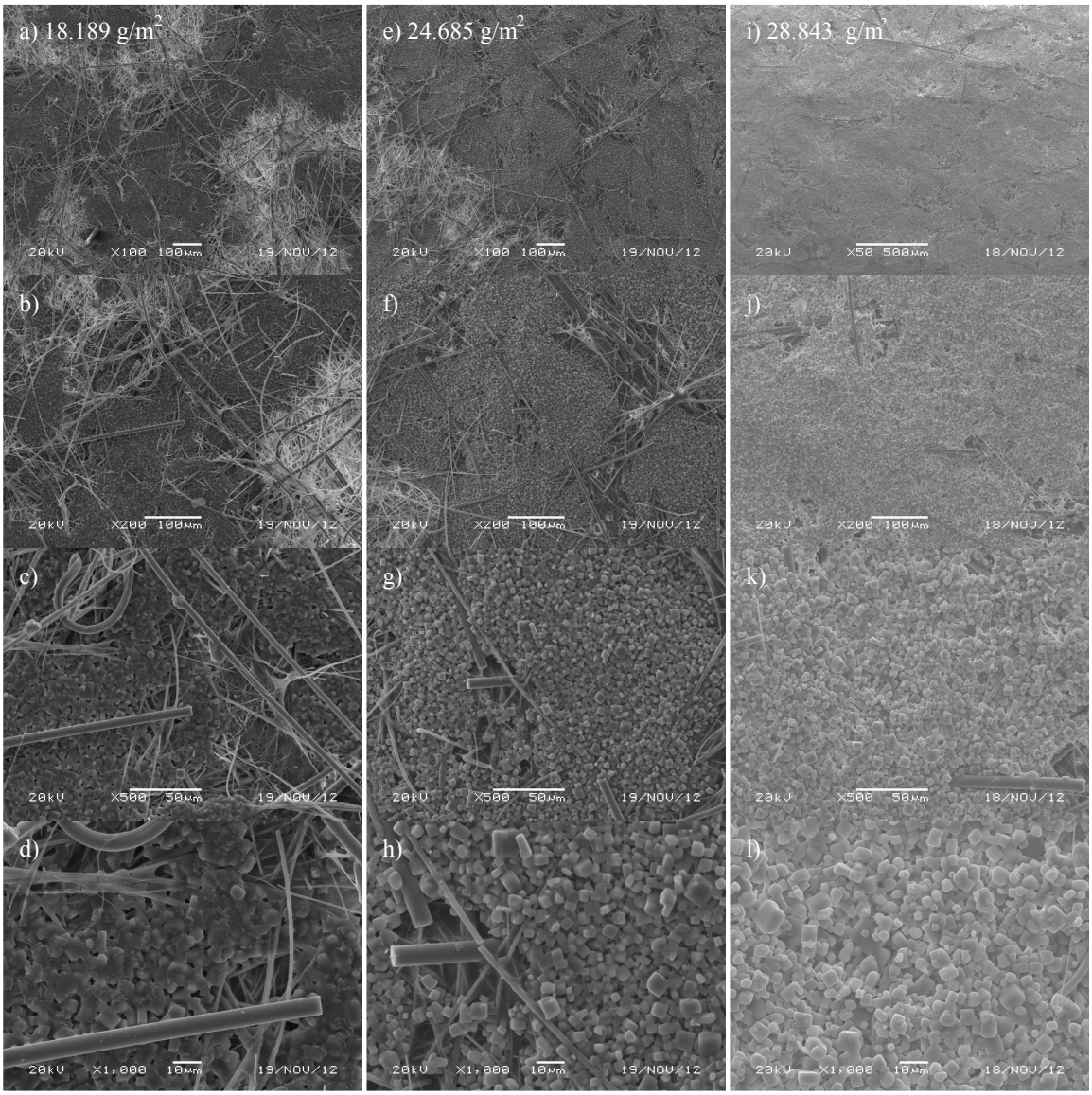

Figure 2.29: SEM images of HEPA filters loaded with NaCl particles after undergoing humidity fluctuations at various mass loadings. Column (1) 18.189g/m^2, column (2) 24.685g/m^2, column (3) 28.843g/m^2 loading

2.4 Filter ESEM Imaging

To visualize the redistribution of collected dry NaCl particles on filter fibers, a sample was observed with an Environmental SEM (ESEM). ESEM can be used to observe hydrated samples at low vacuum conditions and variable water vapor pressure. The process from deliquescence through efflorescence is shown in Figure 2.30. In the sequence of images, it is evident that upon deliquescing, the dendrites form droplets which can eventually coalesce with nearby droplets creating a film covering the filter surface. The ultimate effloresced state consists of concentrated larger deposits unlike the originally evenly distributed individual NaCl crystals.

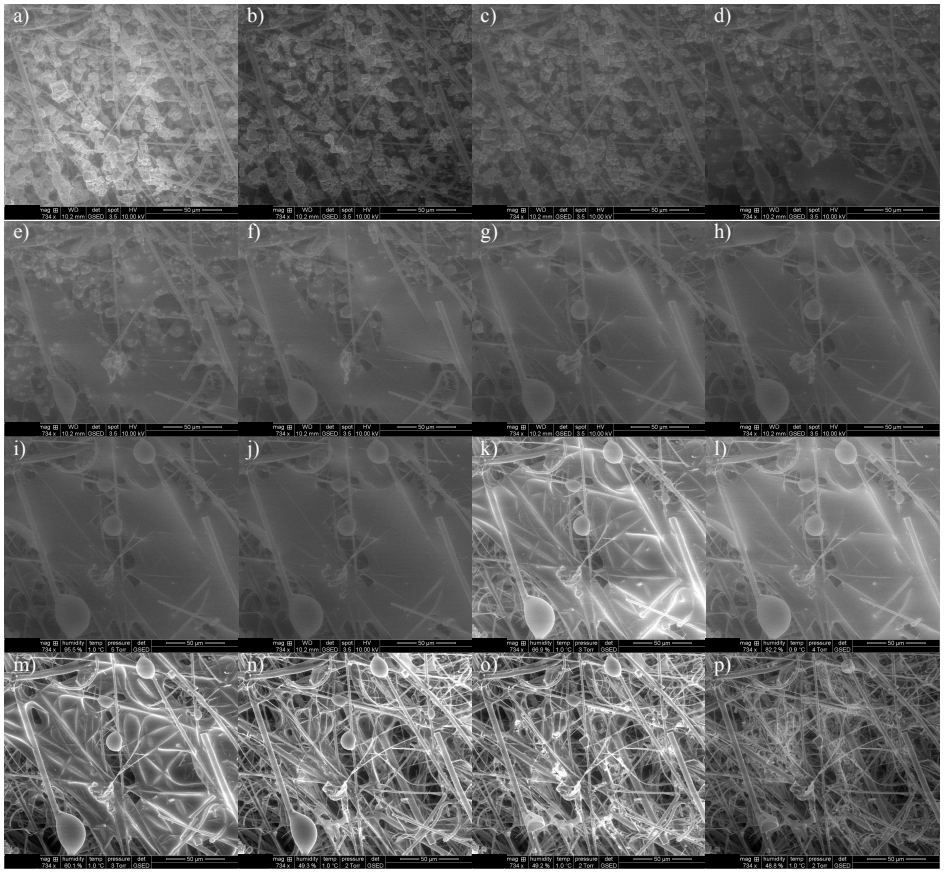

Figure 2.30: ESEM images of deliquescence/efflorescence cycle of NaCl particles captured on HEPA filter.

Figure 2.31 shows an already deliquesced and effloresced deposit undergoing another high and low humidity cycle. Based on the image the droplets do not effloresce to the same location as before, but spatially redistributes. Therefore upon successive deliquescence and efflorescence cycles hygroscopic particles may transport at least on the surface of the filter.

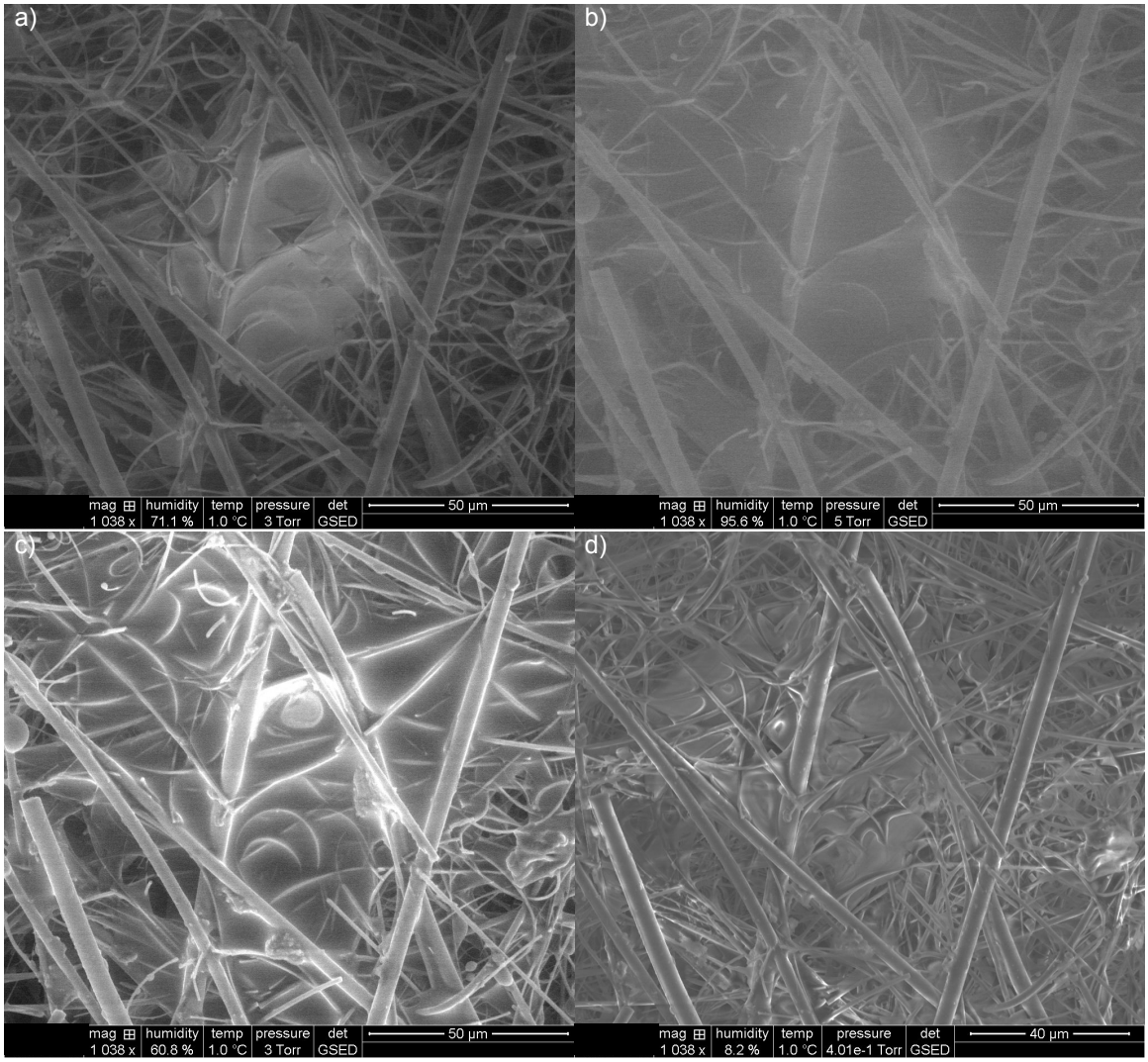

Figure 2.31: ESEM images of NaCl deliquescence in frames a) and b), efflorescence in c) and d), after being deliquesced/effloresced once on HEPA filter.

The results in Figures 2.30 and 2.31 were obtained with the Peltier stage set to 1°C. However, the actual temperature of the sample is questionable since there is a significant insulation created by the filter itself between the stage and the deposited particles. Therefore an ESEM is not appropriate to study the exact deliquescence point of hygroscopic particles unless the sample has been allowed to sit on the stage for an extensive period as otherwise the actual relative humidity of the particles is not known due to the possible temperature difference.

In addition to observing a filter with low mass loading, a sample from 28.843g/m^2 filter was also studied. The temperature and relative humidity conditions that the incomplete 28.843g/m^2 filter sample was exposed to are shown in Figure 2.32. The results are shown in Figure 2.33. Similar to the SEM images in Figure 2.29, the effloresced states in frames c) and e) maintain cubical structure. From the deliquesced images in frames b) and d), it is evident that each crystal begins to uptake water forming an extensive film that has a very low surface area to volume ratio. Therefore the original crystals do not fully deliquesce and retain their cubical shape through efflorescence. To conclude, while the exact relative humidity that the crystals are exposed to is unknown due to a temperature difference between the stage and the top of the filter, the images can be used to qualitatively describe deliquescence and efflorescence processes under humidity fluctuations.

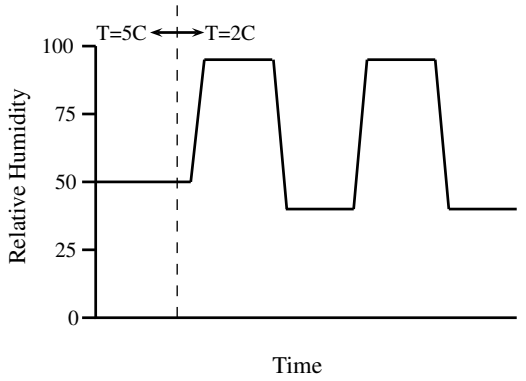

Figure 2.32: Air conditions the filter sample in Figure 2.33 was exposed to.

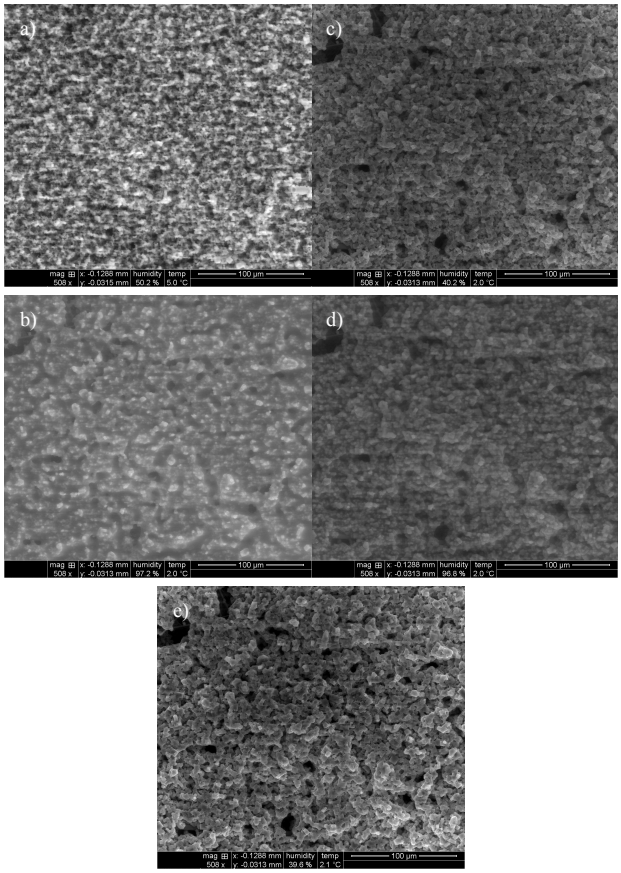

Figure 2.33: ESEM images of 28.843g/m^2 NaCl loaded HEPA filter in frame a) through deliquescence in frames b) and d), efflorescence in c) and e).

2.5 NH_4Cl In Humid Flow

Since the interaction between NH_4Cl particles and cobalt coated wafers were noted to depend on the humidity of the environment even below the deliquescence point, a HEPA filter was loaded with NH_4Cl particles and exposed to humid air flow. Figure 2.34 shows a cake build up immediately after atomization below the deliquescence point at various magnification levels. The cake appers to be built of clearly defined crystals.

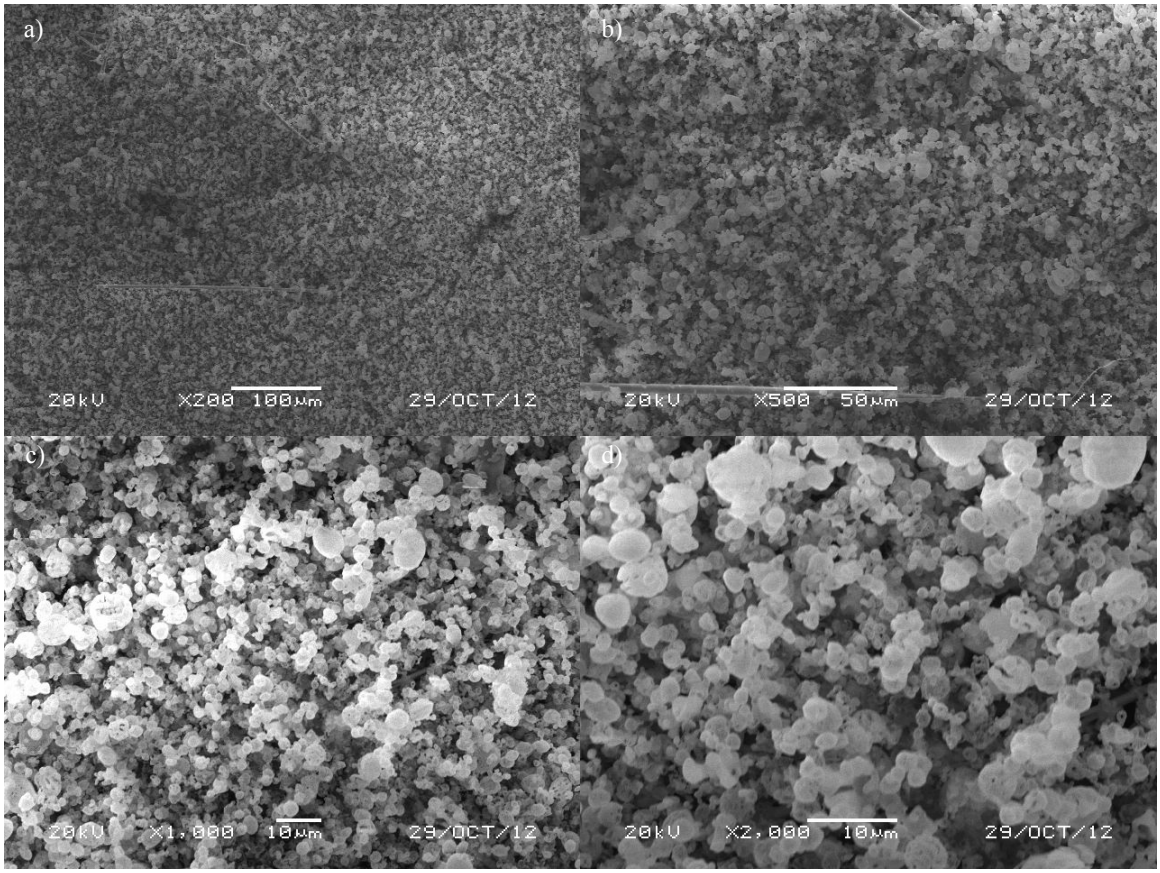

Figure 2.34: NH_4Cl particles deposited on HEPA filter.

Figures 2.35 and 2.36 show a NH_4Cl loaded filter after 60 minute exposure to 70% and 75% relative humidity air flows respectively. In both instances the crystals

appear to agglomerate with the individual crystals meddling together. Although the physical appearance of the cake was noted to transform, no mass increase beyond instrument uncertainty was recorded between the state in Figure 2.34 and after exposure to humid air flow in Figures 2.35 and 2.36. However, the images indicate that even below the deliquescence point the air relative humidity can affect the cake formation as discovered by previous work [9].

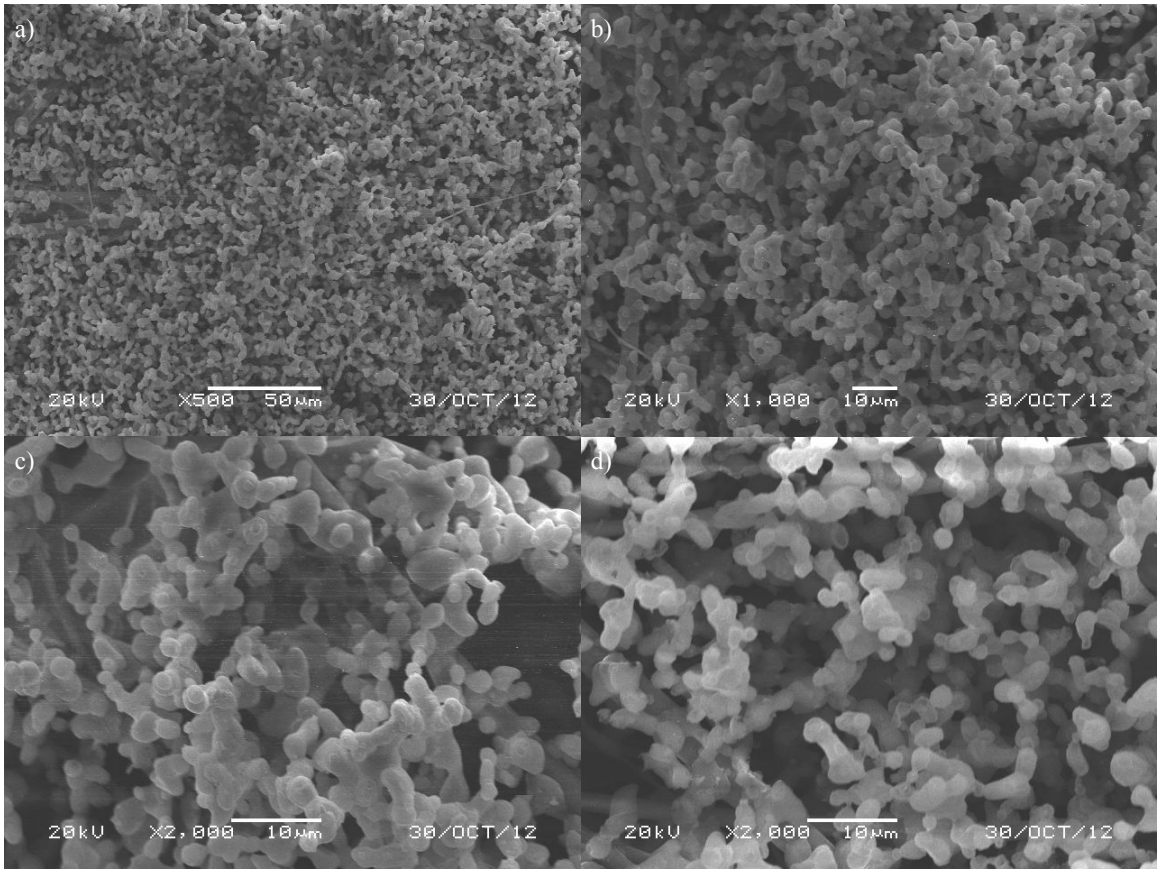

Figure 2.35: NH_4Cl particles deposited on HEPA filter after exposure to 70% relative humidity for 60 minutes.

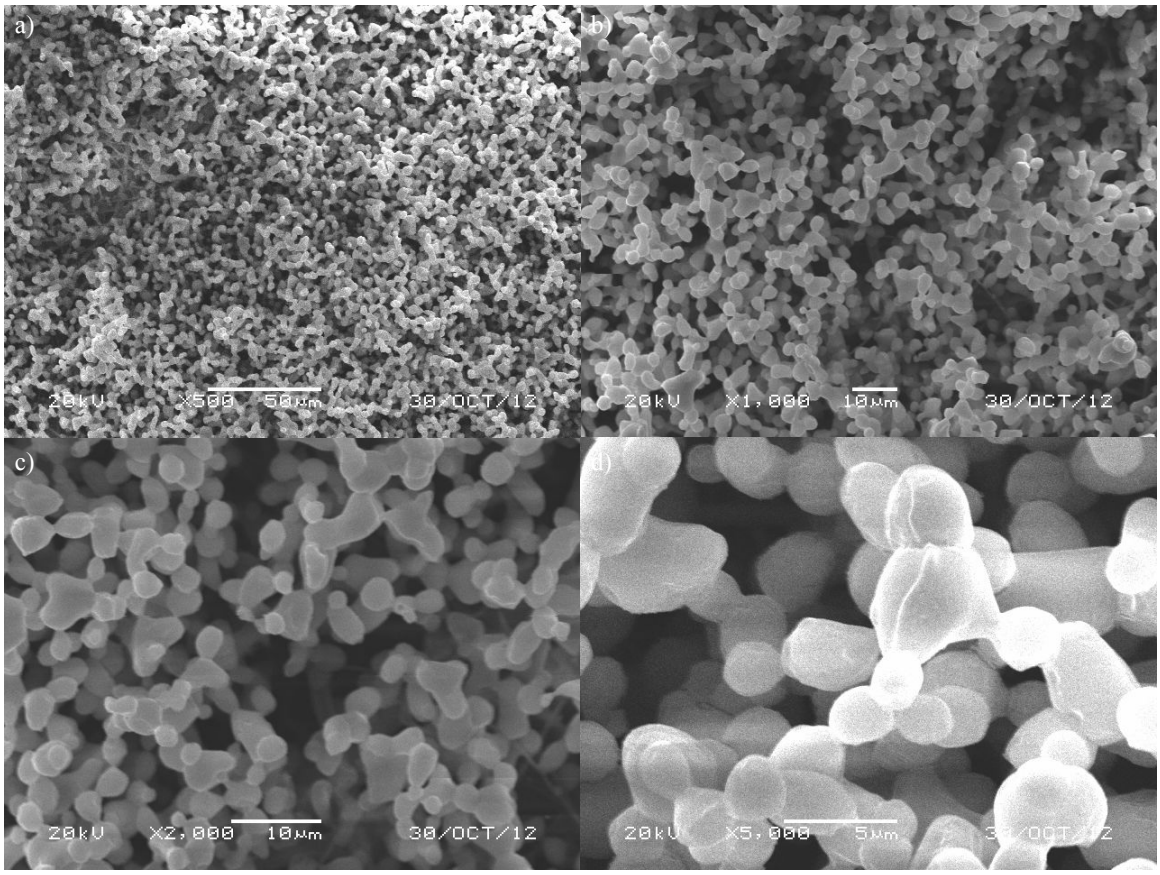

Figure 2.36: NH_4Cl particles deposited on HEPA filter after exposure to 75% relative humidity for 60 minutes.

2.6 Filtration Conclusions

In a semiconductor manufacturing facility, the high mass loadings explored in this chapter will not be encountered. Based on cited work on wet filtration and the hygroscopic particle data presented here it can be concluded that hygroscopic contaminants would not be re-entrained into an airstream for the conditions of this study until extremely high mass loadings are used. Even at almost $25 g/m^2$ no mass loss was recorded, but the deliquesced liquid appeared to redistribute itself within the filter after forming a film on top of the filter. Filter materials other than borosilicate

glass should be investigated. For example, it is possible that the solution would be transported through a more hydrophobic filter material. Even though no mass loss was recorded, a deliquesced hygroscopic contaminant could lead to other contamination pathways as it can redistribute within the filter through capillary action. In one possibility, a deliquesced hygroscopic contaminant could interact with another deposit causing a chemical reaction. Additionally, no water uptake was observed below the deliquescence for NH_4Cl particles even though the cake resistance decreased and the crystals appeared to agglomerate. The agglomeration of the individual NH_4Cl crystals below the deliquescence point indicates some interaction between the crystals and water vapor. Therefore, the effects of humidity on NH_4Cl particles should be studied further, especially in a situation in which they are found near wafer surfaces.

Chapter 3

Hygroscopic Contaminants on Wafers

3.1 Previous Work on Inorganic Wafer Contaminants

Extensive research has been conducted on particle contaminants on wafers and possible sources of such contaminants. However, many sources for potential contaminants still exist [32]. Both gas and solid phase contaminants are shown to exist within a fab. Many of the particulate contaminants are composed of NH_4^+, Na^+, Cl^-, and SO_4^{2-} indicating the existence of hygroscopic particle contaminants in a fab [33]. Bai et al. studied particle contaminants on wafer surfaces with SEM and EDS tools after exposing the wafers to open air in a class 1 fab for various lengths of time. Along with organic contaminants, many inorganic contaminants were also present containing chlorine and potassium ranging from 1x2μm to 20x20μm in size. One signature of typical inorganic contaminant, described by the authors as fractal geometry, is shown in Figure 3.1 [12].

Wafer exposure to chlorine ions can be especially detrimental due to chlorine's corrosive nature [34–37]. Fan et al. experimentally tested the corrosion of an Al-Cu layer in three different conditions, (1) at 1000ppm NH_4Cl solution, (2) 100% relative humidity, and (3) a dip in NH_4Cl solution followed by blow dry with nitrogen and storage in 100% relative humidity. Each test was conducted at 25°C. The results showed that a dip followed by a blow drying left a "corrosion product," while storage in a solution did not. They interpreted this to indicate that the corrosion product was soluble in water [38]. The corrosion of copper when exposed to NaCl particles is also

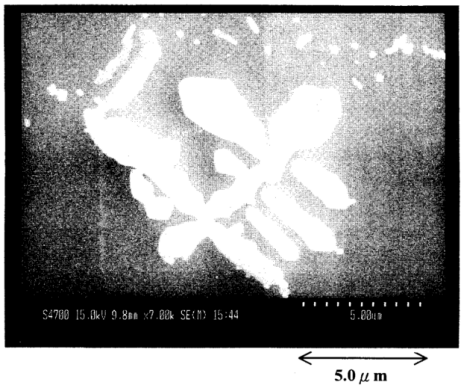

Figure 3.1: SEM image of a typical inorganic contaminant, taken from [12]

known to increase at high relative humidities [39]. Some of these surface effects may be associated with water being adsorbed onto wafer surfaces. Borophosphosilicate glass films (BPSG) were shown to adsord water over time in storage due to hygroscopic properties [40, 41].

Both optical and electron microscope techniques can be utilized to observe deliquescence and efflorecence of surface deposited aerosols. The deliquescence and efflorescence properties of a number of aerosols (NaCl, $(NH_4)_2SO_4$, Na_2SO_4, and NH_4NO_3) have been accurately studied using an ESEM [42, 43]. In addition to scanning electron microscopy (SEM), transmission electron microscopy (TEM) and mircoscopic Fourier transform infrared (micro-FT-IR) techniques have been used to characterize hygroscopic aerosols [44, 45].

However, microscopy techniques cannot be used to study the true growth processes of aerosols. Since the aerosol must be deposited on a surface, it will form a contact angle with the surface which depends on the solution as well as the surface altering its behavior from that of an aerosol suspended in air. Similarly, true efflorescence relative humidity of an aerosol cannot be studied with microscopy techniques, again, due to surface interactions between the substrate and aerosol.

Although bulk theory predicts a prompt deliquescence relative humidity for hygroscopic salt aerosols, experimental research indicates possible surface water interaction prior to deliquescence point. The collection of surface water prior to deliquescence may depend on the composition of the aerosol and its size [46–48].

For a semiconductor manufacturing purposes, aerosols are most problematic if they are deposited onto wafer surfaces. Therefore ESEM techniques are appropriate for studying effects of hygroscopic contaminants on wafer surfaces. Additionally, the effect of relative humidity on the hygroscopic particle prior to deliquescence point is extremely important as cleanrooms typically operate at a relaitve humidity of 45%. In this chapter, the effects of relative humidity on NH_4Cl particles deposited on a cobalt witness wafer are studied with both optical microscopy and ESEM techniques.

NH_4Cl particles of size range 100-200μm and 500nm-10μm were observed with an ESEM (Quanta 650 FEG, FEI, Inc.). To reach relative humidities up to and above the deliquescence point of NH_4Cl, the temperature had to be kept at 5°C to support high enough vapor pressure without damaging the detector.

3.2 Optical Microscopy Results

To test the effect of humidity on NH_4Cl particles, wafer pieces were placed into a controlled relative humidity environments. Tests were conducted at relative humidities ranging from 20% to 77.3%, which is the deliquescence point of NH_4Cl at 25°C. The test pieces were scored from a silicon witness wafer with a cobalt layer protected by TiN layer. The NH_4Cl particles were atomized from a 50% solubility by mass aqueous NH_4Cl solution. For a first round of experiments, the NH_4Cl solution was atomized at ambient relative humidity close to 50%. The contaminated wafer pieces were then placed into a chamber for 72 hours with saturated NaBr solution

which provided a relative humidity of 61%. The results from the initial tests are shown in Figure 3.2 where frames a) and b) show the wafer pieces immediately after atomization and c) and d) after 72 hours of humidity exposure. From frames a) and b), it is not clear whether the NH_4Cl particles were completely dry upon atomization. Based on the discoloration in frames c) and d), it is evident that the particles either deliquesced or there was a substantial amount of water absorbed on the particles enabling the corrosion of the wafer.

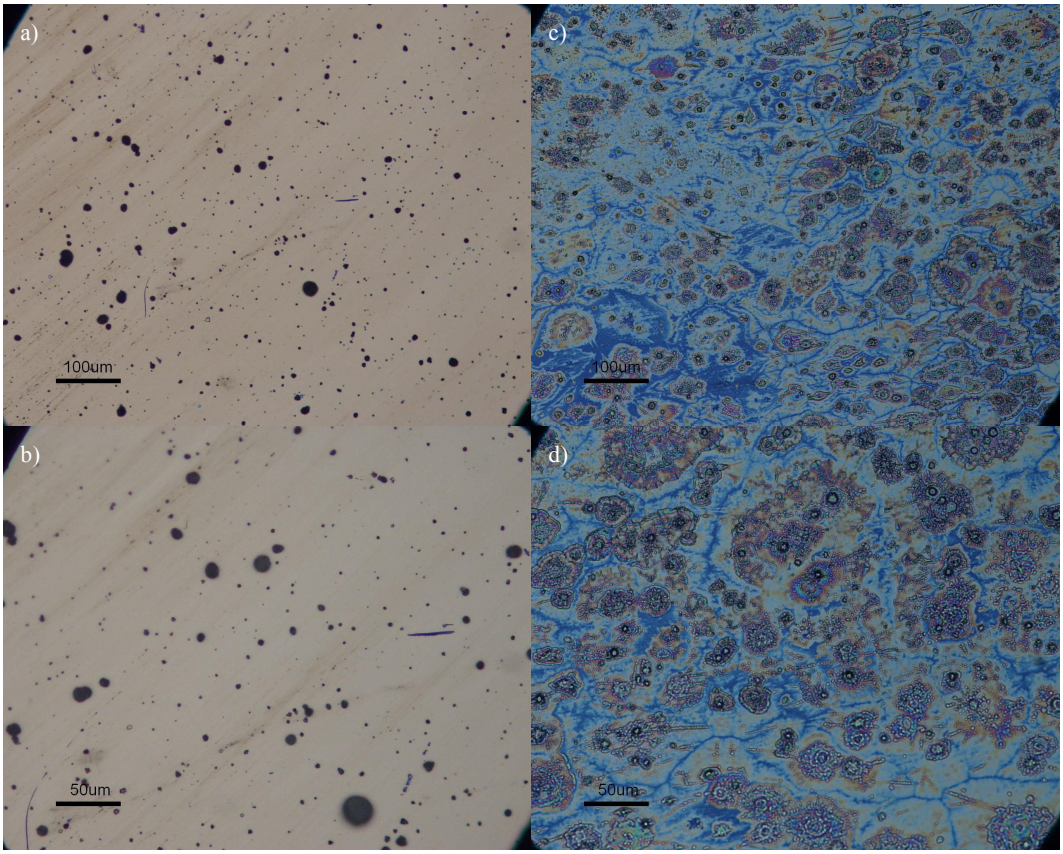

Figure 3.2: Optical images of NH_4Cl particles on witness wafer. Images a) and b) are after atomization while c) and d) are after exposure to 60% relative humidity air for 72 hours. Particles were atomized at 50% relative humidity.

To assess the effect of humidity on dry particles, another set of tests was con-

ducted in a more tightly controlled environment. The atomization relative humidity was kept below 20% relative humidity and the particles were allowed ample flight time to ensure they were dry upon depositing on the wafer pieces. After placing the samples into the humidity chamber, the chamber was purged with HEPA filtered air with 15% relative humidity. The wafer pieces were imaged after atomization and also after removing them from the humidity chamber. Figure 3.3 shows a wafer piece after atomization in frames a) and b), while frames c) and d) correspond to images after 72 hours of exposure to 19.9% mean relative air humidity at a mean temperature of 22.8°C. The humidity was achieved by placing a saturated solution of LiCl in the chamber. The relative humidity was expected to be lower based on saturated salt tables. However, the humidity higher because either water vapor diffused into the chamber from the surroundings or the LiCl solution had been held at a low temperature before being placed into the chamber, permanently altering its saturation humidity. The images do not correspond to the same location, but show a typical spot. From the images it is evident that the NH_4Cl particles did not corrode the wafer beyond their initial deposition position.

Next, humidity effects were studied at relative humidities at the level of a typical fab. Figure 3.4 shows a wafer piece immediately following atomization in frames a) and b). Frames c) and d) show the same wafer piece after 72 hour exposure to fluctuating relative humidity between 45% and 58% with a mean of 54.8%. The humidity was achieved by atomizing mist into the chamber which was allowed to evaporate after the purge process. After sealing the chamber, the relative humidity fluctuated due to diffusion of water vapour into the chamber from the surroundings. The mean temperature was 22.6°C. Again, the frames do not show the same location, but instead provide a typical view. Comparing the images, after 72 hours the NH_4Cl particles have corroded the wafer beyond the original deposition area. However,

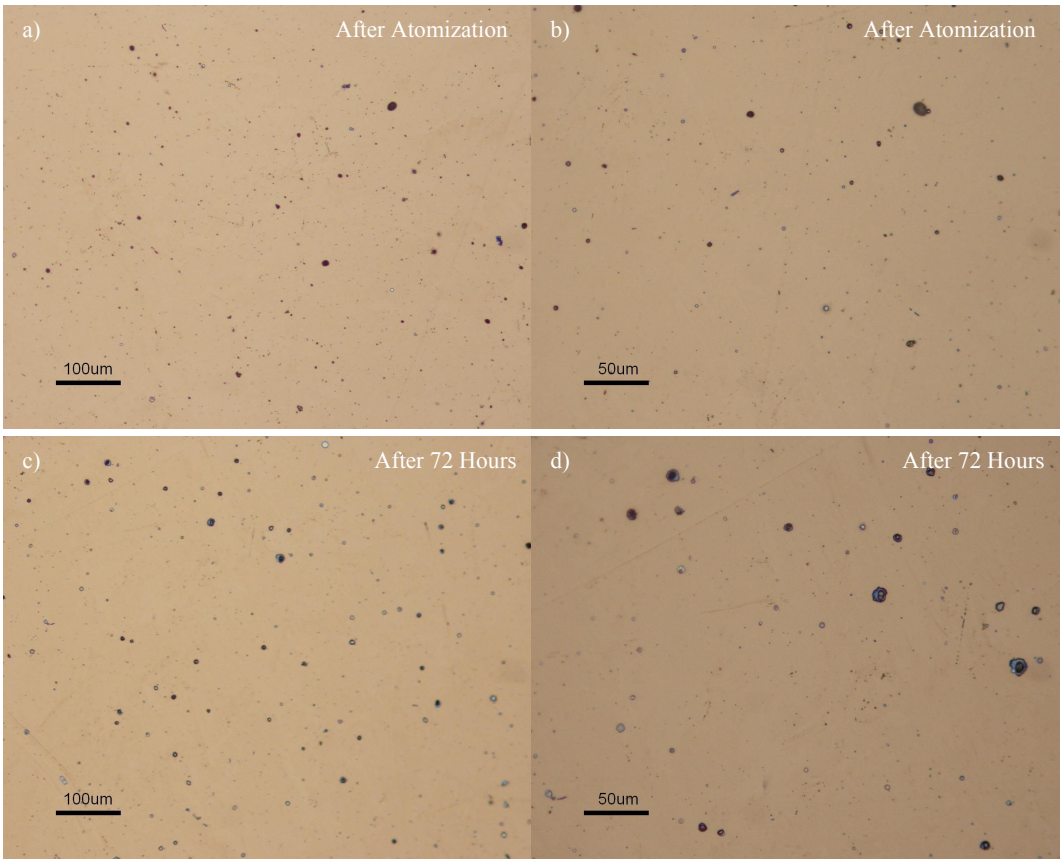

Figure 3.3: Optical images of NH_4Cl particles on witness wafer. Images a) and b) are after atomization while c) and d) are after exposure to 19.9% relative humidity air for 72 hours at 22.8°C.

the solid black particles indicate that deliquescence did not take place. Comparing Figures 3.3 and 3.4 indicates that prior the to point of deliquescence, the air humidity plays a factor on the corrosiveness of NH_4Cl particles.

Figure 3.5 shows a cobalt coated wafer after exposure to 60.8% mean relative humidity air at 21.5°C for 72 hours. The humidity was achieved by placing a saturated solution of NaBr in the chamber. This time the wafer corrosion is significantly different from that seen in Figure 3.2. Similar to Figure 3.4 the deposited crystals do not appear to have deliquesced, but the areas around the particles are corroded

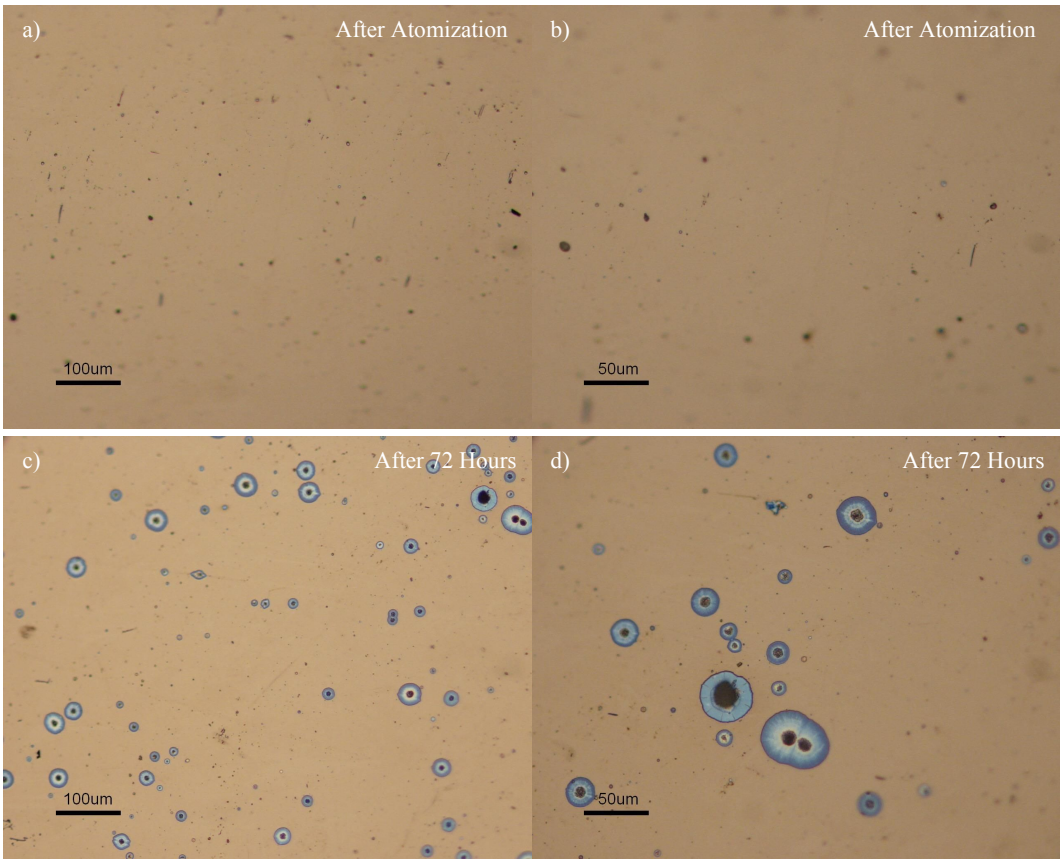

Figure 3.4: Optical images of NH_4Cl particles on witness wafer. Images a) and b) are after atomization while c) and d) are after exposure to fluctuaing relative humidity around a mean of 54.8% for 72 hours at 22.5°C.

as indicated by the discoloration. Therefore it can be concluded that the particles in Figure 3.2 were not completely effloresced upon deposition, but would represent a case where perhaps a supersaturated NH_4Cl aerosol were to deposit onto a wafer. The results in Figure 3.4 represent a case where NH_4Cl particles might have been generated from a gas to particle reaction and then deposited onto a wafer.

Finally, scored wafer pieces with NH_4Cl deposited were exposed to relative humidities up to the deliquescence point. Figure 3.6 shows a wafer piece before atomization in frames a) and b) and after exposure to 74.8% mean relative humidity for

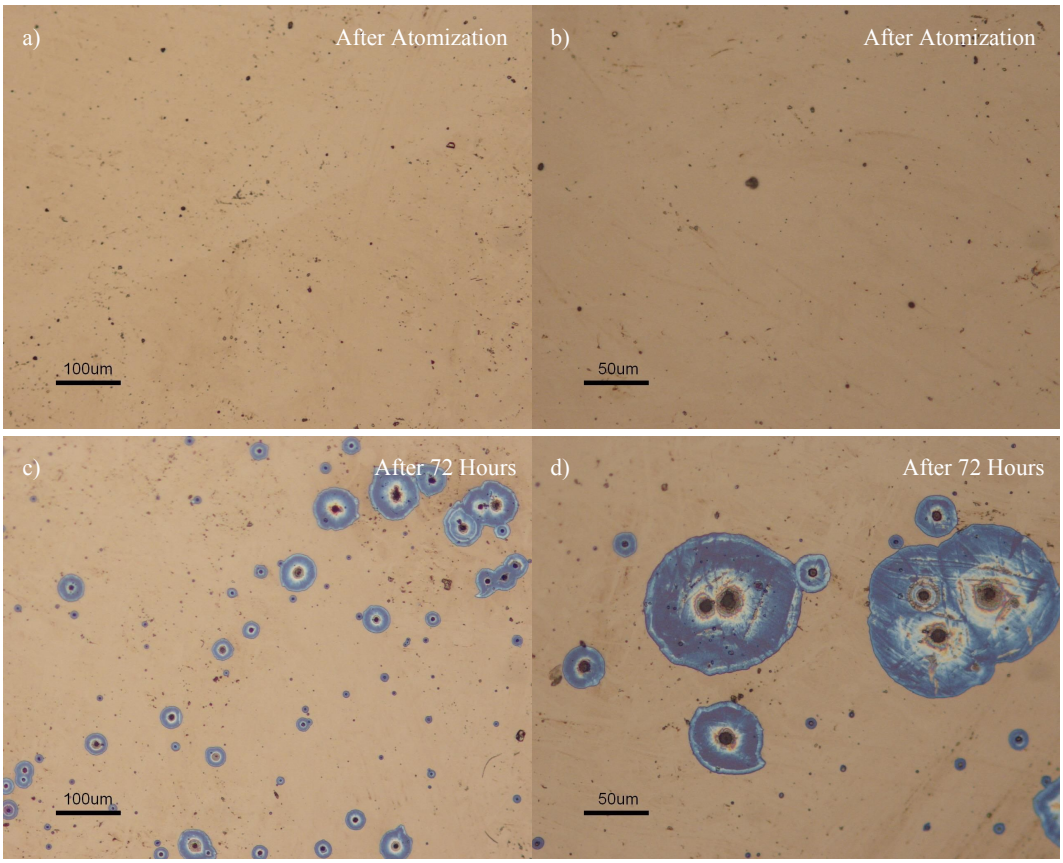

Figure 3.5: Optical images of NH_4Cl particles on witness wafer. Images a) and b) are after atomization while c) and d) are after exposure to 60.8% relative humidity air for 72 hours at 21.5°C.

72 hours in frames c) and d). The temperature was 22.1°C throughout the exposure. The relative humidity was reached by placing saturated NaCl solution into the chamber. Interestingly, no solid particle artifacts are found in the images like in Figures 3.3 through 3.5. In fact, the NH_4Cl particles appear to have completely deliquesced. From the images it is difficult to determine the original particle size since no solid artifacts are present. However, since all of the particle entered into solution, it can be concluded that the foot prints in frames c) and d) are larger than those for the same particle size in Figures 3.4 and 3.5.

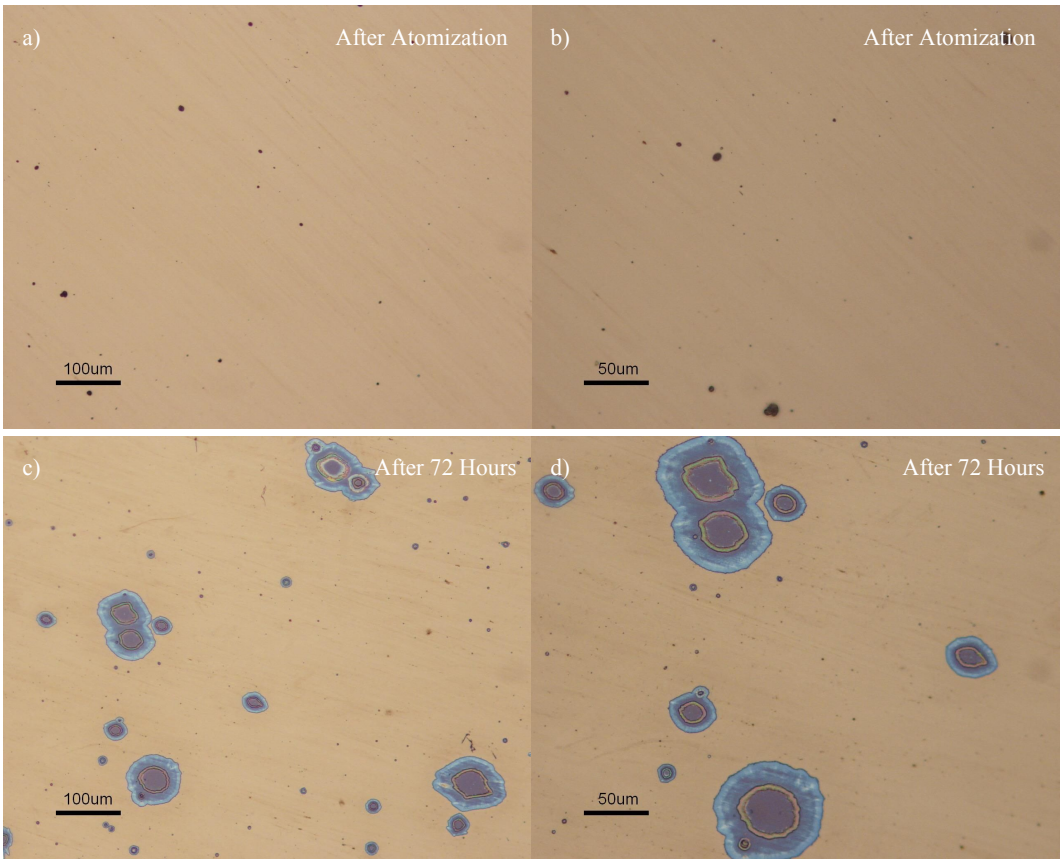

Figure 3.6: Optical images of NH_4Cl particles on witness wafer. Images a) and b) are after atomization while c) and d) are after exposure to 74.8% relative humidity air for 72 hours at 22.1°C.

Figure 3.7 shows wafer pieces exposed to a mean relative humidity of 77.7% at 22.1°C for 72 hours created by a saturated NH_4Cl solution. The foot prints of the deliquesced particles appear similar to those in Figure 3.6. Since the saturated NH_4Cl solution created an environment with enough water vapor pressure to deliquesce the particles, it can be concluded from the visual similarity that the particles in Figure 3.6 entered solution below the deliquescence point of NH_4Cl. A possible explanation for the particles deliquescing below the expected point is that an exothermic chemical reaction occurs between the wafer and the particles, lowering the local temperature

and creating points of relative humidity above the deliquescence point. Another possibility is that the surface energy of the coupled salt, water, air, and substarte system favors deliquescence at lower relative humidity values.

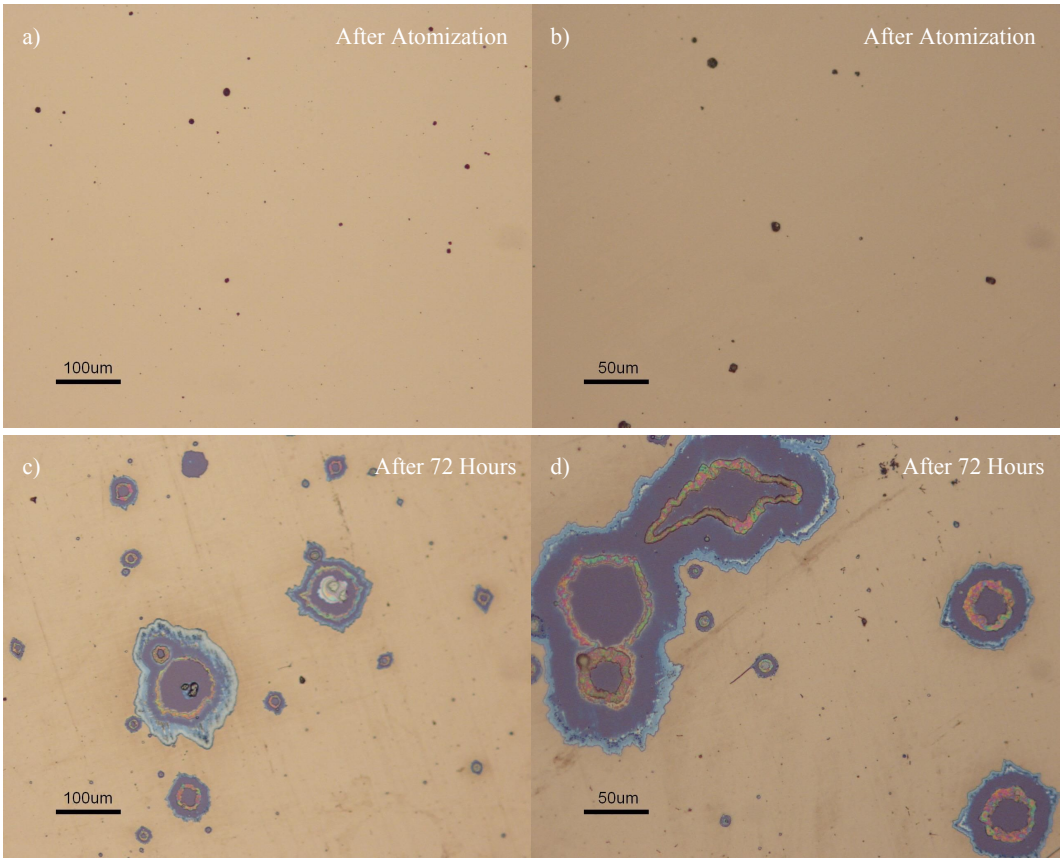

Figure 3.7: Optical images of NH_4Cl particles on witness wafer. Images a) and b) are after atomization while c) and d) are after exposure to 77.7% RH air for 72 hours at 22.1°C.

For all the exposure experiments, the temperatures and relative humidities are plotted against time in Figure 3.8.

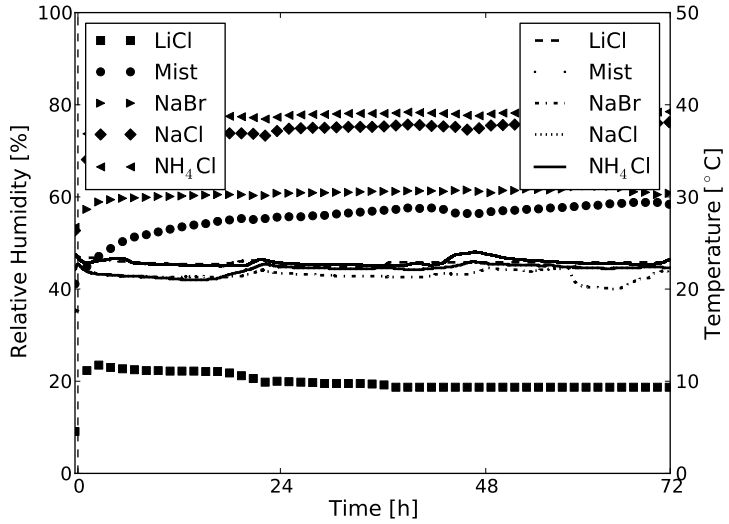

Figure 3.8: Measured temperatures and relative humidieties as a function of time for all the wafer exposure experiments.

3.3 ESEM Results

In addition to long air humidity exposures, an ESEM was used to gain further insight on effects of deliquesced NH_4Cl particles on a wafer. However, unlike the long term humidity exposure experiments, the ESEM experiments were limited to 5°C. The reason for the low temperature limit was to provide a high enough relative humidity to deliquesce the NH_4Cl particles. At a higher temperature, a sufficiently high water vapor pressure could not be provided without damaging the ESEM detector. Although, the relative humidity for deliquescing is higher at lower temperatures, a corresponding deliquescence humidity can be predicted based on theory as discussed in Chapter 1.

Figure 3.9 shows a single NH_4Cl particle going through deliquescence and efflorescence. Initially the water vapor in the chamber was increased at 10°C to reach

a relative humidity of 59.8%. From frame d) to e) the temperature was reduced to 5°C to allow for a lower vapor pressure to provide a higher relative humidity. However, upon reducing the temperature of the Peltier stage, the NH_4Cl particle deliquesced slightly as the vapor pressure was not adjusted quickly enough from its value to provide 59.8% at 5°C. After reducing the vapor pressure to provide 59.8% relative humidity the particle was imaged again as seen in frame e). Although the environment dropped to relative humidity level below the deliquescence point some, surface water was still maintained. At a temperature of 5°C, the vapor pressure was increased to initiate deliquescence, and then it was lowered again to see if the surface water would be expelled, to better determine the deliquescence point of NH_4Cl as shown in frames g) through j). Finally in frame k) the particle was allowed to fully deliquesce and then effloresced in frame l). As expected, upon deliquescing the surface coverage by a single crystal is greatly increased from the dry state. In Figure 3.9 the particle diameter increases from 93μm to 315μm, a 239% increase in diameter and 1047% increase in area. Also, based on frame l) the effloresced particle surface coverage is also greater than the original crystal. However, upon inspecting another area on the same copper tape sample, a different effloresced particle was found as shown in 3.10. Since the particle in Figure 3.9 was imaged continuously, the electron beam could have affected the efflorescing process. The temperatures and relative humidities corresponding to Figure 3.9 are summarized in Table 3.3.

Table 3.1: Temperatures and relative humidities for Figure 3.9

Frame	**Temperature [°C]**	**Relative Humidity [%]**
a	10	20.2
b	10	40.2
c	10	49.9
d	10	59.8
e	5	59.3
f	5	70.0
g	5	79.4
h	5	80.3
i	5	78.9
j	5	79.1
k	5	89.7
l	5	20.2

To determine the predicted state of effloresced NH_4Cl particles on copper, a number of particles were imaged before deliquescence and after efflorescence. The images are shown in Figures 3.11 and 3.12. All the effloresced states are similar to the one in Figure 3.10 except frame p) in Figure 3.12, which appears similar to frame l) in Figure 3.9. Since the particle in frame p) of Figure 3.12 was imaged continuously through efflorescence, it can be concluded that the electron beam affects the efflorescence process. Therefore NH_4Cl particles should not be continuously imaged through efflorescence with an ESEM, at least at high beam energies.

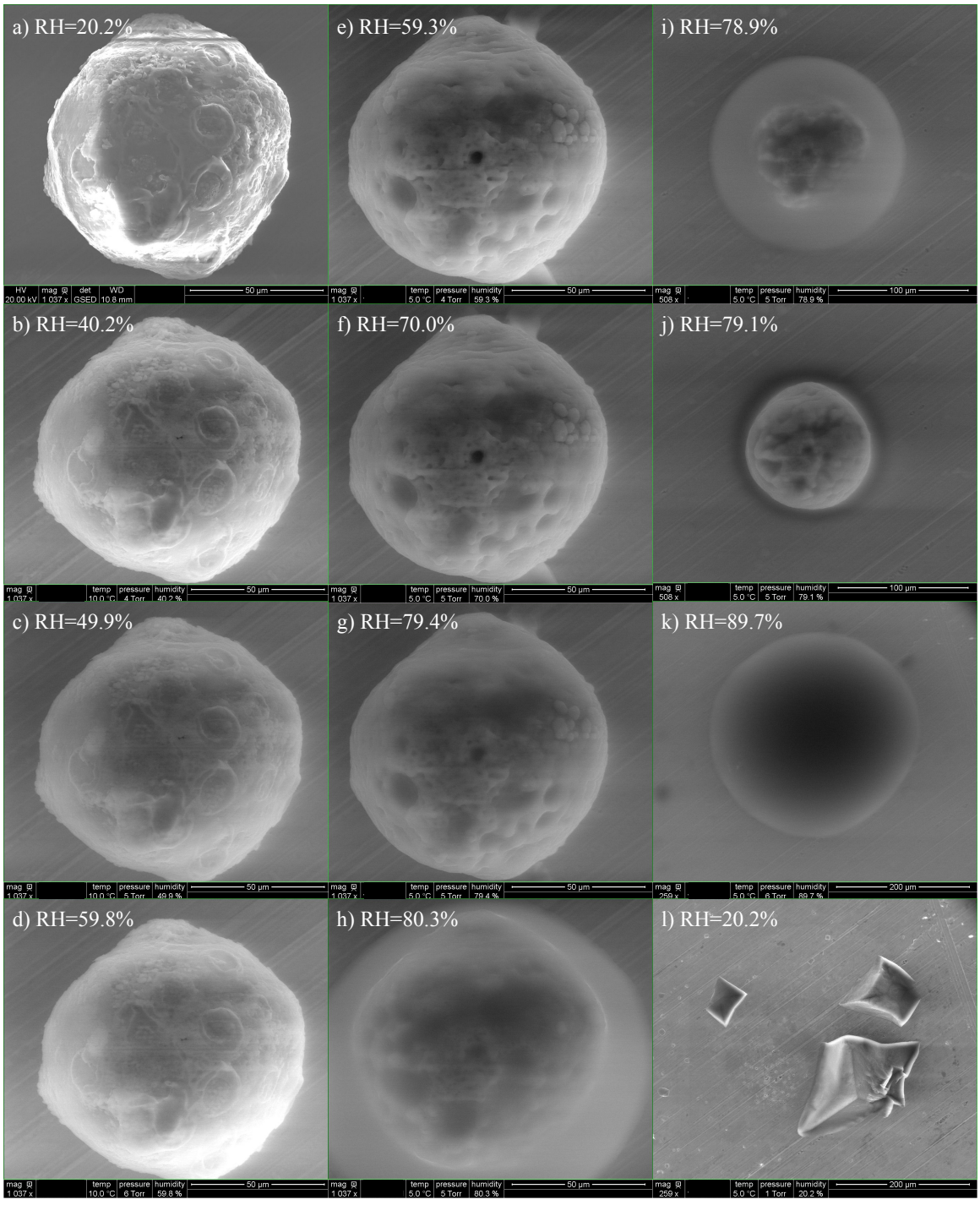

Figure 3.9: ESEM images of large NH_4Cl particles on copper tape through deliquescence and efflorescence.

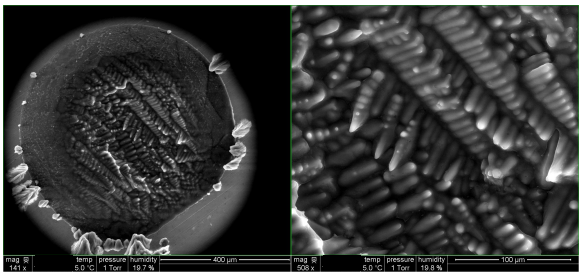

Figure 3.10: ESEM images of an effloresced NH_4Cl particle on copper tape.

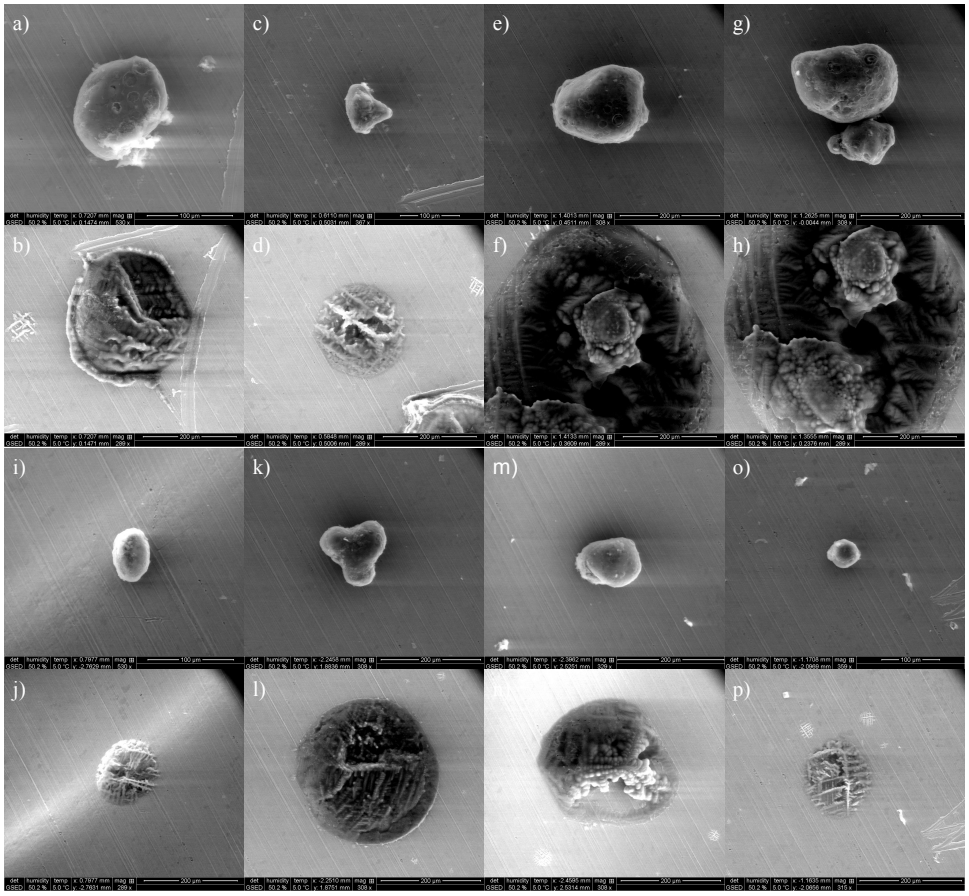

Figure 3.11: ESEM images of NH_4Cl particles and their corresponding effloresced images on copper tape.

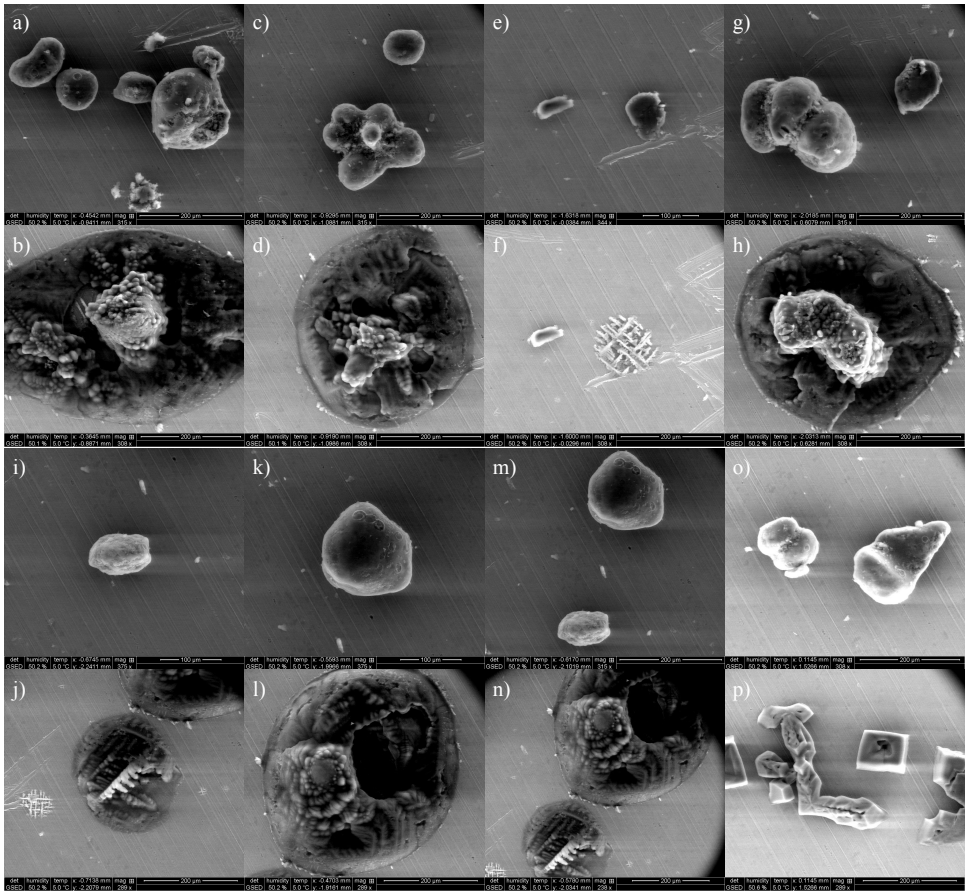

Figure 3.12: ESEM images of NH_4Cl particles and their corresponding effloresced images on copper tape. Frame m) shows a combination of frames i) and k) at a lower magnification while n) shows j) and l).

To quantify the growth of deposited NH_4Cl particles, a first order approximation was made to model the area of the particle and its effloresced state as a circle. The area was calculated as the minimum diameter required to encompass either the particle or effloresced foot print. Particles whose effloresced state was too large to be shown in one image were excluded from the calculations. The circles used for the diameter and area calculations are shown in Figures B.1 and B.2. Meanwhile, the change in area is defined as

$$\Delta A = 100\frac{A_f - A_o}{A_o} \tag{3.1}$$

where A_o is the original dry particle area and A_f is the final foot print area approximated as a circle. For frames c) and g) in Figure 3.12 where particles coalesced upon deliquescing, the dry particle area was approximated as a summation of the individual dry particles

$$\Delta A = 100\frac{A_f - \sum A_{o,i}}{\sum A_{o,i}} \tag{3.2}$$

The results are summarized in Table 3.3 which includes both Figures 3.11 and 3.12. In the tables, d_P is the original dry particle diameter and d_E is the effloresced state diameter. In all the cases, the effloresced foot print was greater than the original dry particle diameter. The circles used to calculate the area changes are included in Appendix B.

Table 3.2: Growth of NH_4Cl foot print on copper.

Figure	$\mathbf{d}_P$ [μ**m**]	$\mathbf{d}_E$ [μ**m**]	Δ**A** [%]
3.11a,b	132	310	449%
3.11c,d	97	200	327%
3.11i,j	70	152	367%
3.11k,l	161	293	233%
3.11m,n	135	294	379%
3.11o,p	63	155	501%
3.12c,d	210, 92	412	221%
3.12e,f	88	130	117%
3.12g,h	249, 126	436	144%
3.12i,j	108	252	442%

In addition to visual observations, Energy Dispersive X-ray Spectroscopy (EDX) line scans of particles on copper before deliquescence and after efflorescence were also

gathered. The EDX data for copper deposited particles are shown in 3.13 where frames a) and b) refer to the same location before deliquescence and after efflorescence respectively. Similarly, frames c) and d) also correspond to the same location. Based on the spatial extent of the spectogram, the chlorine footprint of the particle is larger following efflorescence than in the dry state. The absence of other constituents indicated that the effloresced artifact is mainly composed of chlorine. The existence of copper in the line scans in frames b) and c) indicates that the beam energy was too high to accurately characterize the surface. However, the higher count of copper at the location of the dry particle from frame a) to b) indicates that the effloresced state is lower in height than the original particle as the beam has penetrated deeper into the copper substrate. Therefore, future studies should be conducted with lower beam energy. However, the data illustrates that the EDX can be used to determine the size change in the deposit following deliquescence and efflorescence if visual cannot be used.

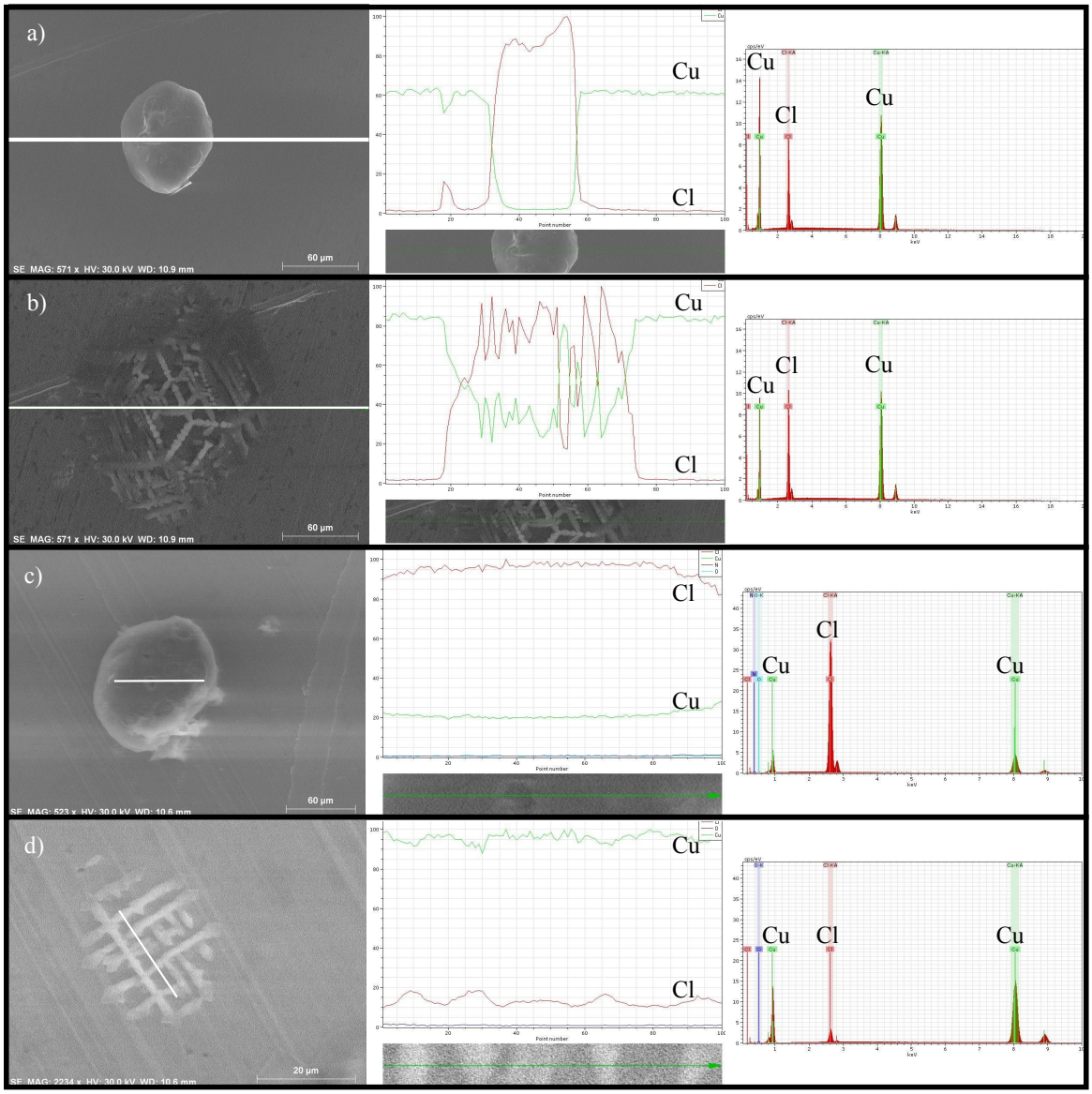

Figure 3.13: EDX line scans of NH_4Cl particles on copper before deliquescence and after efflorescence.

Large NH_4Cl particles were also studied on silicon wafer surface. Figure 3.14 shows dry NH_4Cl particles, their deliquesced state, and final effloresced images on SiO_2. Frame d) is a higher magnification image of the lower particle in frame a). Therefore frames c) and f) show the same effloresced image as the two particles in

frame a) after they coalesce. Meanwhile, Figure 3.15 shows dry NH_4Cl particles along with deliquesced and effloresced states on cobalt with TiN layer in frames a) through f). Frames g) and h) show regions close to effloresced NH_4Cl particles on SiO_2 and frame i) shows a typical effloresced state on cobalt coated with TiN. As in Figures 3.11 and 3.12, all the effloresced states have a larger surface coverage than the dry states. Also, upon efflorescing on SiO_2 the NH_4Cl solution formed a crust-like coverage even in regions far away from the original particle location as shown in frames g) and h) in Figure 3.15. This phenomenon was not observed on the cobalt coated side of the wafer. No size change calculations were made since the effloresced images were too large to be shown in one image.

Once again, EDX line scans were completed of the NH_4Cl crystals before deliquescence and after efflorescence. The EDX results for silicon wafer deposited NH_4Cl crystals are shown in Figure 3.16. In the figure, frames a) and b) correspond to pre-deliquescence and post-efflorescence on SiO_2 while c) and d) show the same states on cobalt with TiN coating. From the data it is clear that the beam energy was too high as in Figure 3.13 since no cobalt is detected in frames c) and d). Therefore the beam penetrated too deep into the sample and in future studies a lower beam energy should be used. However, once again chlorine is found in the artifact along with an increase in the footprint after efflorescence.

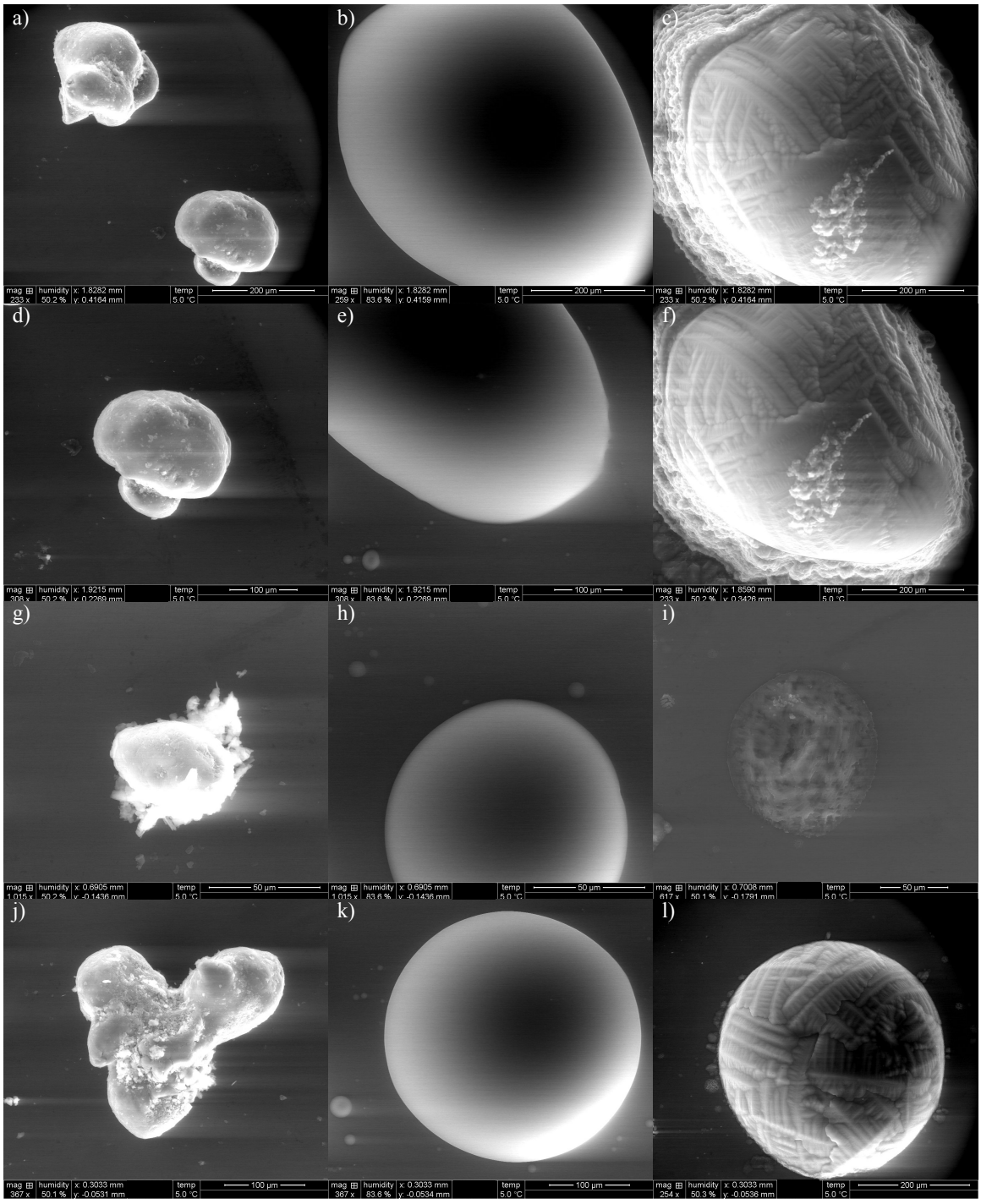

Figure 3.14: ESEM images of NH_4Cl particles and their corresponding effloresced images on silicon wafer.

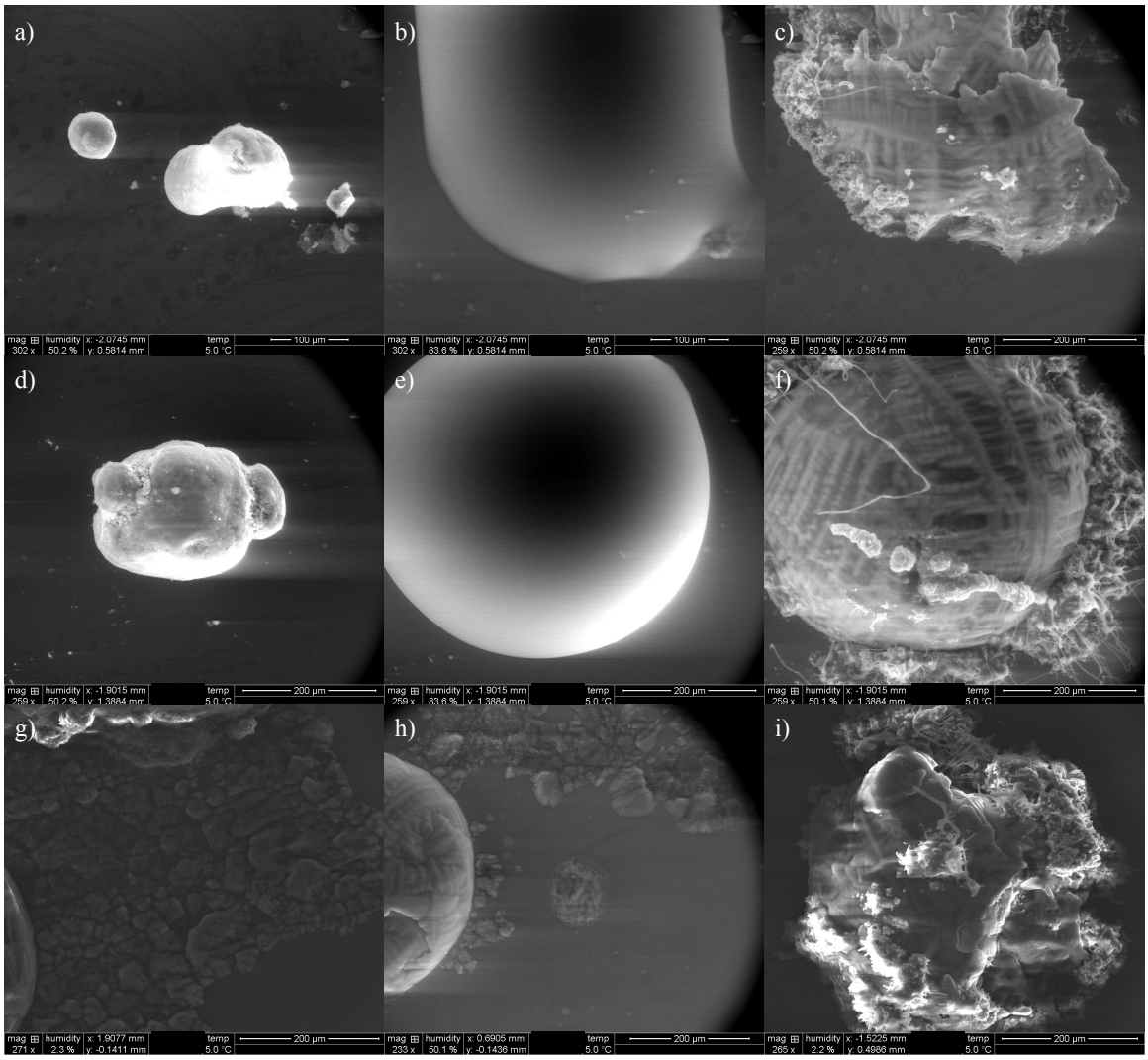

Figure 3.15: ESEM images of NH_4Cl particles and their corresponding effloresced images on cobalt witness wafer with TiN coating in frames a) through f) and i). Frames g) and h) are on silicon wafer.

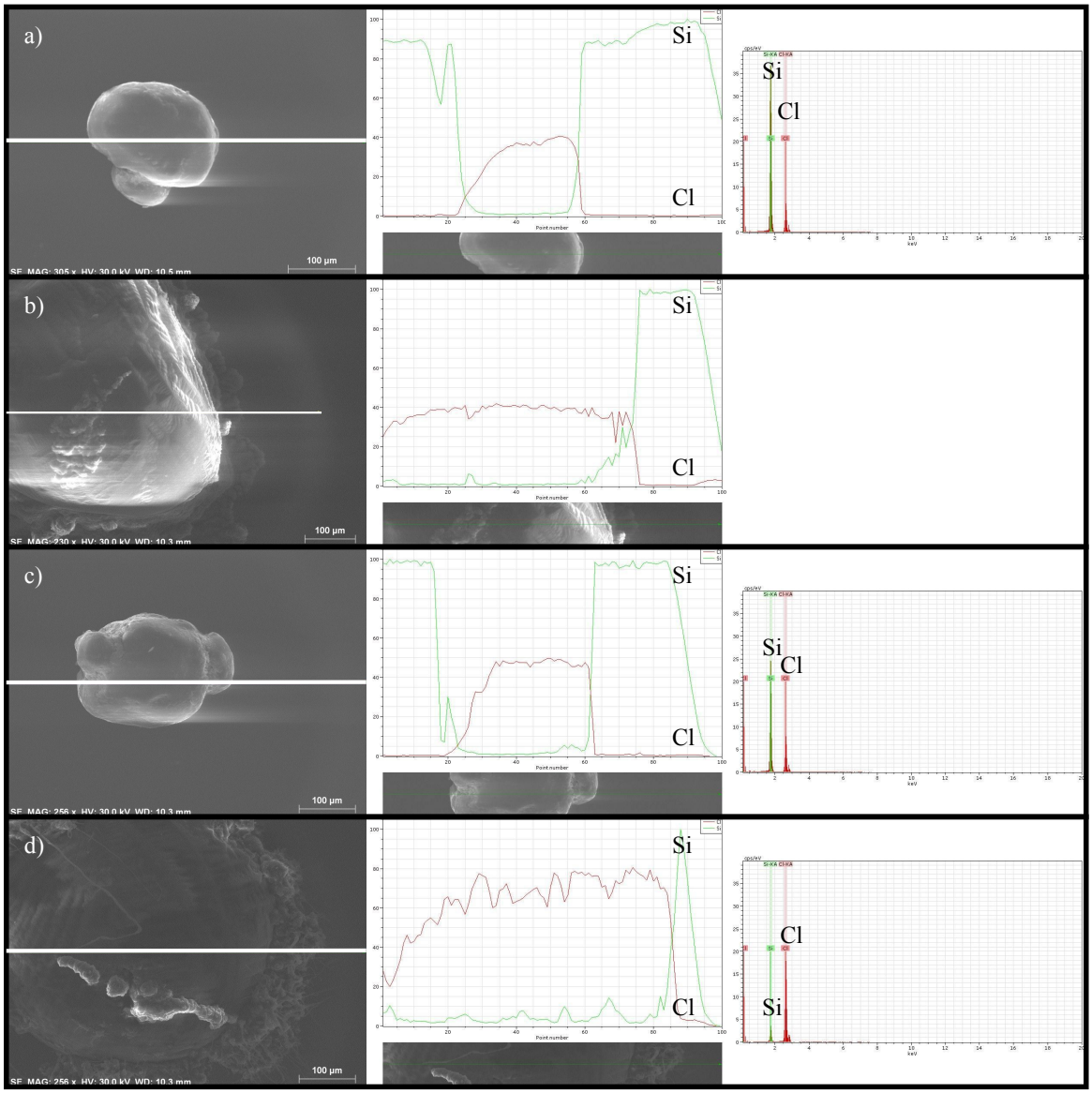

Figure 3.16: EDX line scans of NH_4Cl particles on silicon wafer with a)SiO_2, and b)Co with TiN coatings, before deliquescence and after efflorescence.

Since the NH_4Cl artifacts seemed to exhibit differing behavior on SiO_2 and Co with TiN surfaces, optical images were also used to get a different perspective. Similar to the ESEM samples, large NH_4Cl crystals were placed onto wafer surfaces. With the crystals on the wafer, the samples were placed into a chamber into which water

vapor was introduced until the relative humidity reached 90%. After exposing the samples to the environment for 10 minutes, they were effloresced with 15% relative humidity compressed air. Following efflorescence, the samples were imaged. Figure 3.17 shows the effloresced particles on SiO_2 in frames a) and b) while frames c) and d) show the effloresced state on Co with TiN. The optical images confirm the ESEM observations that on SiO_2 the crystals leave a crust like coverage that can span large areas surrounding the original deposit. Additionally, the round spots indicate the original particle location has a topography similar to the crust surrounding them. The round spots were observed to be thicker than the crust since at high magnifications both the deposit location and crust could not be brought to focus at the same time with the deposit location coming to focus before the crust when lowering the sample stage. The artifacts on the Co with TiN are drastically different from the SiO_2 ones. In frames c) and d) no crust like artifact is found and the spots of the original deposit have a fractal like effloresced deposit. Additionally, the Co surrounding appears corroded as indicated by the discoloration. The discoloration could indicate the extent the particles covered the surface once they were deliquesced.

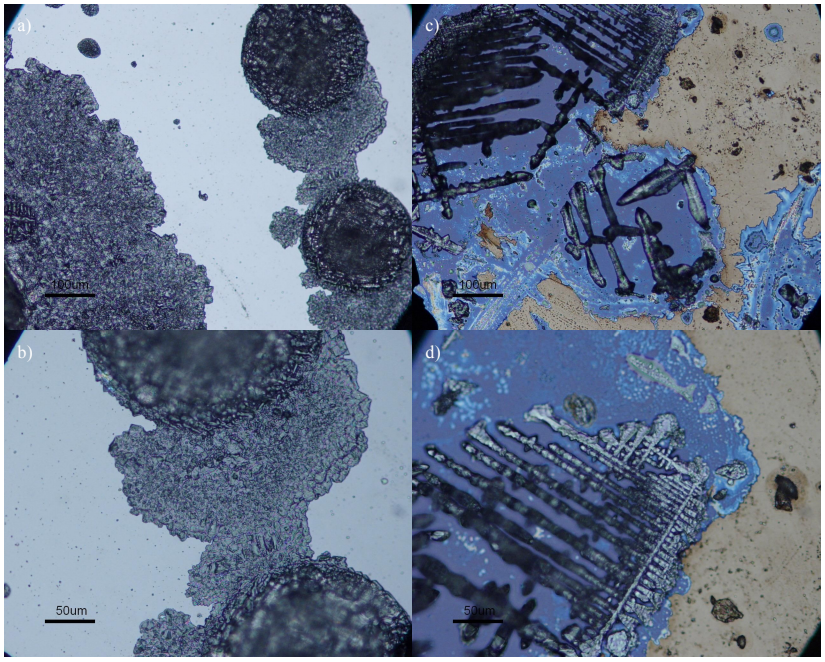

Figure 3.17: Optical images of large NH_4Cl crystals after efflorescence. Frames a) and b) show SiO_2 coating while c) and d) show Co with TiN.

To generate particle sizes closer to those of contaminants in a cleanroom environment, 50% solubility by mass NH_4Cl solution was atomized and deposited on wafer pieces. Figure 3.18 shows dry, deliquesced, and effloresced states of atomized NH_4Cl particles on cobalt coated silicon wafer with TiN coating. Additionally, Figure 3.19 shows atomized NH_4Cl particles on topography with SiO_2 coating. Also, Figure 3.20 shows a higher magnification image of atomized particle through the deliquescence and efflorescence cycle on cobalt in frames a) through c), and on topography in frames d) through f). Finally, Figure 3.21 shows a high magnification image of a final effloresced state on cobalt. Once again, the sample temperature was limited to 5°C. Figure 3.18 shows that in addition to a large deliquesced droplet, a multitude of smaller droplets are formed around the perimeter increasing the total area affected by the solution.

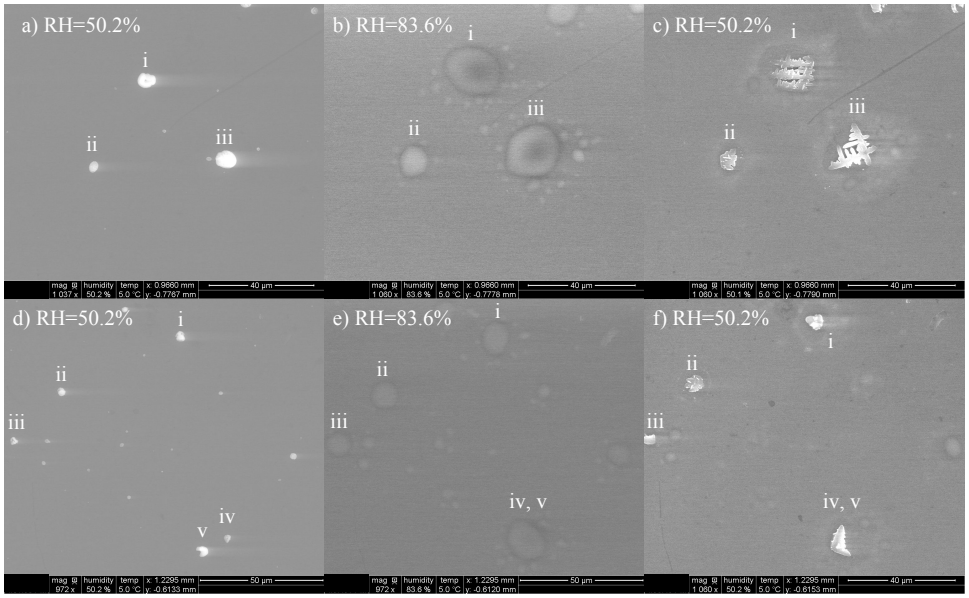

Figure 3.18: ESEM images of NH_4Cl particles on witness wafer through deliquescence and efflorescence cycle.

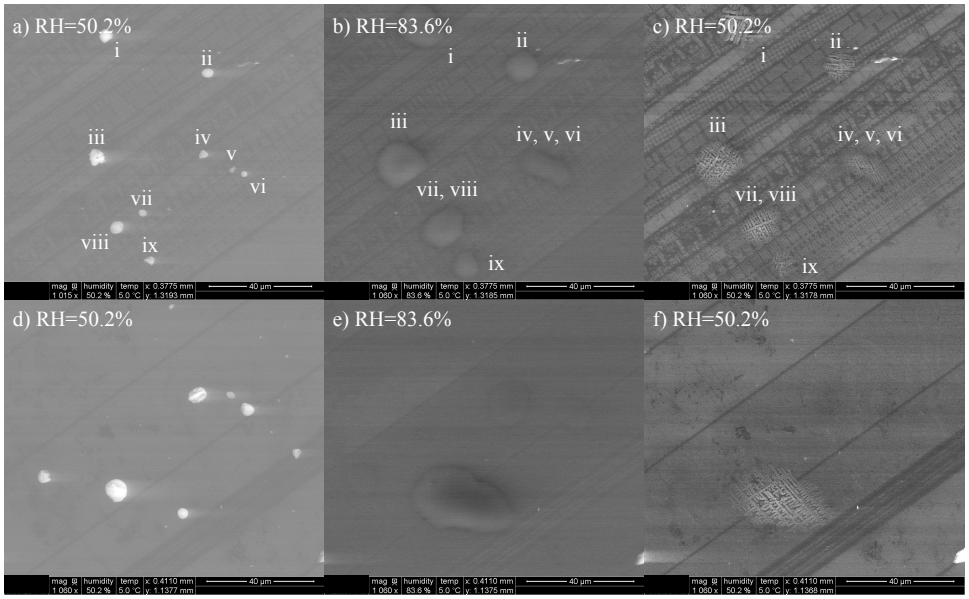

Figure 3.19: ESEM images of NH_4Cl on topography with 50Å SiO_2 coating through deliquescence and efflorescence cycle

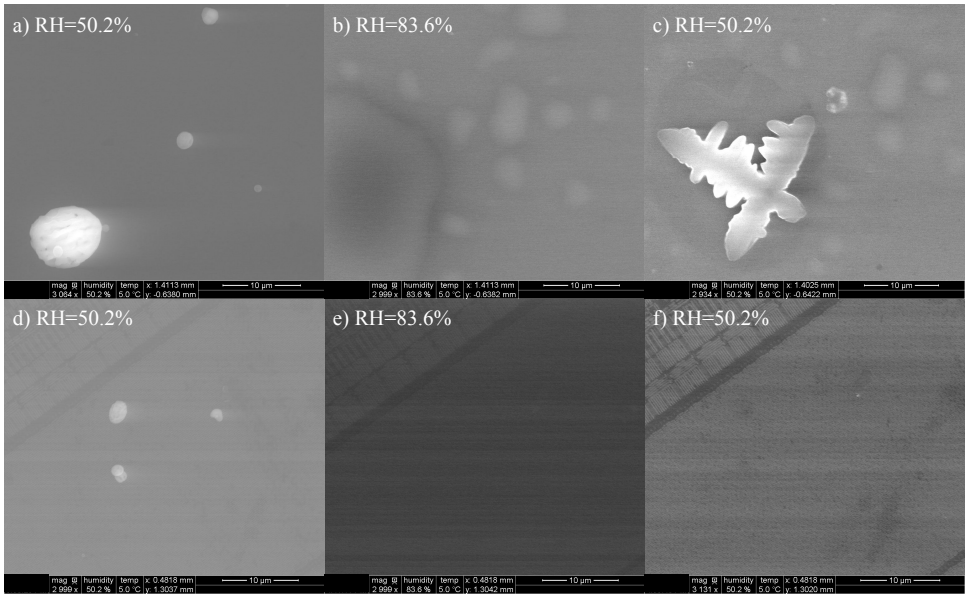

Figure 3.20: High magnification ESEM images of NH_4Cl on cobalt coated witness wafer and topography with 50Å SiO_2 coating through deliquescence and efflorescence cycle

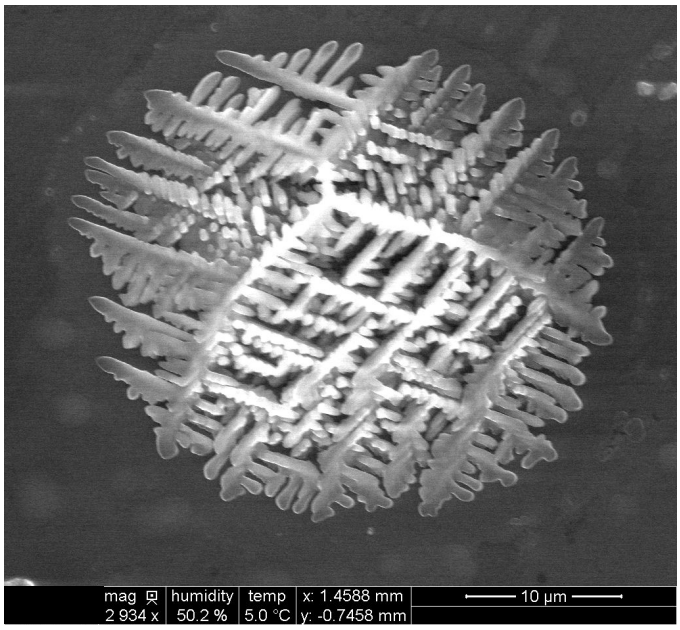

Figure 3.21: High magnification ESEM images of an effloresced NH_4Cl particle on cobalt coated witness wafer.

Similar to Figures 3.11 and 3.12, diameter and area change calculations were made for the increase from the dry particle foot print to that of the deliquesced and effloresced states. The results are shown in Tables 3.3 and 3.3. Predictions were also included based on Köhler theory with the growth factor calculated using the Extended AIM Aerosol Thermodynamics Model [22]. In the Table 3.3, $d_{T,s}$ corresponds to the theoretical diameter if the original particle were to deliquesce when aerosolized. As another approximation, $d_{T,h}$ corresponds to the diameter of a hemisphere that has an equal volume to $d_{T,s}$. The hemispherical prediction aims to forecast the growth of a deposited particle since the fluid would not exist as a perfect sphere on a surface.

Table 3.3: Growth of NH_4Cl diameter on wafer.

Figure	$\mathbf{d}_P$ [μ**m**]	$\mathbf{d}_D$ [μ**m**]	$\mathbf{d}_E$ [μ**m**]	$\mathbf{d}_{T,s}$ [μ**m**]	$\mathbf{d}_{T,h}$ [μ**m**]
3.18a,b,c	7.5	22.9	16.8	13.9	17.5
	5.4	13.2	8.9	10.1	12.7
	9.3	22.9	20.6	17.4	21.9
3.18d,e,f	5.3	13.9	8.0	9.8	12.4
	4.4	11.7	8.4	8.1	10.3
	4.0	9.6	6.0	7.5	9.4
	4.0, 5.8	17.2	13.1	7.5, 10.8	9.4, 13.6
3.19d,e,f	6.4	17.9	17.9	11.9	15.1
	5.5	13.9	12.0	10.3	13.0
	7.8	18.7	18.8	14.5	18.2
	4.6, 3.7, 3.4	19.7	15.3	8.6, 6.8, 6.3	10.8, 8.6, 7.9
	4.0, 6.4	17.0	17.1	7.5, 11.9	9.4, 15.1
	4.6	11.4	11.2	8.6	10.8

Table 3.4: Growth of NH_4Cl area on wafer.

Figure	$\mathbf{A}_P$ [$\mu\mathbf{m}^2$]	$\mathbf{A}_D$ [$\mu\mathbf{m}^2$]	$\mathbf{A}_E$ [$\mu\mathbf{m}^2$]	$\mathbf{A}_{T,s}$ [$\mu\mathbf{m}^2$]	$\mathbf{A}_{T,h}$ [$\mu\mathbf{m}^2$]
3.18a,b,c	43.7	410.5	222.7	152.3	241.7
	23.0	136.7	61.6	80.4	127.6
	68.1	410.5	332.5	237.5	377
3.18d,e,f	21.8	152.6	50.5	75.9	120.5
	14.9	107.2	55.9	52.1	82.8
	12.6	72.2	28.5	44.0	69.9
	12.5, 26.4	233.9	135.4	43.7, 92.0	69.4, 146.1
3.19d,e,f	32.1	250.0	250.0	112.1	178.0
	24.1	152.4	112.6	84.0	133.3
	47.2	276.1	277.0	164.6	261.2
	16.7, 10.6, 8.8	303.7	184.0	58.1, 36.8, 30.8	92.2, 58.5, 48.9
	12.7, 32.1	226.5	230.4	44.1, 112.1	70.1, 178.0
	16.7	102.5	98.4	58.1	92.3

The change in area from dry particle to deliquesced or effloresced state was calculated using equations 3.1 and 3.2. The area changes are shown in columns 2 and 3 of Table 3.3. Columns 4-7 show the error based on the predicted areas versus the actual areas. For a single particle, the error is defined as

$$E = 100\frac{A_T - A_f}{A_f} \tag{3.3}$$

For situtions where multiple particles coalesced upon deliquescing, the error is defined as

$$E = 100\frac{\sum A_{T,i} - A_f}{A_f} \tag{3.4}$$

In Table 3.3 the subscript D indicates the deliquesced state, E the effloresced state, s the predicted area with a spherical assumption, and h the predicted area

with a hemispherical assumption. For the deliquesced state, the hemispherical prediction more closely approximates the area than the spherical one. For the effloresced state, the hemispherical model generally overpredicts the area while the spherical approximation underestimates the final foot print.

Table 3.5: Growth of NH_4Cl foot print on wafer.

Figure	$\Delta\mathbf{A}_D$ [%]	$\Delta\mathbf{A}_E$ [%]	$\mathbf{E}_{D,s}$ [%]	$\mathbf{E}_{E,s}$ [%]	$\mathbf{E}_{D,h}$ [%]	$\mathbf{E}_{E,h}$ [%]
3.18a,b,c	840.0	410.0	-62.9	-31.2	-41.1	8.5
	493.2	167.4	-41.2	30.4	-6.7	107.1
	502.8	388.2	-42.1	-28.2	-8.2	13.4
3.18d,e,f	600.9	131.2	-50.2	50.4	-21.0	138.8
	616.8	273.9	-51.3	-6.7	-22.8	48.1
	472.0	125.8	-39.0	54.4	-3.2	145.1
	500.8	247.7	-42.0	0.28	-7.9	59.2
3.19d,e,f	680.7	680.7	-55.3	-55.3	-29.1	-29.1
	532.6	367.6	-44.9	-25.4	-12.5	18.4
	485.0	486.9	-40.4	-40.6	-5.5	-5.7
	405.5	414.2	-58.6	-31.7	-34.3	8.5
	405.5	414.2	-31.0	-32.2	9.5	7.7
	515.2	490.7	-43.3	-41.0	-10.0	-6.3

For the cases where the particles did not coalesce, additional analysis was completed to determine the height of each deliquesced state. The height of the deliquesced droplets was calculated by assuming a spherical cap with a radius, a, as the measured deliquesced diameter. The spherical cap is illustrated in Figure 3.22. The volume of a spherical cap can be calculated by

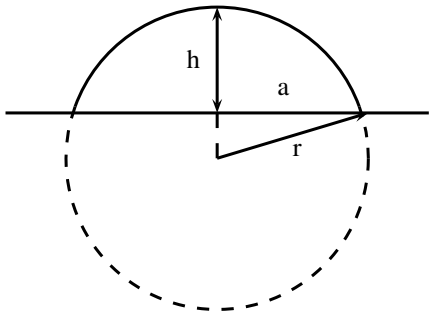

Figure 3.22: Spherical cap showing the parameters necessary for calculations of its properties.

$$V = \frac{\pi h}{6}\left(3a^2 + h^2\right) \tag{3.5}$$

The volume was set equal to that if the dry particle were to completely deliquesce and reach an equilibrium size. Therefore with both the diameter and volume known, the height of the spherical cap could be calculated. The results are illustrated in Figures 3.23 through 3.25 where Figure 3.23 corresponds to deliquesced particles on SiO_2 and Figures 3.24 and 3.25 correspond to cobalt with TiN coating.

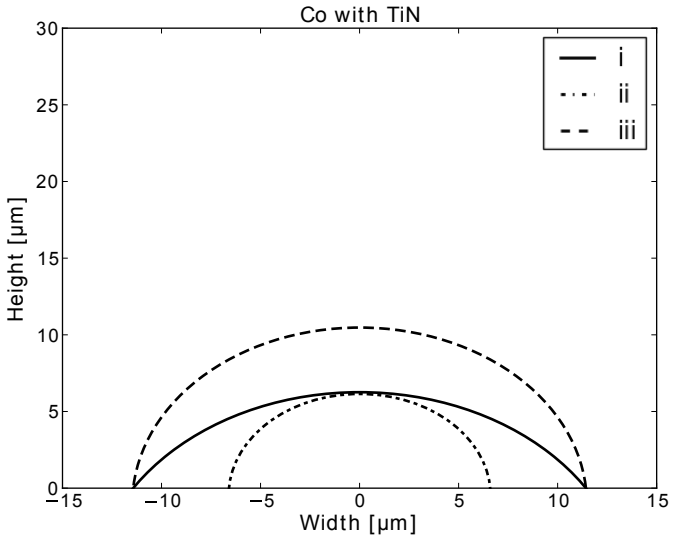

Figure 3.23: Deliquesced NH_4Cl particles on cobalt with TiN layer approximated as spherical caps from Figure 3.18.

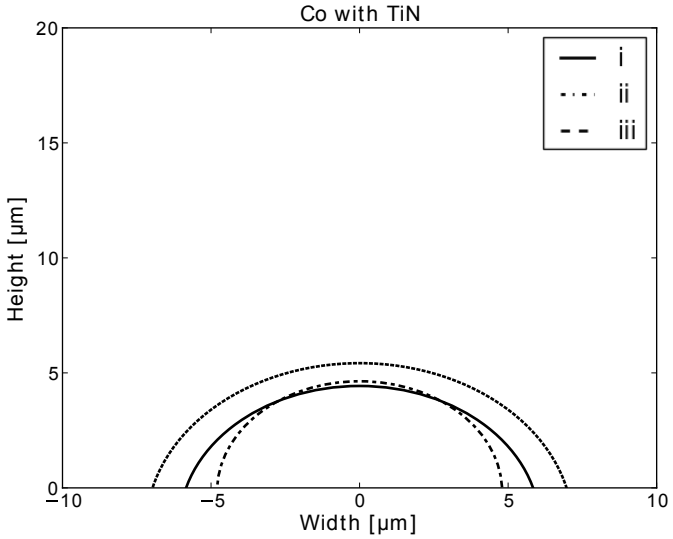

Figure 3.24: Deliquesced NH_4Cl particles on cobalt with TiN layer approximated as spherical caps from Figure 3.18.

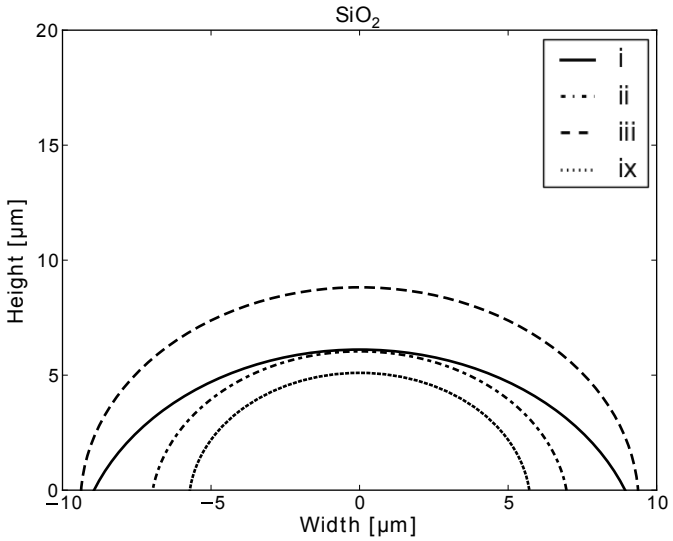

Figure 3.25: Deliquesced NH_4Cl particles on SiO_2 approximated as spherical caps from Figure 3.19.

The wetting by the particles can be characterized by the ratio of the height to the radius, h/a. The ratios are summarized in Table 3.3. There appears to be no significant difference when comparing the ratios on SiO_2 to those on Co with TiN. Therefore based on the analysis here, an NH_4Cl particles will wet both surfaces to the same extent. In future studies, an inclined SEM sample holder should be used to measure the true angle between the wafer and droplet. Additionally, the spherical cap approximation has significant uncertainty since after deliquescing, the NH_4Cl particles appeared to form smaller droplets surrounding the large droplet at the original dry location. Therefore the equivalent volume approximation may not be a valid constraining the approximation. Also, the SiO_2 coating was on top of topography and not a flat surface possibly altering the wetting characteristics. On the other hand, the wetting on the cobalt can be affected the chemical reaction occurrig between the salt and substrate observed in the beginning of the chapter.

Table 3.6: Deliquesced NH_4Cl particle aspect ratios approximated as spherical caps.

Figure	Particle	h/a
3.23	i	0.27
	ii	0.47
	iii	0.46
3.24	i	0.39
	ii	0.38
	iii	0.48
3.25	i	0.34
	ii	0.43
	iii	0.47
	ix	0.45

3.4 Wafer Microscopy Conclusion

A methodology was established for observing the effect of humidity on corrosiveness of NH_4Cl deposited on cobalt coated wafers. For particles in the micron size range, optical microscopy techniques can be utilized for general observation of defects. For detailed growth under deliquescence and subsequent efflorescence, an ESEM is appopriate if the beam is blanked during the processes to eliminate energy input into the particle surface system. In all occasions, the effloresced particle diameter did not reduce down to the size of the original dry particle, but left an artifact greater in size with fractal like growth pattern. If a particle were to deliquesce while aerosolized, its deposited diameter would be greater than the airborne diameter. The increase could be roughly be estimated using a hemispherical approximation coupled with Köhler theory. However, the results may vary greatly for different solutions or surface properties. Additionally, the final effloresced diameter cannot be predicted by a simple hemispherical or spherical approximation.

Chapter 4

Conclusion

The work presented here aims to expand upon the literature on hygroscopic particles from the perspective of how environmental changes in a semiconductor wafer processing facilities affect particle changes in filters and on wafer surfaces. In a fab, the study of hygroscopic particles is important to understand contamination pathways as such particles may be found captured in a filter or deposited on a wafer. Based on the filtration background included in Chapter 1, no known studies have been published on deliquescence and efflorescence of filter captured hygroscopic particles due to dynamic fluctuations in the gas relative humidity. Therefore as detailed in Chapter 2, the phase change of particles in a HEPA filter was experimentally studied when the filter was subjected to successive humidity fluctuations above deliquescence and below efflorescence. The salt crystals were found to redistribute themselves into the top layer of the filter upon collapse of the filter cake due to deliquescence. At the high mass loadings, the SEM images show the collected salt to form islands on top of the filter through which air cannot pass. At very high mass loadings, the salt may cover the entire surface of the filter upon efflorescence after the first deliquescence dramatically increasing the pressure drop across the filter. It is of interest to identify if these particles or if the solution can ever escape through the filter. If mass loss were to occur from the filter, it would take place at higher face velocities. Additionally, the deliquesced salt could make its way through the filter if the air humidity would be maintained above the deliquescence point for a longer period of

time. At high deliquesced loadings, the filtration problem becomes similar to the wet filtration studies discussed in Chapter 1 in which re-entrainment was encountered upon reaching the pressure plateau after exponential increase in pressure drop with respect to mass accumulation. However, such high loadings or face velocities are not typically encountered in a fab but could be an issue in other filtration applications

Even though no mass loss was detected following the humidity exposures, important future work should still be conducted to fully assess the risks of hygroscopic contaminants captured in the fab filters. As indicated by both SEM and ESEM images, even at the lower mass loadings the salt particles drastically redistribute on the filter media upon deliquescing. Such transport could bring the hygroscopic contaminants in contact with other artifacts opening a pathway to chemical reactions that would not be otherwise encountered. Also, upon deliquescing the contaminants have a gas liquid interface instead of a solid gas interface with the environment, which could also lead to chemical reactions especially if a volatile chemical leak occurs in the fab. From a general filtration perspective, the filter media studied should be expanded to other materials. The velocity at which shedding of deliquesced droplets could be lower for a more hydrophobic filter material.

Although no re-entrainment was recorded from the HEPA filters, hygroscopic contaminants could still be present in the fab ballroom, for example due to gas to particle reactions. Based on experiments discussed in Chapter 3, the long time humidity exposures of cobalt wafers coated with TiN to varying levels of relative humidity showed significant water vapor interaction for NH_4Cl particles below their deliquescence point. The first exposure test showed that if an NH_4Cl particle were to deposit while still carrying water on its surface onto a wafer, the water would not be expelled at 61% relative humidity but instead the contamination area became infinite as the

particles continued to deliquesce. For completely effloresced NH_4Cl particles, very little, if any, interaction between the wafer and the salt crystals was noted at a relative humidity of 20%. However, in the range of 50-60% the NH_4Cl particles corroded areas surrounding the locations of the original deposits. At relative humidities of 75% and 78% the NH_4Cl particles deliquesced leaving behind no solid artifacts and the corrosion was the most extensive of all the cases. The study of wafer contamination by NH_4Cl particles was also extended with in situ observations with an ESEM. The ESEM results show a different interaction between the cobalt and SiO_2 sides of the wafer. On the cobalt side, particles corrode the areas surrounding the locations of the original deposits leaving a fractal like artifact upon efflorescing. Meanwhile, the deliquesced particles form a crust-like layer around the locations of the original deposits indicating more extensive wetting of the substrate than on the cobalt side. In addition to corrosion observations, the foot print of the final effloresced state could be predicted with roughly 10% accuracy using simple volume conservations and equilibrium growth of an intially dry particle. Such calculations could be useful in determining the source of contaminants if the size of the original dry state could be back-calculated from the artifacts.

The experimental results of Chapter 3 show significant effects of relative humidity on the particle-wafer interaction for NH_4Cl even below the deliquescence point warranting further study. The exact deliquescence point with respect to particle size for NH_4Cl should be determined since micrometer size range particles had deliquesced after 72 hours at a relative humidity approximately 2% below the expected value. The effect of the substrate on the deliquescence point should also be explored. As indicated by the literature review in Chapter 4, some substrates used in silicon manufacturing processes themselves are hygroscopic indicating that the moisture required to deliquesce a small particle could be provided by the substrate itself. Additionally, if a

hygroscopic particle were to exothermically react with the deposition substrate, it could provide a localized relative humidity required for deliquescence at the environments water vapor partial pressure. Also, since the deliquescence relative humidity decreases with an increase in temperature, processes that heat the substrate could lead to a pathway to deliquescence if they are allowed to cool in a space with significant water vapor partial pressure. Perhaps most importantly, typical inorganic hygroscopic salt contaminants in a fab should be characterized to determine their composition. From the composition, the deliquescence point of each contaminant could be determined. Particles containing more than one solute would possibly be most ciritcal since the deliquescence point of a multicomponent inorganic salt system is lower than the deliquescence point of either individual constituents.

Appendix A

Transient Data For The Filtration Experiments

Figures A.1 through A.5 shows the pressure difference as well as the relative humidities as a function of time for the filtration experiments. In each figure, the flat region around 0 following atomization is the time taken to measure the accumulated filter cake mass. Additionally, Figures A.6 through A.10 illustrate the relative humidities and temperatures for each filter mass loading in Chapter 2. In all the figures included in this appendix, the dash-dot horizontal line represents the deliquescence humidity for NaCl.

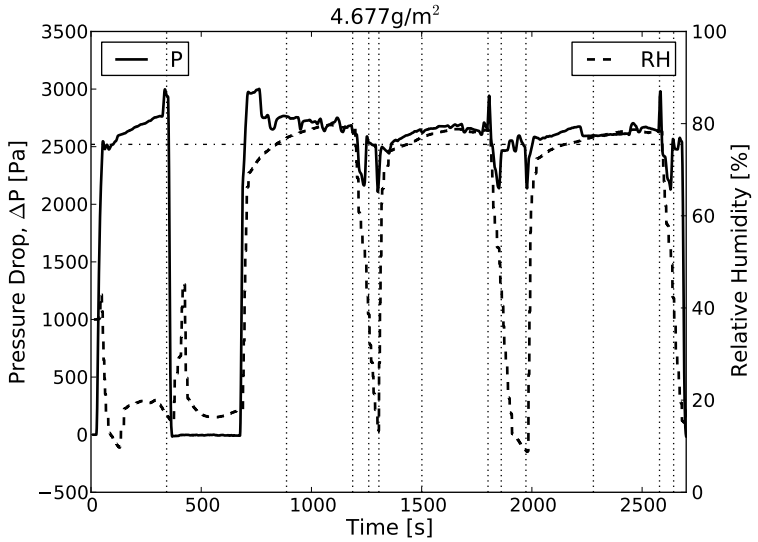

Figure A.1: Relative humidity and pressure difference as a function of time for 4.677g/m^2 mass loading

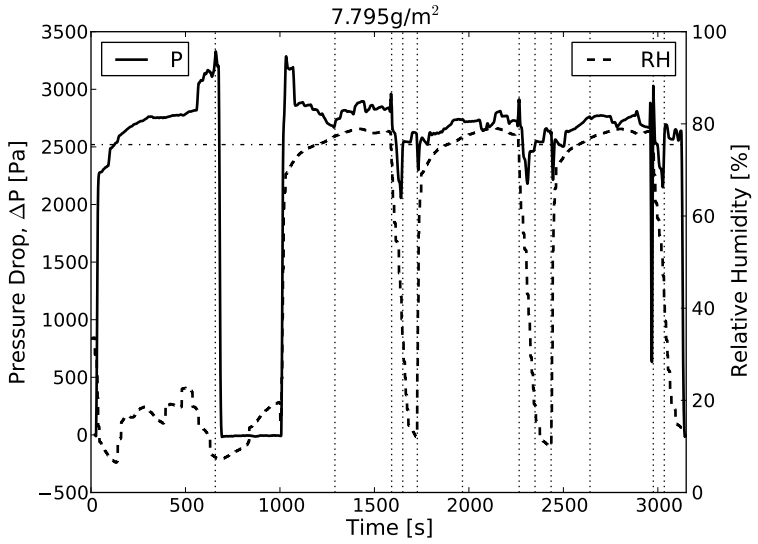

Figure A.2: Relative humidity and pressure difference as a function of time for 7.795g/m^2 mass loading

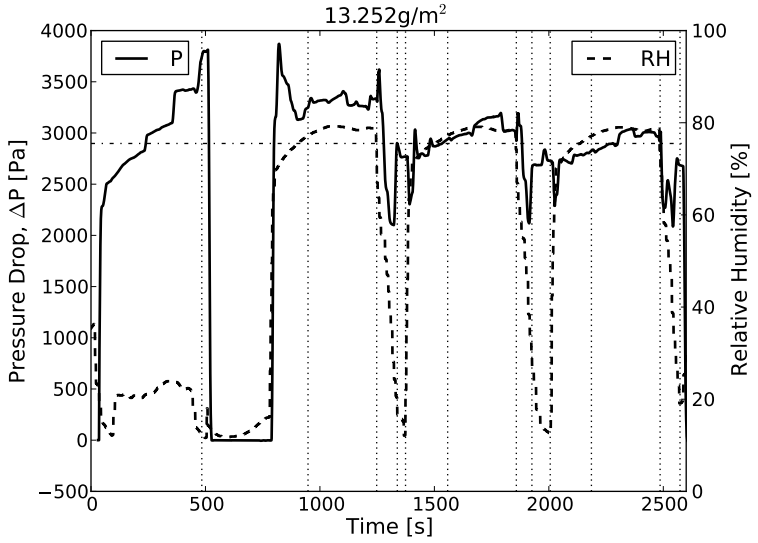

Figure A.3: Relative humidity and pressure difference as a function of time for 13.252g/m^2 mass loading

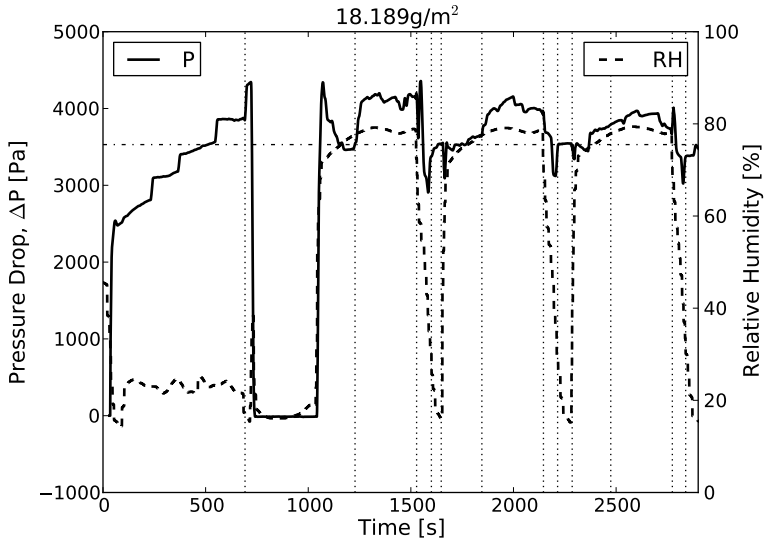

Figure A.4: Relative humidity and pressure difference as a function of time for 18.189g/m^2 mass loading

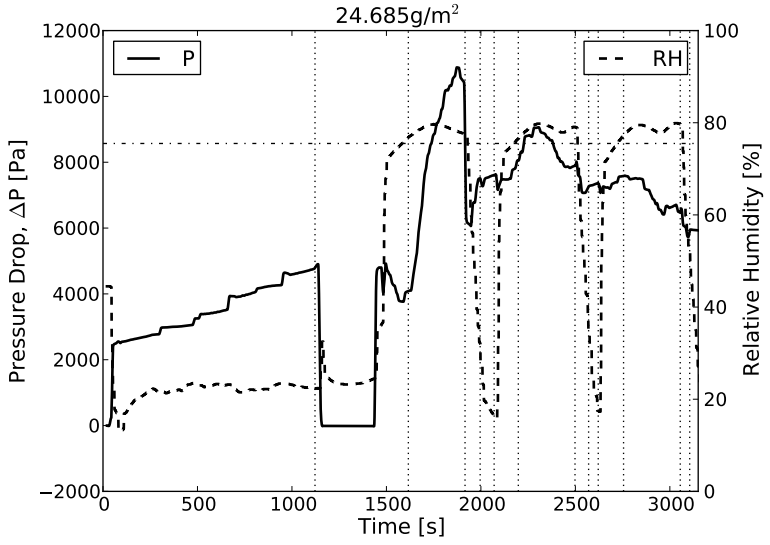

Figure A.5: Relative humidity and pressure difference as a function of time for 24.685g/m^2 mass loading

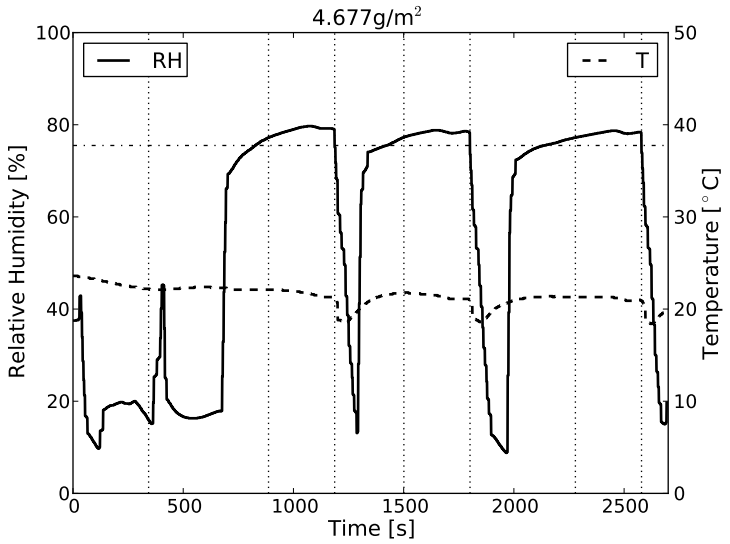

Figure A.6: Relative humidity and temperature as a function of time for 4.677g/m^2 mass loading

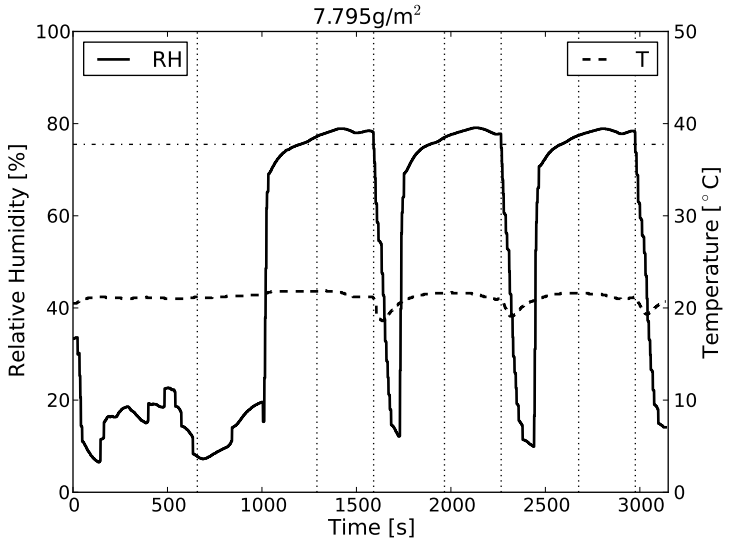

Figure A.7: Relative humidity and temperature as a function of time for 7.795g/m^2 mass loading

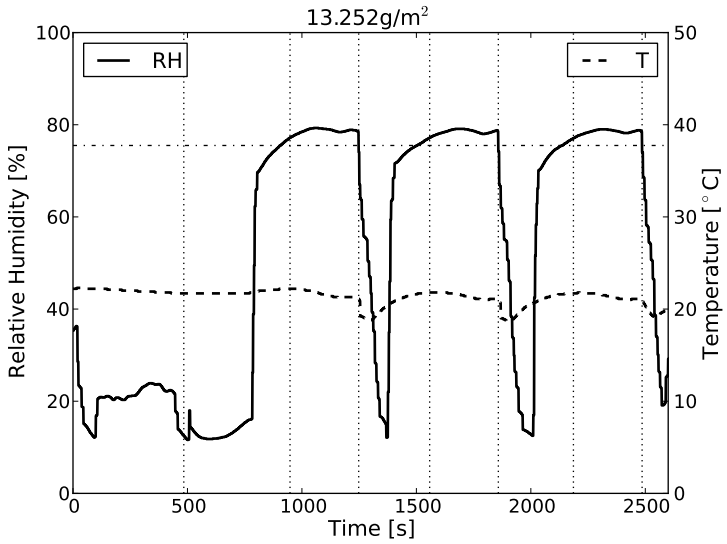

Figure A.8: Relative humidity and temperature as a function of time for 13.252g/m^2 mass loading

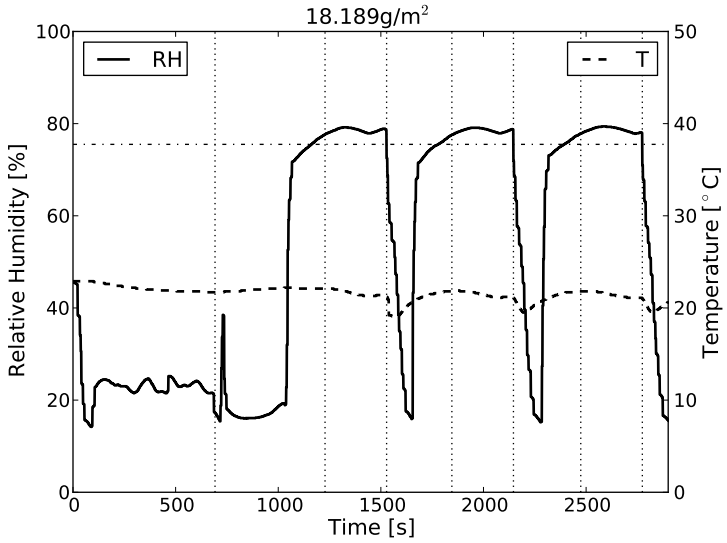

Figure A.9: Relative humidity and temperature as a function of time for 18.189g/m^2 mass loading

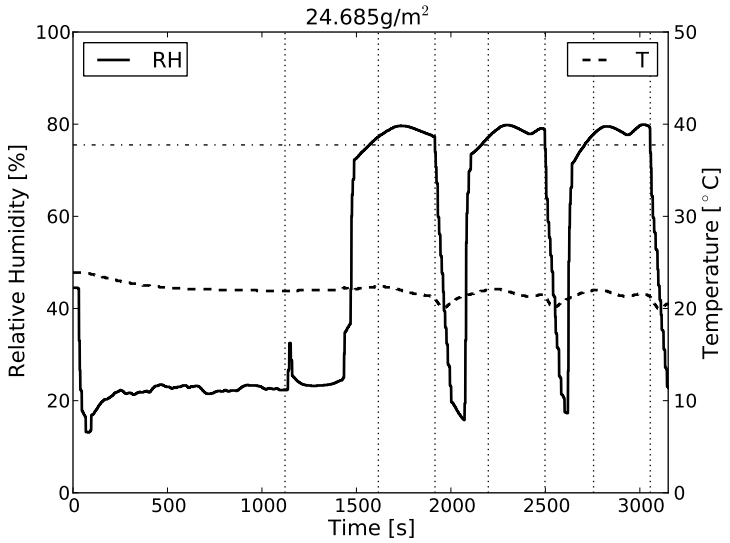

Figure A.10: Relative humidity and temperature as a function of time for 24.685g/m^2 mass loading

Appendix B

Circles Used For Wafer Particle and Artifact Calculations

The figures in this appendix illustrates the circles used for diameter and area increase in Chapter 3.

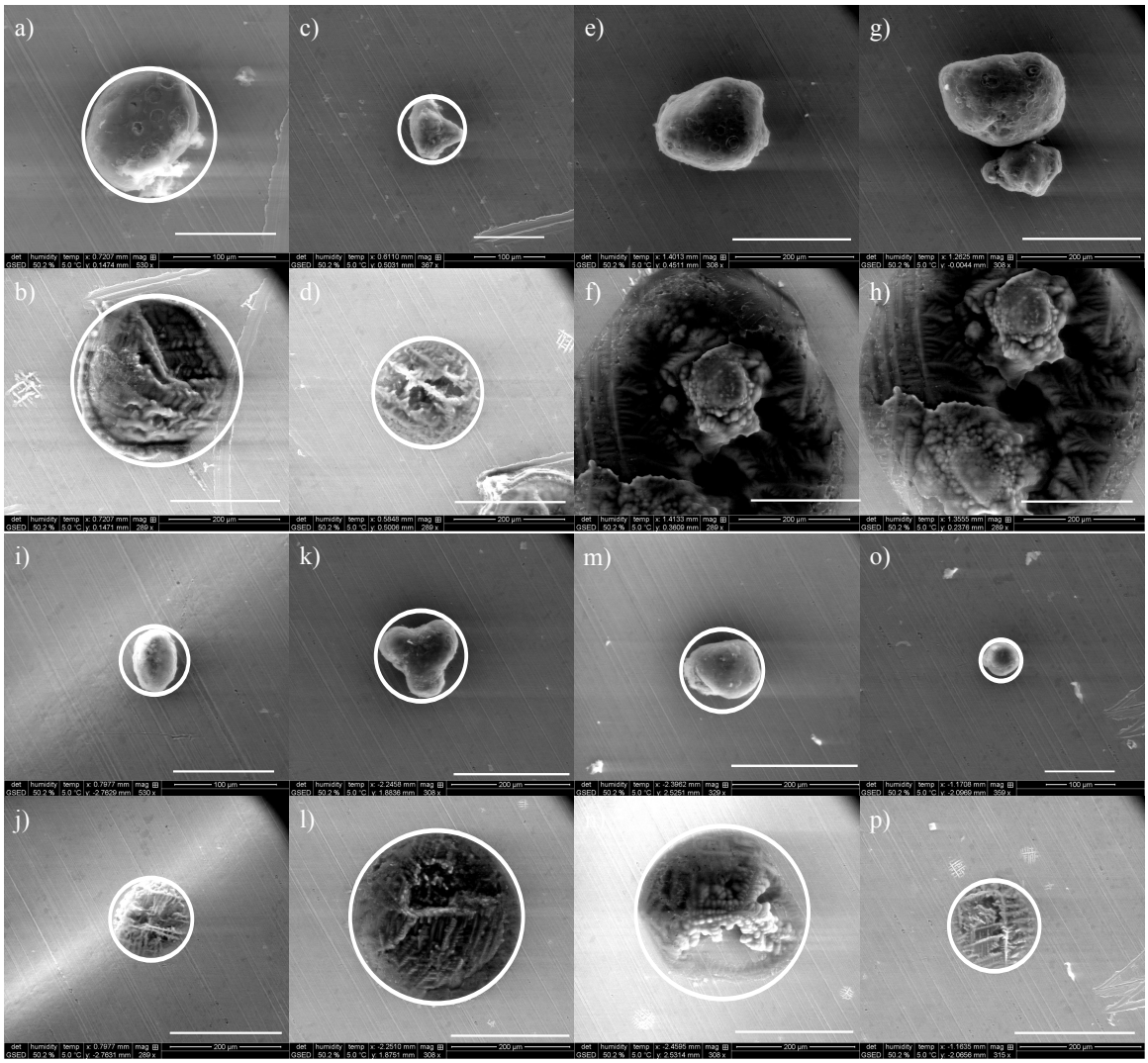

Figure B.1: Circles used for area and diameter calculations in Figure 3.11

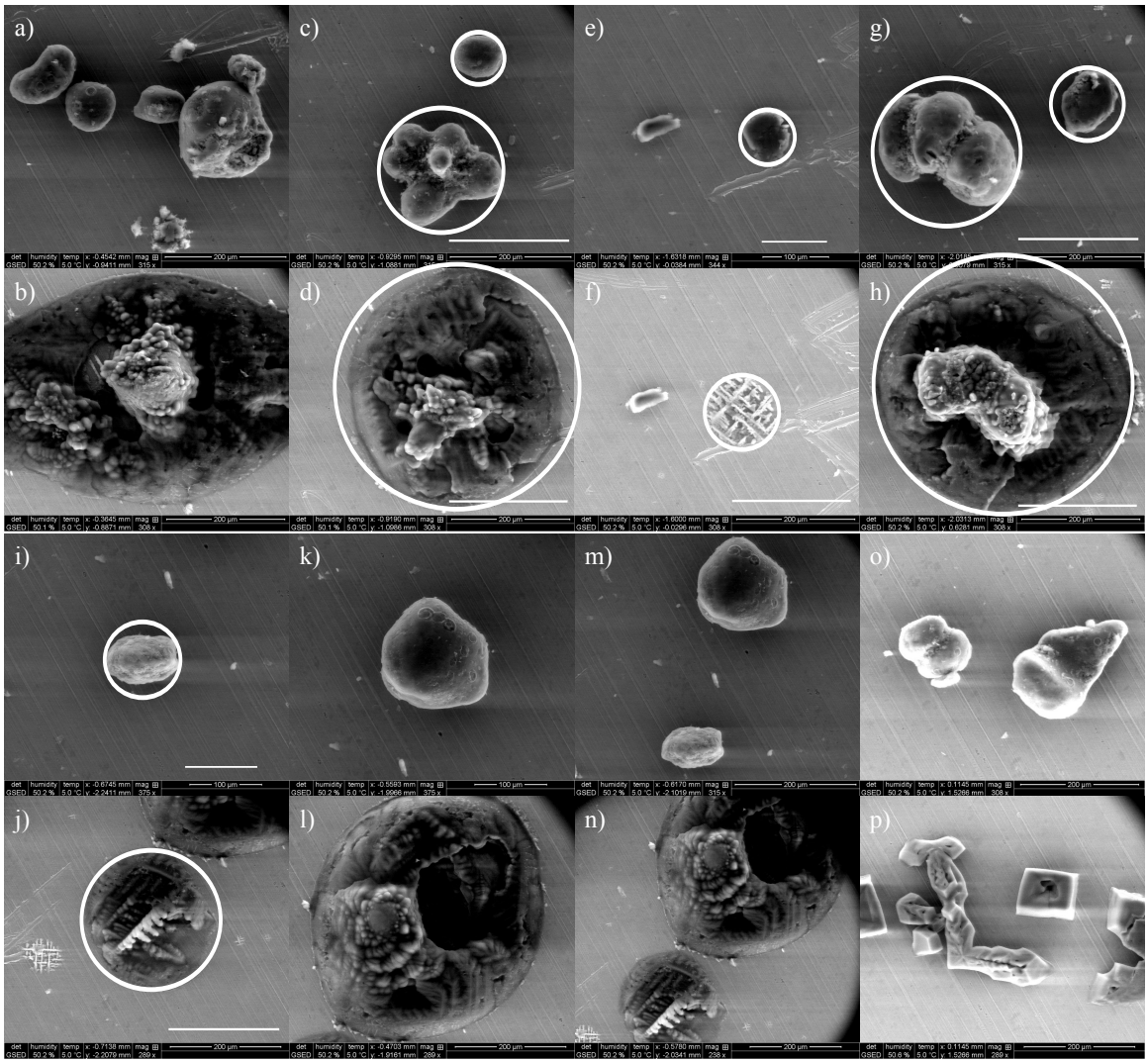

Figure B.2: Circles used for area and diameter calculations in Figure 3.12

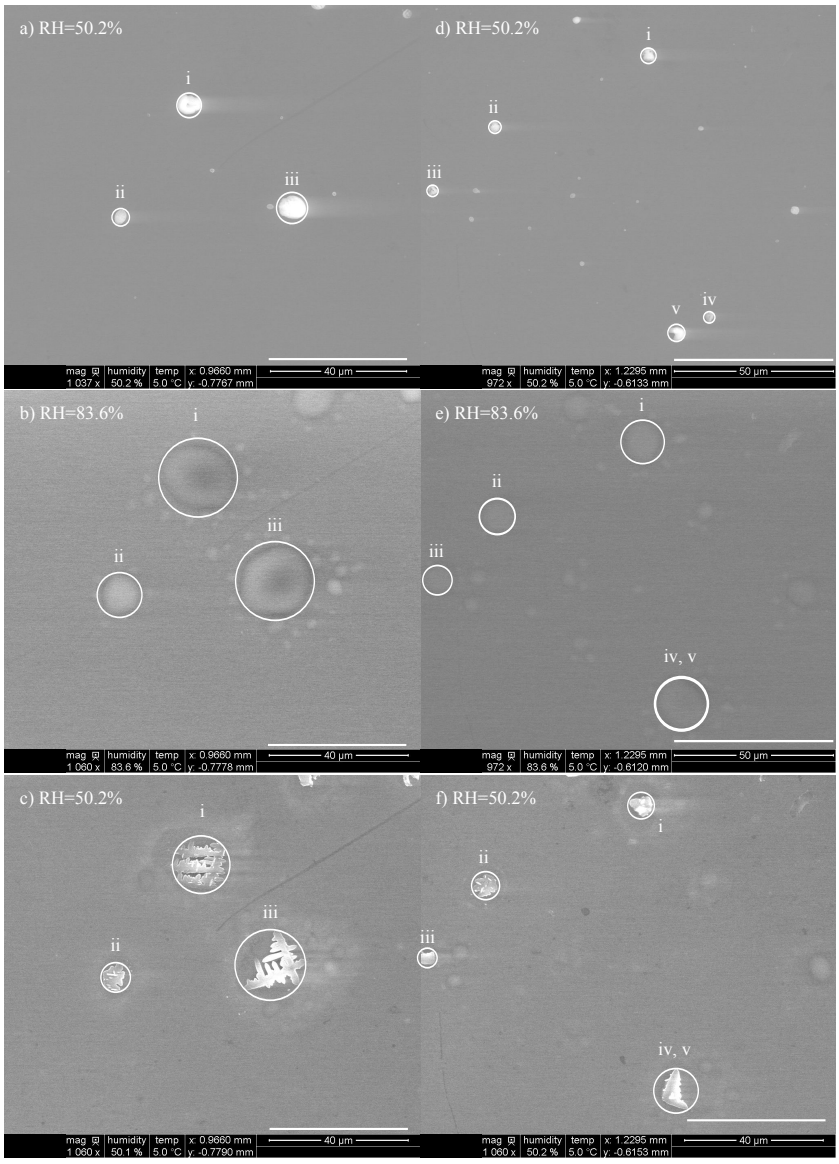

Figure B.3: Circles used for area and diameter calculations in Figure 3.18

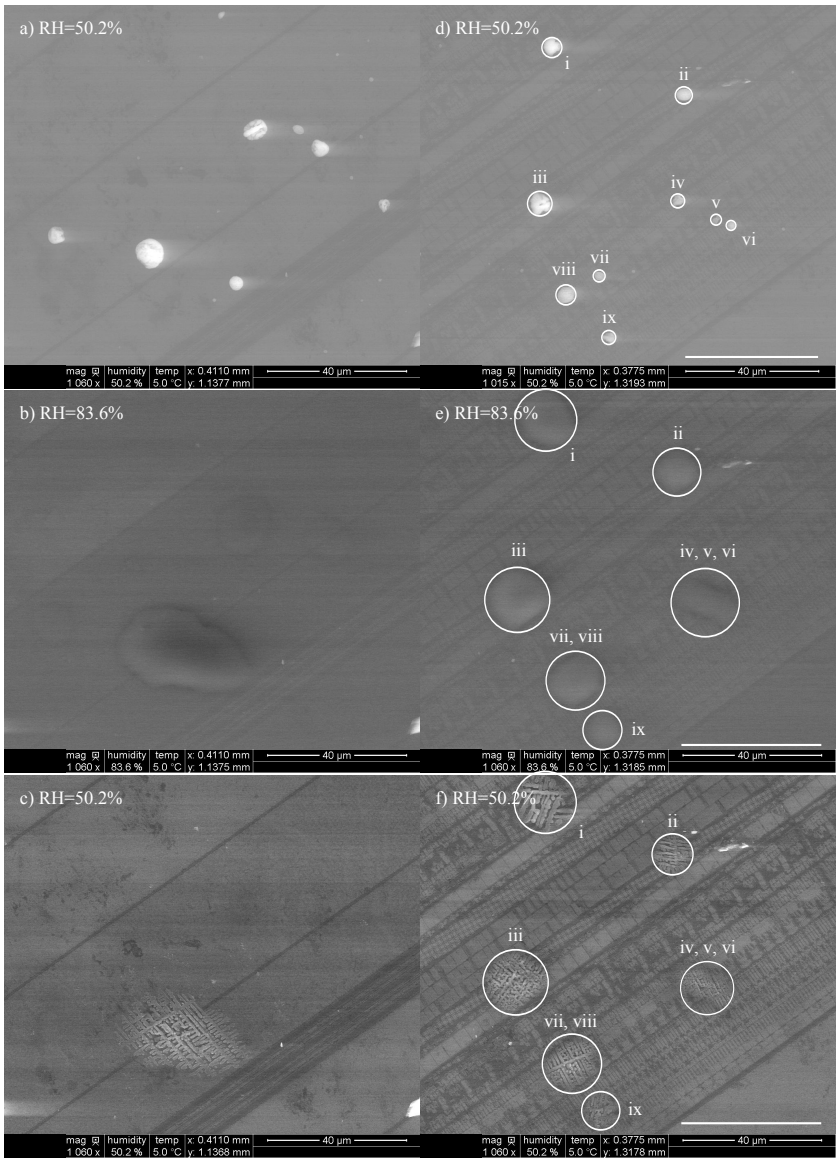

Figure B.4: Circles used for area and diameter calculations in Figure 3.19

Bibliography

[1] W. Hinds, *Aerosol Technology: Properties, Behavior, and Measurement of Airborne Particles.* 2nd ed., 1999.

[2] D. A. Japuntich, J. I. T. Stenhouse, and B. Y. H. Liu, "Experimental results of solid monodisperse particle clogging of fibrous filters," *Journal of Aerosol Science*, vol. 25, no. 2, pp. 385–393, 1994.

[3] D. Thomas, P. Penicot, P. Contal, D. Leclerc, and J. Vendel, "Clogging of fibrous fiters by solid aerosol particles: Experimental and modelling study," *Chemical Engineering Science*, vol. 56, pp. 3549–3561, 2001.

[4] V. J. Novick, P. R. Monson, and P. E. Ellison, "The effect of solid particle mass loading on the pressure drop of HEPA filters," *Journal of Aerosol Science*, vol. 23, no. 6, pp. 657–665, 1992.

[5] P. Contal, J. Simao, D. Thomas, T. Frising, S. Callé, J. C. Appert-Collin, and D. Bémer, "Clogging of fibre filters by submicron droplets. Phenomena and influence of operating conditions," *Journal of Aerosol Science*, vol. 35, pp. 263–278, Mar. 2004.

[6] I. N. Tang, H. R. Munkelwitz, and J. G. Davis, "Aerosol growth studies II. Preparation and growth measurements of monodisperse salt aerosols," *Journal of Aerosol Science*, vol. 8, no. 3, pp. 149–159, 1977.

[7] K. Linnow and M. Steiger, "Determination of equilibrium humidities using temperature and humidity controlled X-ray diffraction (RH-XRD).," *Analytica chim-*

ica acta, vol. 583, pp. 197–201, Jan. 2007.

[8] S. El Golli, J. Bricard, P.-Y. Turpin, and C. Treiner, "The evaporation of saline droplets," *Journal of Aerosol Science*, vol. 5, no. 3, pp. 273–292, 1974.

[9] A. Joubert, J. C. Laborde, L. Bouilloux, S. Callé-Chazelet, and D. Thomas, "Influence of Humidity on Clogging of Flat and Pleated HEPA Filters," *Aerosol Science and Technology*, vol. 44, pp. 1065–1076, Nov. 2010.

[10] C. P. Lyons, "Design Principles for the Entries and Transmission Lines of Aerosol Analysers," in *Aerosol Sampling Guidelines* (A. L. Nichols, ed.), ch. 2, pp. 32–60, 1st ed., 1998.

[11] "Model 3320 Aerodynamic Particle Sizer Instruction Manual," 2000.

[12] H. Bai, Y. Kang, and C. Liu, "Dimensional and Elemental Analysis of Particulate Contaminations on Silicon Wafers," *Aerosol Air Qual. Res*, vol. 2, no. 1, pp. 53–60, 2002.

[13] T. Liew and J. Conder, "Fine mist filtration by wet filters-I. Liquid saturation and flow resistance of fibrous filters," *Journal of Aerosol Science*, vol. 16, pp. 497–509, Jan. 1985.

[14] S. Tekasakul, P. Suwanwong, Y. Otani, and P. Tekasakul, "Pressure Drop Evolution of a Medium-Performance Fibrous Filter During Loading of Mist Aerosol Particles," *Aerosol and Air Quality Resarch*, vol. 8, no. 3, pp. 348–365, 2008.

[15] P. Penicot, D. Thomas, F. Contal, D. Leclerc, and J. Vendel, "Clogging of HEPA Fibrous Filters by Solid and Liquid Aerosol Particles: An Experimental Study," *Filtration and Separation*, no. March, pp. 59–64, 1999.

[16] S. Payet, D. Bouland, G. Madeleine, and A. Renoux, "Penetration and Pressure Drop of a HEPA Filter During Loading with Submicron Liquid Particles," *Journal of Aerosol Science*, vol. 23, no. 7, pp. 723–735, 1992.

[17] T. Frising, D. Thomas, D. Bémer, and P. Contal, "Clogging of fibrous filters by liquid aerosol particles: Experimental and phenomenological modelling study," *Chemical Engineering Science*, vol. 60, pp. 2751–2762, May 2005.

[18] R. McGraw and E. R. Lewis, "Deliquescence and efflorescence of small particles.," *The Journal of chemical physics*, vol. 131, pp. 194705–1–194705–14, Nov. 2009.

[19] H. Köhler, "The nucleus in and the growth of hygroscopic droplets," *Transactions of the Faraday Society*, vol. 32, pp. 1152–1161, 1936.

[20] I. Tang, "Phase transformation and growth of aerosol particles composed of mixed salts," *Journal of Aerosol Science*, vol. 7, no. 5, pp. 361 – 371, 1976.

[21] I. N. Tang and H. R. Munkelwitz, "Composition and temperature dependence of the deliquescence properties of hygroscopic aerosols," *Atmospheric Environment. Part A. General Topics*, vol. 27, no. 4, pp. 467–473, 1993.

[22] S. L. Clegg, P. Brimblecombe, and A. S. Wexler, "Extended AIM Aerosol Thermodynamics Model."

[23] K. Linnow, H. Juling, and M. Steiger, "Investigation of NaCl deliquescence in porous substrates using RH-XRD," *Environmental Geology*, vol. 52, pp. 317–327, Jan. 2007.

[24] A. Gupta, V. Novick, P. Biswas, and P. Monson, "Effect of Humidity and Particle Hygroscopicity on the Mass Loading Capacity of High Efficiency Particulate Air

(HEPA) Filters," *Aerosol Science and Technology*, vol. 19, no. 1, pp. 94–107, 1993.

[25] A. Craig and R. McIntosh, "The preparation of sodium chloride of large specific surface," *Canadian Journal of Chemistry*, vol. 30, no. 5, pp. 448–453, 1952.

[26] L. Krämer, U. Pöschl, and R. Niessner, "Microstructural rearrangement of sodium chloride condensation aerosol particles on interaction with water vapor," *Journal of Aerosol Science*, no. 6, pp. 673–685.

[27] O. Brekke and L. E. Bakken, "Performance deterioration of intake air filters for gas turbines in offshore installations," in *Proceedings of the ASME Turbo EXPO 2010, Vol 5*, pp. 685–694, Int Gas Turbine Inst, 2010. ASME Turbo Expo 2010, Glasgow, Scotland, Jun. 14-18, 2010.

[28] C. N. Davies, "The entry of aerosols into sampling tubes and heads," *Journal of Physics D: Applied Physics*, vol. 1, pp. 921–932, 1968.

[29] F. Durst, S. Noppenberger, M. Still, and H. Venzke, "Influence of humidity on hot-wire measurements," *Measurement Science and Technology*, vol. 7, pp. 1517–1528, Oct. 1996.

[30] L. Greenspan, "Humidity fixed points of binary saturated aqueous solutions," *Journal of Research of the National Bureau of Standards*, vol. 81, no. 1, pp. 89–96, 1977.

[31] A. Joubert, J. C. Laborde, L. Bouilloux, S. Chazelet, and D. Thomas, "Modelling the pressure drop across HEPA filters during cake filtration in the presence of humidity," *Chemical Engineering Journal*, vol. 166, no. 2, pp. 616–623, 2011.

[32] S. Li, H. Shih, S. Yen, and J. Yang, "Case study of micro-contamination control," *Aerosol and Air Quality Resarch*, vol. 7, no. 3, pp. 432–442, 2007.

[33] I. K. Lin, H. Bai, and B. J. Wu, "Analysis of Relationship between Inorganic Gases and Fine Particles in Cleanroom Environment," *Aerosol and Air Quality Research*, vol. 10, pp. 245–254, 2010.

[34] S. J. Lue, T. Wu, H. Hsu, and C. Huang, "Application of ion chromatography to the semiconductor industry. I. Measurement of acidic airborne contaminants in cleanrooms.," *Journal of chromatography. A*, vol. 804, pp. 273–8, Apr. 1998.

[35] S. J. Lue and C. Huang, "Applications of ion chromatography in the semiconductor industry. II. Determination of basic airborne contaminants in a cleanroom.," *Journal of chromatography. A*, vol. 850, pp. 283–287, July 1999.

[36] B. J. Wu, H. Bai, I. K. Lin, and S. S. Liu, "AlCu Pattern Wafer Study on Metal Corrosion Due to Chloride Ion Contaminants," *Semiconductor Manufacturing, IEEE Transactions on*, vol. 23, no. 4, pp. 553–558, 2010.

[37] B. J. Wu, H. Bai, I. Lin, and H. H. Liu, "Metal Corrosion of Al-Si-Cu Pattern Wafer Due to Chloride Ion Contaminants," *Aerosol and Air Quality Resarch*, vol. 12, pp. 104–112, 2012.

[38] S. K. Fan and J. W. McPherson, "A wafer-level corrosion susceptibility test for multilayered metallization," in *Reliability Physics Symposium 1988. 26th Annual Proceedings., International*, no. c, pp. 50–57, 1988.

[39] Z. Y. Chen, S. Zakipour, D. Persson, and C. Leygraf, "Effect of Sodium Chloride Particles on the Atmospheric Corrosion of Pure Copper," *Corrosion*, vol. 60, no. 5, pp. 479–491, 2004.

[40] T. Dyer, "Moisture instability of borophosphosilicate glass and the effects of thermal treatment," *Journal of The Electrochemical Society*, no. May 2012, pp. 3950–3956, 1998.

[41] A. G. Thorsness and A. J. Muscat, "Moisture Absorption and Reaction in BPSG Thin Films," *Journal of The Electrochemical Society*, vol. 150, no. 12, pp. F219–F228, 2003.

[42] M. Ebert, M. Inerle-hof, and S. Weinbruch, "Environmental scanning electron microscopy as a new technique to determine the hygroscopic behaviour of individual aerosol particles," *Atmospheric Environment*, vol. 36, pp. 5909–5916, 2002.

[43] T. Matsumura and M. Hayashi, "Hygroscopic Growth of an (NH4)2SO4 Aqueous Solution Droplet Measured Using an Environmental Scanning Electron Microscope (ESEM)," *Aerosol Science and Technology*, vol. 41, pp. 770–774, Aug. 2007.

[44] M. Wise, G. Biskos, S. Martin, L. Russell, and P. Buseck, "Phase Transitions of Single Salt Particles Studied Using a Transmission Electron Microscope with an Environmental Cell," *Aerosol Science and Technology*, vol. 39, pp. 849–856, Sept. 2005.

[45] K.-H. Ahn, S.-M. Kim, H.-J. Jung, M.-J. Lee, H.-J. Eom, S. Maskey, and C.-U. Ro, "Combined use of optical and electron microscopic techniques for the measurement of hygroscopic property, chemical composition, and morphology of individual aerosol particles.," *Analytical chemistry*, vol. 82, pp. 7999–8009, Oct. 2010.

[46] M. Wise, S. Martin, L. Russell, and P. Buseck, "Water Uptake by NaCl Particles Prior to Deliquescence and the Phase Rule," *Aerosol Science and Technology*, vol. 42, pp. 281–294, Apr. 2008.

[47] D. A. Bruzewicz, A. Checco, B. M. Ocko, E. R. Lewis, R. L. McGraw, and S. E. Schwartz, "Reversible uptake of water on NaCl nanoparticles at relative humidity below deliquescence point observed by noncontact environmental atomic force microscopy.," *The Journal of Chemical Physics*, vol. 134, p. 044702, Jan. 2011.

[48] D. Hu, J. Chen, X. Ye, L. Li, and X. Yang, "Hygroscopicity and evaporation of ammonium chloride and ammonium nitrate: Relative humidity and size effects on the growth factor," *Atmospheric Environment*, vol. 45, no. 14, pp. 2349–2355, 2011.

Vita

Mikko Ponkala was born in Turku, Finland. As a teenager, he moved to the United States of America where he eventually completed a B.S.M.E and a M.S.M.E at The University of Texas at Austin in 2010 and 2012 respectively. Mikko's hobbies inlcude playing guitar as well as constructing guitar amplifiers. He also enjoys building model railroads.

Permanent contact information: mikko@utexas.edu

This thesis was typed by Mikko Juha Viljami Ponkala.